# ANALYSIS OF HYDRAULIC FRACTURE PROPAGATION AND WELL PERFORMANCE USING GEOMECHANICAL MODELS AND FAST MARCHING METHOD

A Dissertation

by

JIXIANG HUANG

Submitted to the Office of Graduate and Professional Studies of
Texas A&M University
in partial fulfillment of the requirements for the degree of

DOCTOR OF PHILOSOPHY

| | |
|---|---|
| Chair of Committee, | Akhil Datta-Gupta |
| Co-Chair of Committee, | Michael J. King |
| Committee Members, | Eduardo Gildin |
| | Yalchin Efendiev |
| Head of Department, | A. Daniel Hill |

May 2017

Major Subject: Petroleum Engineering

# ABSTRACT

Successful exploitation of unconventional resource plays relies on the massive hydraulic fractures which provide high conductive paths and large contact area between formation and wellbore. The pursuit of efficiency and cost savings drives the industry to implement the strategies that utilize more closely spaced hydraulic fractures, as well as multiple horizontal wells with reduced spacing, to maximize the production from unconventional reservoirs with ultra-low permeability. One rising challenge from this trend is to find the optimized spacing between fracture clusters, fracture stages, and fractured horizontal wells so that the potential fracture interference could be minimized. This interference could occur at different scales within lifecycle of exploration, from stress interference in completion stage to pressure interference in production stage. Thus, to systematically study these issues, both geomechanical model and reservoir model are required. In this dissertation, a finite element based geomechanical model and a fast marching based reservoir model are customized to address these emerging problems in unconventional reservoir development.

First, we present a comprehensive study of various factors that affect the performance of refracturing operation, such as fracturing spacing, permeability, proppants and refracturing time, by using a cohesive zone finite element based model that can capture the effect of depletion on fracture propagation. The well performance are evaluated under two different refracturing designs: refracturing new or existing perforations. Based on the simulation results, their respective suitability have been concluded.

Second, we integrate fracture propagation, reservoir flow and wellbore hydraulics to evaluate the stress shadow effect and efficiency of limited entry perforations during multiple simultaneous fracture propagation within a single fracture stage. Simulation results provide insights to the selection of operational parameters such as cluster spacing, number of clusters and perforations, which can be modified accordingly to deal with the fracture interference and thus promote the uniform stimulation in the formation.

Last, to study the production interference between wells, on top of current fast marching based reservoir simulation workflow, we proposed an approach to extend its applicability from transient to boundary-dominated flow regime, as well as a new partition method to identify the respective drainage volume of individual well. This partition criterion utilizes asymptotic pressure solution and results in a good approximation to the conventional streamline tracing method. The supremacy of numerical efficiency has been further demonstrated with numerical experiments.

# DEDICATION

To my parents and my wife for their love and support

# ACKNOWLEDGEMENTS

First and foremost, I would like to express my deepest gratitude to my advisor, Dr. Akhil Datta-Gupta, for his continuous enlightenment, academic guidance, and financial support. His remarkable knowledge and insightful view helped me tackle obstacles in the completion of this study.

I would like to extend my sincere gratitude to my co-advisor, Dr. Michael J. King, for his inspiring ideas and encouragement through the meetings and discussions. I am also grateful to my committee members, Dr. Eduardo Gildin and Dr. Yalchin Efendiev for their helpful comments and valuable suggestions.

I would like to thank ExxonMobil for providing me internship opportunities, where I gained lots of industry experience and broadened my vision.

Special thanks to all MCERI members and friends in Texas A&M University for making me a wonderful and memorable life in College Station.

Finally, thanks to my beloved parents and wife for their endless encouragement and support.

CONTRIBUTORS AND FUNDING SOURCES

## Contributors

This work was supervised by a dissertation committee consisting of Professors Akhil Datta-Gupta (advisor), Michael J. King (co-advisor), and Eduardo Gildin of the Department of Petroleum Engineering and Professor Yalchin Efendiev of the Department of Mathematics.

All work for the dissertation was completed independently by the student.

## Funding Sources

This work was made possible by the financial support of the JIP members of the Model Calibration and Efficient Reservoir Imaging (MCERI) consortium in Texas A&M University.

TABLE OF CONTENTS

Page

LIST OF FIGURES

Page

LIST OF TABLES

Page

# CHAPTER I

# INTRODUCTION

Unconventional resources are those located outside of conventional oil and gas deposits and generally contained in complex geological systems that prevent them from migrating into wellbore in the way they do in conventional reservoirs. In recent years, unconventional resources such as shale gas have taken a significant share in the energy supply in the US and the world energy market. The advent and growth of the development of these resources have been driven largely by the advances in new technologies such as horizontal well drilling and multistage hydraulic fracturing.

To successful exploitation of unconventional resource plays relies on the massive hydraulic fractures which provide high conductive paths and large contact area between formation and wellbore. The pursuit of efficiency and cost savings drives the industry to implement the strategies that utilize more closely spaced hydraulic fractures, as well as multiple horizontal wells with reduced spacing, to maximize the production from unconventional reservoirs with ultra-low permeability. One rising challenge from this trend is to find the optimized spacing between fracture clusters, fracture stages, and fractured horizontal wells so that the potential fracture interference could be minimized. This interference could occur at different scales within lifecycle of exploration, from stress interference in completion stage to pressure interference in production stage. Meanwhile, fracture conductivity is found to degrade over time with production declining to near-matrix level after 6 to 7 years, thus restimulation of the reservoir becomes another attractive approach to maximize production.

## 1.1 Overview of Refracturing

Unlike the conventional reservoir, one major issue in unconventional reservoirs is the rapid decline of production rate in the early few years. To compensate this production reduction, drilling multiple parallel horizontal wells close to existing wells is a very common practice in the field development. However, in low oil price environment, the urgent goal is to reduce cost and maintain, even increase, production from existing assets. Considering that drilling new wells is usually costly and time-consuming, refracturing existing well, about one-third cost of completing a new well (Dahl et al. 2016), has been recognized as an economically promising option to inhibit the decline of production and improve the well deliverability (Craig et al. 2012; Jayakumar et al. 2013; Vincent 2010).

Based on a compilation of published literature, Vincent (2010) summarized more than 100 field studies in which the restimulation treatments have been performed and concluded a series of critical mechanisms responsible for production improvement achieved by refracturing, such as enlarged fracture geometry, increased pay coverage (with increased fracture height), restored fracture conductivity, reactivated natural fractures and fracture reorientation to touch 'new' rock. The common problems that lead to failed stimulation have also been explored and guidelines for evaluating the refracturing candidates are suggested. Craig et al. (2012) discussed some possible reasons for improved well performance with refracturing based on simulation and history matching on Bakken wells. Jayakumar et al. (2013) performed a series of refracturing modeling under different scenarios in shale reservoir to understand the permeability range and existing fracture

spacing under which refracturing might be beneficial. Malpani et al. (2015) also showed that refracturing can improve the performance of early suboptimal-completed wells with relatively large cluster spacing and small proppant volumes. Overall, the requirement for refracturing can be due to various reasons such as initial inefficient completion, proppant degradation, near wellbore damage and pressure depletion. Therefore, the rationale of refracturing treatment can be categorized into two types: either achieve a larger simulated reservoir volume (SRV) than initial fracturing or restore the existing fracture conductivity. No matter which scenario is being pursued, for a successful refracturing strategy, understanding specifically what are expected to be accomplished before any restimulation practice is the first key step.

Numerical simulations have been proved to be a very effective and efficient tool to facilitate the understanding of important mechanisms involved the refracturing process, such as the stress change due to the pressure depletion, and the impact of original fractures on new fracture propagation during refracturing. Unfortunately, majority of the refracturing simulation work in the literature only focus on the production prediction by assuming the same re-fracture geometry as that in the initial fracturing job when using the same pumping schedule (Haddad et al. 2015; Jayakumar et al. 2013; Tavassoli et al. 2013). These simulation results ignore the stress change around the producing fracture and may give biased prediction. Since the major difference between refracturing and initial fracturing is that the reservoir conditions, such as pressure and stress, have changed due to the depletion, a fully coupled geomechanics and fracture model is required to re-examine these results, especially when depletion-induced stress change is non-trivial.

Another big challenge in refracturing is how to select the best candidates from a large pool of producing wells. To compare the relative potential between wells, a reliable and comprehensive criterion is generally required. Most of available literature on refracturing candidate selection, are limited to conventional reservoirs or tight reservoirs (Roussel and Sharma 2011; Vincent 2011). Since there is no well-established guidance for refracturing, the industry practice on the candidate selection are very empirical and operator-specific (French et al. 2014; Grieser et al. 2016). Sinha and Ramakrishnan (2011) proposed a standardized screening method to study the relationship between the production and completion indicators, but this method fails to account for the production history. Barree et al. (2017) discuss the importance of appropriate well conditioning/unloading prior to decision and state that success of such treatments is not guaranteed without understanding the mechanism. Therefore, a physics-based refracturing tool is also highly demanded to guide the refracturing candidate selection.

### 1.2 Overview of Limited Entry Perforations

Production logs from unconventional wells showed that about one-third of the perforation clusters in unconventional reservoirs are not producing (Lecampion et al. 2015; Miller et al. 2011), which are attributed to reasons such as inefficient completion, proppant degradation, near wellbore damage and pressure depletion. Therefore, improving well completion efficiency becomes another crucial topic for unconventional reservoirs. One major reason for above low efficiency has been tied to the so-called ‘stress shadow effects’ due to fracture interaction (Bunger and Peirce 2014; Wu et al. 2015), where fluid

distribution into clusters within the same stage is non-uniform which eventually results in the non-uniform fracture propagation. Due to the closer fracture spacing, the ‘stress shadow effects’ is more significant between fractures within a single stage, compared with that between stages in refracturing model.

Many completion techniques have been developed to promote an effective multi-fracture stimulation of horizontal wells but some of them are under high cost and risk that often make them unattractive. Limited entry technique is a fracturing practice of promoting the development of perforation friction pressure during a reservoir stimulation treatment by limiting the number or size of perforation holes in a completion interval so that fracturing fluid can be diverted into the formation of interest through the selected perforations. This technique is first introduced as a cost-effective approach for multi-zone stimulation in vertical wells. The key idea is to divert the fluid into the target zone by reducing the perforations and increasing treatment rate to amplify pressure loss through perforations (Lagrone and Rasmussen 1963).

Application of limited entry perforation recently has been extended to massive hydraulic fracturing of unconventional reservoir with ultra-low permeability and proved to be excellent stimulation approach for horizontal wells with an acceptable level of cost and risk recently (Oberhofer 2016; Ugueto C et al. 2016). The perforation holes work as chokes connecting wellbore and formation, where the flow resistance is related to perforation diameter and number (Bunger et al. 2014; Economides and Nolte 2000; Wu et al. 2016). Daneshy (2015) presented the theory of dynamic interaction within multiple fractures in horizontal wells which are in line with actual field trend. Lecampion et al.

(2015) clarified the interplay between the impact of perforation friction and stress shadow on multiple fracture propagation and concluded that a sufficiently large pressure drop through perforation can inhibit the stress interference between different fractures. Wu et al. (2016) demonstrated that designing the limited entry perforations by intentionally tailoring perforation dimension in each cluster could promote uniform fracture propagation using the displacement discontinuity method. Beyond the numerical simulations, Ugueto C et al. (2016) used fiber optics data such as DAS and DTS to evaluate the perforation cluster efficiency of limited entry completions and found that certain amount of fracturing occurs in all perforation clusters, contrary to commonly held opinion that lack of fracture initiation is the cause of inefficiency.

### 1.3 Overview of Drainage Volume Characterization

The concept of drainage volume has been widely used in reservoir engineering to characterize the certain reservoir volume associated with a particular well or completion, as well as provide an intuitive way for the management of reservoirs. It is an engineering term with its definition tied to specific applications accordingly. For example, streamlines and time of flight could be very useful to define the associated drainage volume in a water flooding application in conventional reservoir, while pressure depletion and depth of investigation might be more appropriate for a primary depletion application as happened in unconventional development. Considering the extremely low permeability and transient flow regime during the lifetime, the application of depth of investigation is extended to

unconventional reservoirs by applying an asymptotic expansion to the diffusivity equation, leading to the Eikonal equation that governs the propagation of the pressure front.

To intuitively visualize the drainage volume evolution, numerical method like streamline has been used to help visualize the trajectories or flow paths, which are always tangential to the local velocity field. Streamlines represent the instantaneous velocity field and form as long as the underlying velocity field exists, no matter of the flow conditions such as compressible or incompressible flow, steady or unsteady flow, oil or gas reservoirs (Datta-Gupta and King 2007). The visualization power of streamlines have been proved to be very powerful to examine both swept and drainage volumes in conventional reservoirs, but it requires the information of flux field that is generally calculated by full finite difference/volume simulation and cumbersome in high resolution reservoirs.

Unlike the streamline method that relies on the given flux field, Fast Marching Method (FMM) provides a direct and intuitive way to characterize the drainage volume using the diffusive time of flight from the Eikonal equation, which can be obtained very efficiently. The drainage volume defined by the diffusive time of flight is basically an extension of the depth of investigation concept to heterogeneous reservoirs. Although the theory of FMM have been well developed and its applications are quite mature (Sethian 1999), the FMM has only been introduced into reservoir engineering recently in the context of unconventional resource revolution (Datta-Gupta et al. 2011). The previous studies have established a basic framework to use the solutions from Eikonal equation solved by FMM (Fujita 2014; Kim 2009; Xie 2012). Based on the diffusive time of flight (DTOF) result in the simulation domain, pressure solution can be further solved either by

numerical or analytical methods. In numerical method, the DTOF is used as the spatial coordinate to reduce 3D diffusivity equation into 1D equations while all relevant physics are solved along the 1D grid, as did in streamline method (Datta-Gupta et al. 2007). In contrast, analytical method is hinged on the asymptotic pressure solution to provide a direct relationship between well production and the associated drainage volume, which can easily extended to simple well test, rate transient and flow regime analysis.

Although these successful applications in unconventional reservoir, there are still many fundamental challenges to overcome in order to improve it to be a useful and robust tool for general applications. First, the asymptotic approach is suitable for transient flow regime in infinite-acting reservoir, boundary effect will induce a significant deviation from its true solution. The new algorithm that takes reflection and multiple arrival phenomena into consideration is required to extend the application to boundary-dominated flow regime.

Second, the fast marching method only considers the first arrival of pressure front and thus can only capture the first touch between pressure fronts from different sources, limited to describe the complex competition between multiple wells. For single well application, Xie et al. (2012) has demonstrated the power of the FMM for drainage volume visualization and subsequent production forecasts in tight gas and shale gas reservoirs. However, for accurate the drainage volume partition between multiple wells, additional information, such as well schedule, should be incorporated into current fast marching algorithm to facilitate the characterization. One direction application with drainage volume partition information in unconventional reservoir is to optimize the horizontal well

spacing, which generally requires massive forward modeling. The traditional finite difference reservoir simulation may not be the best fit for these kinds of applications. Considering the balance between accuracy and efficiency, fast marching based method provides an alternative method to capture the dominant physics, i.e., effective drainage volume in the multiple well interference issue, in a more intuitive and efficient manner.

## 1.4 Objectives and Outline

This dissertation mainly focuses on the coupled fracture propagation and reservoir simulation of multiple hydraulic fracture propagation, as well as multi-well interference with fast marching method. The rest of this dissertation will be organized into three major sections followed by a summary. The specific objectives of each of the three major sections are outlined as follows:

In Chapter II, we will adopt a fully coupled finite element model to simulate both fracture propagation and subsequent well performance for refracturing simulation because the crucial step in this issue is to retain the induced stress and pressure change after initial reservoir depletion. The main objective of the simulation results is to provide a better understanding of: 1) how production affects the in-situ stress change; 2) how proppants impact the nearby fracture propagation; 3) the specific goal to be achieved by the refracturing treatment.

In Chapter III, we will couple a wellbore hydraulics model that considers friction through wellbore and perforation with above fracture model to simulate the simultaneous hydraulic fracturing within a single fracture stage. Through the sensitivity study of number

of clusters, number and size of perforation shot, as well as cluster spacing, we aim to provide insights into how the limited entry technique competes with the stress shadow effects and potentially promotes more uniform fracture development.

In Chapter IV, we will take a closer look at the limitations of existing fast marching method in unconventional reservoirs and extend its application into more general situations where boundary effect and well interference become dominant.

In Chapter V, conclusions of this study and recommended future work are presented.

# CHAPTER II

# MODELING OF REFRACTURING AND WELL PERFORMANCE IN SHALE RESERVOIRS USING COUPLED GEOMECHANICAL MODEL*

The successful development of unconventional reservoir relies on the massive hydraulic fractures which provide high conductive paths and large contact area between matrix and wellbore. Since well production always shows a steep decline after the early high flow rate, refracturing can be an economically promising option to compensate for the loss of production and improve the well delivery.

In this chapter, a series of synthetic cases are used to evaluate the well performance under different refracturing designs. The key characteristics for refracturing simulation is accurate quantification of the depletion-induced stress and pressure field change. Thus, finite element method is used to solve the coupled reservoir flow and geomechanics model while a cohesive zone model is adopted to simulate the fracture propagation. A viscoelastic model is used to simulate the time-dependent fracture conductivity change due to proppant embedment. The synthetic cases are grouped into two categories: refracturing in existing perforations and in newly created perforations. A systematic sensitivity study is performed on the effects of fracturing spacing, matrix permeability and refracturing time.

---

*Reprinted with permission from "Simulation of Coupled Fracture Propagation and Well Performance under Different Refracturing Designs in Shale Reservoirs" by Huang, J., et al. 2016: Paper SPE-180238-MS Presented at the SPE Low Perm Symposium in Denver, Colorado, USA, 5–6 May 2016. Copyright 2016 Society of Petroleum Engineers.

Numerical results show different fracture configurations for refracturing in depleted and virgin reservoirs and thus demonstrate the importance of accounting for stress and pressure changes during initial production. Refracturing the existing perforation is likely to create a wider but shorter fracture compared to the virgin case because the fracturing fluid in these fractures encounter less resistance for enlarging fracture width rather than fracture length because of reduced pressure and total stress. Refracturing new perforations appears to give better short-term performance than refracturing existing perforations but worse long-term performance. Simulation results indicate that for relatively low permeability reservoir it is favorable to add more fracture area; however, the advantage is diminished while for relatively high permeability reservoir where the SRV might already be depleted. When proppant degradation is severe, and fracture conductivity is the limiting factor for production, refracturing existing perforations becomes more attractive. Moreover, simulation results seem to indicate an optimum time window exists for refracturing in this scenario.

## 2.1 Introduction

Unconventional resources such as shale gas have taken a significant share in the energy supply in the US and the world energy market (Holditch 2010). The advent and growth of the development of these resources have been driven largely by the advances in technologies such as horizontal well drilling and multistage hydraulic fracturing. However, one big issue in unconventional reservoirs is the rapid decline of production rate in the early few years. Refracturing has been proved to be an effective remedial operation to

exploit more shale resources by re-stimulating the reservoir. Some important conclusions have been generated by analyzing several field cases. Vincent (2010) explored various field cases to emphasize the different mechanisms responsible for production improvement achieved by refracturing, such as increased fracture length, choice of suitable fracture fluids and improved conductivity. Craig et al. (2012) discussed some possible reasons for improved well performance with refracturing based on simulation and history matching on Bakken wells. Jayakumar et al. (2013) performed a series of refracturing modeling under different scenarios in shale reservoir to understand the permeability range and existing fracture spacing under which refracturing might be beneficial. Overall, the rationale of refracturing is to either achieve a larger simulated reservoir volume (SRV) than initial fracturing or restore the existing fracture conductivity. The requirement for refracturing can be due to various reasons such as initial inefficient completion, proppant degradation, near wellbore damage and pressure depletion. Consequently, we need to understand specifically what needs to be accomplished by the refracturing treatment before any operation. To develop an appropriate refracturing strategy, it is critical to understand the important mechanisms involved this complex process such as the stress change due to the pressure depletion and the impact on the proppants from the original fractures on the fracture propagation during refracturing. The numerical simulation is an economical tool to understand above issues and provide the optimized solution.

To simulate the complex fracture development and potential fracture interference, advanced numerical methods have been extended in recent years to be able to simulate the

sophisticated hydraulically-drive fracture propagation, such as boundary element method (BEM) (Huang et al. 2014; Sesetty and Ghassemi 2015; Wu and Olson 2013), discrete element method (DEM) (Nagel et al. 2011; Zhou et al. 2016b), finite element method (FEM) with cohesive zone method (CZM) (Haddad and Sepehrnoori 2014; Shin and Sharma 2014; Wang et al. 2016; Yao et al. 2010), as well as the extended finite element method (XFEM) (Dahi-Taleghani and Olson 2011; Zielonka et al. 2014). Among these methods, the boundary element method has been proved to be efficient because it only discretizes the boundary but it is also limited to elastic homogeneous medium. More importantly, since it focus on the fractures, the important pressure diffusion mechanism in the porous medium has been not ignored. Particle-based methods like discrete element method are powerful to help understand the fundamental physics of fracture initiation and propagation, as well as naturally suitable to simulate the complex fracture network. Due to the limitation of particle sizes, these methods are very hard to apply to the field-scale problems at current computational capabilities. Therefore, finite element related methods are able to incorporate the important physics involved in the complex nonlinear interaction between rock and fluid and thus believed to be most promising for resolving engineering problems. As a well-developed model, CZM has been demonstrated for simulating the fracture propagation in the predefined path (along the element interference) accurately and robustly. The main limitation of this model is the planar fracture assumption. XFEM is a relatively new method that allows fracture to cross the individual element and thus is able to simulate the nonplanar fracture propagation, however, this method is still under

development and not yet applied to large scale problems, especially for fluid-driven fracture.

On the other side, in order to accurately evaluate the production performance of the generated fracture systems, the explicit representation of discrete fractures are generally required. As a result, the demand on advanced meshing and domain discretization technique is rising because the Cartesian and corner-point grid systems, commonly used in conventional reservoir simulator, are no longer sufficient to accurately represent the complex fracture system. Compared with separated fracture and reservoir simulators, fully coupled models have the advantage to avoid the solution mapping between meshes used in different simulations, which is critical for refracturing simulation that involves two-way solution transfer.

In this chapter, a fully coupled poroelastic model is used to simulate both hydraulic fracture propagation and well performance, which can not only capture the complex fracture propagation process in multistage sequential hydraulic fracturing but also production simulation along with proppants degradation. We adopt CZM to simulate the planar fracture propagation by assuming that the out-of-plane deflection is negligible. Bunger et al. (2012) provides a detailed algorithm to predict when it is valid to neglect the fracture path deflection and use the planar model. The entire simulation is performed based on the commercial finite element package ABAQUS platform, which provides a powerful interface for user-defined material and element properties, as well as the complex initial and boundary condition variation through customized subroutines in FORTRAN. The

ultimate goal of this chapter is to provide insights into various refracturing strategies under different reservoir and completion conditions.

## 2.2 Methodology

The commercial fracture simulators and reservoir simulator are typically separated in different packages from different vendors. For a complete workflow in unconventional development, these two parts need to be integrated together and in most situations the additional software is required to map and upscale the generated fracture geometry from fracture simulator to reservoir simulator. There are some major issues caused by the weak coupling between fracture and reservoir simulators: 1) reservoir flow part (poroelastic effect) is generally ignored during fracture propagation process in the fracture simulator where the leaked fracturing fluid concentration near fracture surface and tip is important to capture the effective stress distribution; 2) production induced stress change is not considered in reservoir simulator which is crucial for refracturing and infill drilling simulation; 3) the complex fracture geometry requires unstructured gridding which is not readily available in most commercial reservoir simulators.

The major advantage of the fully coupled model in ABAQUS is that the fracture propagation and production simulation can be performed on the same grid system (structured or unstructured) so that the induced stress and pressure change are retained for both refracturing and subsequent production simulation. Moreover, the fracture conductivity mapping/upscaling is avoided. The disadvantage of this fully coupled model is the computational cost and the assumption of single phase flow. The following sections

summarize the key theories used in ABAQUS for modeling reservoir, fracture propagation and flow within the fracture. For detailed description, the reader is referred to the manual (Simulia 2014).

### *2.2.1 Reservoir Model*

The reservoir system involves two sets of governing equations that describes the balance of momentum and mass conservation of a slightly compressible single phase fluid. The fully coupled geomechanics and fluid flow in the porous medium is modeled approximately using the conventional continuum approach by linking the finite element mesh to the solid phase, where the liquid is allowed to flow through. The effective stress principle is adopted to describe its mechanical behavior, where the total stress $\sigma$ consists of effective stress $\sigma'$ and pore pressure $p$

$$\sigma = \sigma' + \alpha p \tag{2.1}$$

where $\alpha$ is Biot's coefficient and is treated as unit for simplicity, $\sigma'$ is the effective stress that actually governs the mechanical behavior of the rock. In the finite element method, conservation of momentum is expressed in form of the principle of virtual work for the domain in its current configuration

$$\int_V \sigma' : \delta\varepsilon dV = \int_S \vec{t} \cdot \delta\vec{u} dS + \int_V \vec{f} \cdot \delta\vec{u} dV \tag{2.2}$$

where $\delta\varepsilon$ and $\delta\vec{u}$ are virtual rate of strain and displacement, $\vec{t}$ and $\vec{f}$ are the surface traction per unit area and body force per unit volume. Similarly, the mass flow balance equation is written in a variational form required by finite element approximation

$$\frac{d}{dt}\int_V \rho\phi dV + \int_S \rho\vec{q}\cdot\vec{n}dS = 0 \tag{2.3}$$

where $\rho$ and $\phi$ are density of fluid and porosity of reservoir, respectively. The vector $\vec{n}$ is the outward normal direction to the surface *S* and the flow rate is $\vec{q}$ described by Darcy's law. By using the backward Euler approximation, the mass conservation equation is integrated in time. Eventually, the above fully coupled equations will be solved by the Newton iterations.

### *2.2.2 Fracture Propagation Model*

Conventional linear elastic fracture mechanics (LEFM) assumes pure elastic behavior and predicts that a fracture will propagate as long as the stress intensity factor reaches the material toughness by ignoring the critical process zone, which is a small region near the fracture tip where the inelastic behavior occurs. This assumption fails when used to predict the fracture propagation in ductile and quasi-brittle rocks such as shales. The cohesive zone method which considers the process zone near fracture tip is able to capture the nonlinear material behavior near fracture tip based on the energy criterion that states the fracture will start to propagate when the energy release rate reaches the critical fracture energy.

The cohesive zone is a single thin layer that is embedded at the interface between continuum elements to represent the cohesive intermolecular force. This force reflects the intermolecular strength and is much stronger than the macroscopic strength of material. For simplicity, the bilinear traction-separation (T-S) law is used to describe this

constitutive behavior of the cohesive zone, as shown in Figure 2.1, which assumes that it exhibits the linear behavior before reaching the traction limit $T_0$ where damage initiates, followed by the linear reduction until the complete failure. The critical energy of material $G^c$ is area under this triangle, which is related to material toughness.

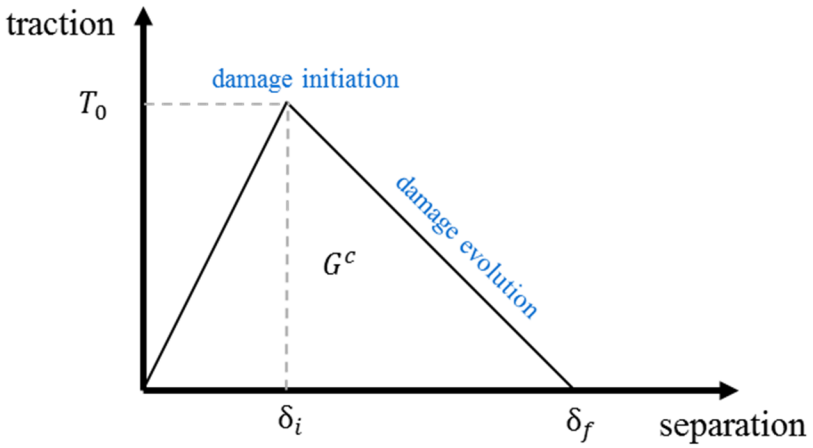


**Figure 2.1 Bilinear traction-separation law for fracture opening in cohesive element**

The progressive damage process involves two critical stages: damage initiation and damage evolution. One of the commonly used damage initiation criteria is the quadratic function based on the nominal stress where the three possible failure modes are integrated together

$$\left(\frac{\langle t_n \rangle}{t_n^0}\right)^2 + \left(\frac{t_s}{t_s^0}\right)^2 + \left(\frac{t_t}{t_t^0}\right)^2 = 1 \qquad (2.4)$$

where $t_n$, $t_s$, $t_t$ are the normal, the first and second stress components; $t_n^0$, $t_s^0$, $t_t^0$ are corresponding strength when the deformation is purely normal to the surface or along the first or second shear direction. The Macaulay brackets $\langle\ \rangle$ above are used to indicate that

the purely compressive deformation or stress state does not contribute to the damage. Once the damage initiates, the stress components will be degraded accordingly

$$t = (1 - D)\bar{t} \tag{2.5}$$

where $\bar{t}$ are stresses predicted by the perfect linear elastic assumption and $D$ is the scalar damage variable to describe the extent of damage (Turon et al. 2006). When $D$ = 1, the material becomes completely damaged and fracture is generated. The relative contribution of normal and shear deformation is quantified by the mixed-mode developed by Benzeggagh-Kenane (Benzeggagh and Kenane 1996). By assuming that critical fracture energies during deformation along the first and second shear directions are similar, the criterion is defined as

$$G^c = G_n^C + \left(G_s^C - G_n^C\right)\left(\frac{G_S}{G_T}\right)^\eta \tag{2.6}$$

where $G_n^c$ , $G_s^c$ are critical fracture energies in mode I and II that can be calculated using Griffith and Irwin's equation (Kanninen and Popelar 1985); $G_S$ and $G_T$ are the summation of work done by traction in shear direction only or in both normal and shear directions, respectively. The exponent $\eta$ is a material parameter that determines the contribution of shear mode to the total critical energy and equal to 2 for brittle material and 3 for ductile material. When the accrued fracture energy reach the critical energy $G^c$, the cohesive element is completely fractured.

It is important to point out that complex constitutive models with significant stiffness degradation, such as above cohesive traction-separation law, often have difficulty

in convergence. One of the numerical techniques to overcome these convergence difficulties is to use the viscous regularization of the constitutive equations, which renders the stiffness matrix of the softening/degraded material to be positive definite for sufficiently small time increment. The appropriate value of the viscosity parameter that results in the reasonable balance between improved convergence of the nonlinear system and the acceptable accuracy of numerical results is problem dependent and requires the experience and discretion of the user. The larger values of viscosity regularization provides better convergence at the cost of accuracy of the results. If no convergence problem is encountered, the zero value will be preferred. For our calculations, a dampening value from $10^{-4}$ to $10^{-6}$ is used because it doesn't affect the results too much but improve the convergence obviously.

### *2.2.3 Reservoir Flow Model*

The fracture flow is represented by the cohesive element where the fluid flow continuity within the fracture (tangential flow) and through the fracture surface (normal flow) is maintained. For the tangential flow, this model provides a smooth transition to approximate the changing nature of fluid flow from the initial Darcy flow in undamaged status to Poiseuille flow (gap flow) when fracture initiates and evolves. Poiseuille flow refers to the steady viscous flow between two parallel plates and its volumetric flow rate under unit thickness can be written in the form similar to Darcy law

$$q_t = -k_t \nabla p_f \tag{2.7}$$

where $k_t$ is the tangential resistance to the fluid flow and $p_f$ is the pressure in the fracture. A variety of fluids have been used for hydraulic fracturing such as slickwater, linear gels, crosslinked gels and foams. For a Newtonian fluid, the tangential resistance using Reynold's equation is defined as

$$k_t = \frac{w_f^3}{12\mu} \tag{2.8}$$

where $\mu$ is the fluid viscosity and is $w_f$ the fracture width. Similarly, for a power law fluid, the constitutive relation is defined as

$$\tau = K\dot{\gamma}^{\alpha} \tag{2.9}$$

where $\tau$ is the shear stress, $K$ is the fluid consistency, $\dot{\gamma}$ is the shear strain rate and $\alpha$ is the power law coefficient. Thus, the corresponding tangential resistance is defined as (Simulia 2014)

$$k_t = \left(\frac{2\alpha}{1+2\alpha}\right)\left(\frac{1}{K}\right)^{\frac{1}{\alpha}}\left(\frac{w_f}{2}\right)^{\frac{1+2\alpha}{\alpha}}\|\nabla p\|^{\frac{\alpha}{1-\alpha}} \tag{2.10}$$

It is worth noting that the above definition is used during fracturing process. During the production simulation, to consider the effect of proppant settling in the fracture, the above tangential resistance should be calibrated to match the experimental permeability of proppant pack, which is to be described in the next section.

For the normal flow, it simulates the fluid leakoff and reflects the resistance due to the effect of filter cake. The pressure-dependent leakoff model is used to describe the normal flow through the fracture surface

$$q_n = C_L \left( p_f - p_m \right) \tag{2.11}$$

where $C_L$ is the fluid leakoff coefficient that can be interpreted as the permeability of a finite layer of filter cake on the fracture surface, and $P_m$ is the pore pressure in the adjacent formation. The coefficient used in this 1-D leakoff model can be defined as a time-dependent value by user to mimic the filter cake buildup and time dependent resistance.

### *2.2.4 Proppant Model*

Proppants are essential in shale formation fracturing to maintain the opening of generated fractures and provide a highly conductive path for reservoir fluid flow into the wellbore. Current reservoir simulation implicitly considers the proppant by using facture compaction multiplier derived from the short term conductivity, measured in laboratory up to 48 hours, as a function of closure stress, which is the difference between minimum horizontal stress and the pressure in the fracture. Figure 2.2 illustrates an example relationship between proppant permeability and closure stress.

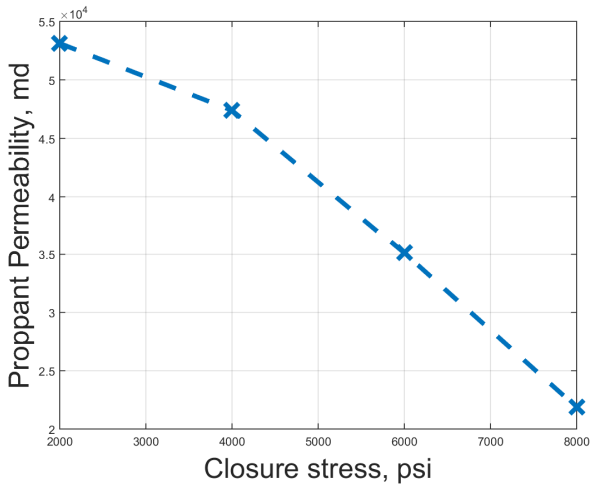


**Figure 2.2 Proppants permeability versus closure stress for Jordan Unimin 40/70**

In practice, however, the reference or baseline conductivity data are always optimistic and actual fracture conductivity is much lower than expected (Barree et al. 2003). The discrepancy is attributed to various kinds of physical and chemical detrimental effects on both proppant pack and contacting rock under the realistic reservoir conditions in the long term. For instance, proppant fines, particles breaking off of the proppant grain, can cause serious degradation of conductivity, e.g., 5% proppant fines can result in 62% reduction in proppant pack flow capacity (Coulter and Wells 1972). Proppant embedment, as shown in Figure 2.3, has been known to reduce the fracture width and hence fracture conductivity based on decades of field history. This embedment becomes worse with the increase of production time as the result of rock creep deformation, especially in the shale reservoir containing high clay content (Sone and Zoback 2010). Geochemical studies have demonstrated that under certain stress and temperature fractures would heal with time by a mechanism called pressure dissolution, where minerals at grain-to-grain contacts under high stress will dissolve and deposit into regions of relatively low stress such as pore spaces (Weaver et al. 2014). Terracina et al. (2010) summarize some mechanisms that significantly damage the proppants and also evaluate the resulting production using field evidence.

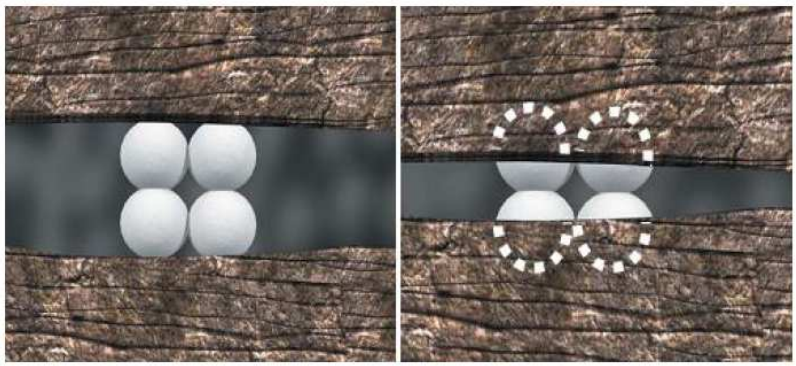

**Figure 2.3 Proppant embedment into the fracture face reduces fracture width and conductivity (from Terracina et al. (2010)).**

Realizing that time-independent proppant conductivity may not be appropriate for long term simulation, Weaver et al. (2014) patented an experiment method, spanning several months to years, to determine the time-dependent conductivity of aged proppants and quantify proppant strength loss under the long term exposure to the geothermal and chemical reactions, regardless of stress in the reservoir. Guo and Liu (2012) propose an analytical model for proppant embedment by using a viscoelastic model to describe rock creep deformation, which reduces fracture width with time. By using finite element method, Glover et al. (2015) propose a viscoelastic model for assessing the fracture conductivity under short and long term loading when material properties can be determined. Although published data on long-term performance of fracture conductivity is limited so far, it should not preclude us from considering a way to incorporate both stress- and time-dependent conductivity into production simulation.

In our finite element simulation, the proppant pack, which is an arrangement of proppant particles, is explicitly represented using the continuum elements with equivalent

mechanical and transport properties, as shown in Figure 2.4. Strictly speaking, the equivalent properties should not reflect only the properties of proppants but the interaction behavior between proppant pack and contacting rock under reservoir conditions which needs to be calibrated by experimental and field data. The combined effect of aforementioned detrimental mechanisms on both proppants and contacting rock is approximated by introducing a linear viscoelastic model into proppant pack, where the fracture width reduction with time is realized by the degradation of the equivalent proppant pack modulus. The early time fracture closure is dominated by the equivalent elastic property of proppant pack while late time closure could be controlled by the viscous property if degradation is serious. As a result, the fracture width and conductivity become the functions of both stress and time. Specifically, the proppant pack is assumed to be the linear, isotropic and viscoelastic material defined by a Prony series expansion of the relaxation modulus (Simulia 2014):

$$Y(t) = Y_0 \cdot \left[ 1 - \sum_{i=1}^{n} p_i \left( 1 - e^{-t/\tau_i} \right) \right] \tag{2.12}$$

where $Y_0$ is the instantaneous modulus of the material, $p_i$ is the $i$'th Prony constant and $\tau_i$ is the $i$'th Prony retardation time constant. Generally, the Prony constants could be obtained by fitting the experimental data or converted from the classical viscoelastic constitutive models such as Maxwell model, Kelvin model and Burger's model (Kong and Yuan 2010).


**Figure 2.4 Proppants in the FEM model represented by continuum elements**

The initial fracture conductivity estimation is based on the relationship between proppant permeability and closure stress, as well as the effective proppant pack width (using datasource from StimLab). For the unknown proppant, Barree et al. (2016) provide the generic correlations to determine the proppant pack baseline conductivity based on minimal information. For any specific proppant schedule, we first calibrate the elastic property of our model to match the measured fracture conductivity at the initial time and then use aforementioned viscous property to describe the degradation behavior that reflects the equivalent effect of all kinds of detrimental mechanisms on fracture conductivity. Overall, using the linear viscoelastic model may not be an ideal solution to accurately capture the complex interaction behaviors between proppants and rock formation, but at least it provides a compromised but feasible way to incorporate both stress- and time-dependent fracture conductivity into production simulation, considering this physics is missing in most simulation studies.

### *2.2.5 Refracturing Strategies*

Refracturing on the current wells is recognized as an economical alternative to infill drilling and has been proved to be an effective method to enhance the well performance

when original fractures are neither adequate to access enough reservoir volume nor sufficient to provide a conductive path for fluid flow into wellbore. Correspondingly, various refracturing practices can be generally classified into two categories: refracturing existing perforations and new perforations. Refracturing existing perforations are widely used to clean-up the degraded proppants and restore or enhance the original fracture conductivity. It can also be adopted to increase the propped fracture length and the associated stimulated reservoir volume. On the other hand, refracturing new perforations is used to either increase the fracture surface contact area with reservoir in extremely low reservoir or stimulate the new reservoir that has not been accessed by original fractures. The potential new perforation locations are most likely to locate in the middle between original fractures which have enough spacing to accommodate new fractures. Infill drilling and fracturing at neighbor well is beyond the scope of this comparative study. The sensitivities of critical factors, such as formation permeability, stage spacing and refracturing time, will be performed for these two different refracturing strategies.

### *2.2.6 Refracturing Procedure*

The life time simulation of a horizontal well with both initial fracturing and refracturing consists of a series of critical operational steps with different dominant mechanisms. In this integrated workflow, the whole simulation analysis are divided into following seven simulation steps:

1. An initial balance step is used to check and ensure that the equilibrium of the whole reservoir system is achieved after applying the initial pore pressure and in-situ

stresses to the formation. This is particularly important when complex initial and boundary conditions or the heterogeneities are introduced in the system.

2. The second step simulates the hydraulic fracturing process where a specified volume of fracturing fluid is injected stage by stage. Injection flow at a rate of 40 barrels per minute is assigned to the perforation point which is initially open to permit entry of fluid. The duration of is 20 minutes for each fracture stage. After pumping each fracture stage, a crucial boundary condition is applied: the proppant elements inside will be activated after each fracture stage to support the fracture surface opening and to mimic the behavior of the proppants that were injected into the fracture.
3. Following the hydraulic fracture is a shut-in period, where the injection into the well is terminated and the built-up pore pressure in the fracture is allowed to leak off into the formation. The duration typically lasts several hours to days.
4. In the subsequent step, a constant bottomhole pressure constraint is applied to simulate the production behavior. This step ends after several years when refracturing starts.
5. The next step represents the refracturing process, where the same fluid volume as original fracturing is injected to either existing perforations or new perforations that are in the middle between existing fractures. The new proppant elements are introduced to replace the old ones in existing fractures or added into the newly generated fractures.

6. Another shut-in period is followed to allow refracturing fluid to leak off into the formation.
7. At the end, the same constant bottomhole pressure is applied for several additional years of production.

## 2.3 Validation and Applications

### *2.3.1 Fracture Model Validation*

To better understand the fracture growth in space, a fully three-dimensional model coupled with two-dimensional fluid flow within fracture is required. However, such a 3D model generally requires substantial amounts of input data and can be extremely computationally intensive. It has been reported that the simulation of a single 3D hydraulic fracture propagation at the laboratory scale, in some cases, can cost over a month, let alone the multiple-fracture propagation at the reservoir scale. Currently, these fully 3D models are limited mostly to academic research that provides us insights into the fracture-fluid interaction process in 3D space. Since we focus on the effects of depletion on refracturing well performance at the reservoir scale, a 2D plane strain model is adopted to reduce the computational cost while capturing the most critical physics during the hydraulic fracturing process.

The most commonly used 2D analytical fracture propagation models are Perkins-Kern-Nordgren (PKN) (Nordgren 1972; Perkins and Kern 1961) and Khristianovich-Geertsma-DeKlerk (KGD) (Geertsma and De Klerk 1969; Khristianovic and Zheltov 1955), which assume plane strain deformation with constant fracture height. Although

they have limitation in the applications and have been gradually replaced by more complex models, they still serve as a benchmark for the numerical fracture propagation models. Therefore we use the analytical solution of KGD model (Valko and Economides 1995) is used to validate the numerical 2D model with constant fracture height. The input parameters for typical shale reservoirs are listed in the Table 2.1.

| **Parameter** | **Value** | **Unit** |
|---|---|---|
| Young's Modulus | 2.58E6 | psi |
| Poisson's Ratio | 0.3 | - |
| Fracture Toughness | 2000 | $psi*in^{1/2}$ |
| Reservoir Permeability | 100 | nd |
| Porosity | 4.3 | % |
| Reservoir Oil Viscosity | 0.36 | cp |
| Total Compressibility | 3.6E-6 | $psi^{-1}$ |
| Initial Reservoir Pressure | 4850 | psi |
| Producing Bottomhole Pressure | 2000 | psi |
| Minimum Horizontal Stress | 7900 | psi |
| Maximum Horizontal Stress | 8300 | psi |
| Overburden Stress | 11000 | psi |
| Reservoir Thickness | 200 | ft |
| Injection Rate | 40 | BPM |
| Injection Time | 20 | min |
| Fracturing Fluid Viscosity | 1.2 | cp |
| Fracture Height | 200 | ft |
| Leakoff Coefficient | 1E-6 | ft/(psi*s) |

**Table 2.1 Input parameters for a typical shale reservoir**

Figure 2.5 shows the comparisons of KGD model with numerical model for the fracture width at injection point and injection bottomhole pressure. Overall, the numerical simulation produces close results with analytical model, but the discrepancy is obvious at the early time. There are several factors that contribute to the difference. One critical contributing factor is that the numerical model simulates the fracture initiation process, capturing the fracture "breakdown" pressure, while the KGD analytical model doesn't. To avoid numerical convergence difficulty, the injection rate linearly ramps up to the constant rate in first 3 minutes in the simulation model while a constant injection rate is assumed in analytical model. Secondly, the numerical model considers the coupling effect between rock and fluid, where it is difficult to get the analytical solution for the coupling process. In addition, another important mechanism that has been ignored in KGD model is the leakoff, which contributes to the faster pressure decline in numerical results.

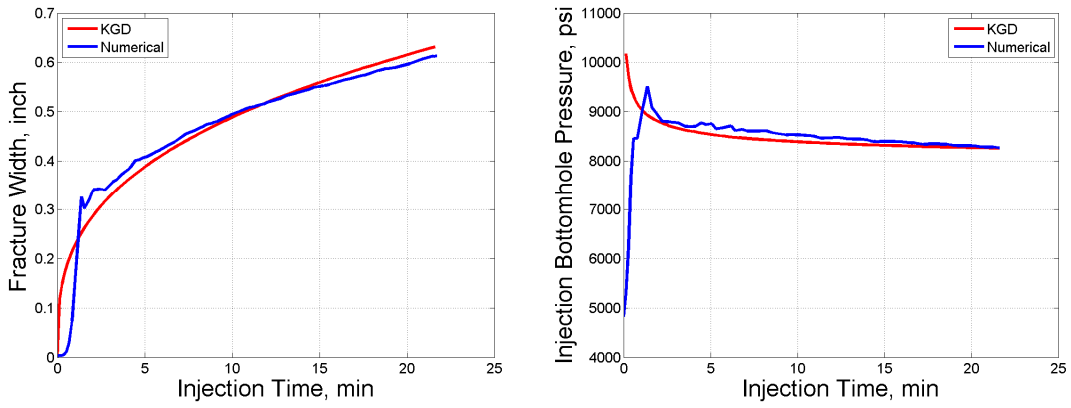


**(a)** **(b)**

**Figure 2.5 Comparisons of numerical model with KGD model: (a) fracture width at injection point; (b) injection bottomhole pressure.**

### *2.3.2 Proppant Model Validation*

We have proposed a new way to consider both stress- and time-dependent fracture conductivity by using an equivalent viscoelastic model to represent the interaction behavior between proppant and contacting rock formation. The time-dependent fracture conductivity has attracted the industry's concern and the related experiments are undergoing but the results are not available at the time of publication (Weaver et al. 2014). However, when the time-dependent (viscous) effect is very small and negligible, for some kinds of proppants and formation, the viscoelastic model will be reduced to the elastic model to capture the stress-dependent fracture conductivity, which is measured in short term.

To validate this ability of our model, we build a verification model to match the laboratory fracture conductivity test (Alramahi and Sundberg 2012), where the proppants are confined within two rock samples, as shown in Figure 2.6. The fracture is fulfilled with the proppant elements. The confining rock is relative rigid and width change is controlled by the mechanical deformation of proppants, so that it can simulate the equivalent fracture width reduction induced by both proppants crushing and embedment using the nonlinear large deformation analysis. The equivalent Young's modulus and Poisson ratio for the proppant pack after calibration is 6E3 psi and 0.2. We assign an extremely large value to the viscosity coefficient to eliminate the viscous effect. The corresponding fracture conductivity is calculated based on the cubic law, which has been shown to accurately capture the fracture conductivity over a certain range of closure stress in shale (Kassis and Sondergeld 2010). By increasing the confining stress from 500 psi to

5700 psi, we can produce the close results with the measured fracture conductivity, as shown in Figure 2.7. This validation can approve the ability of the proposed viscoelastic model to capture conventional stress-dependent fracture conductivity behavior when time-dependent effect is not significant.

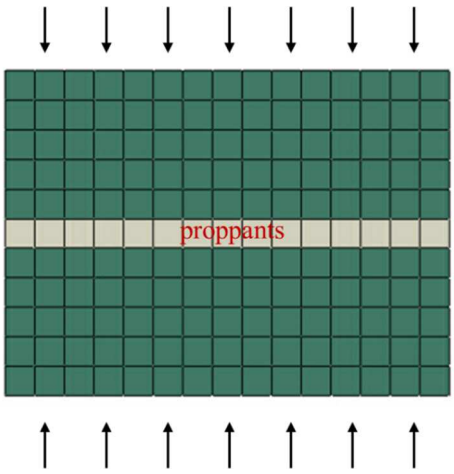


**Figure 2.6 Verification model for fracture conductivity test**

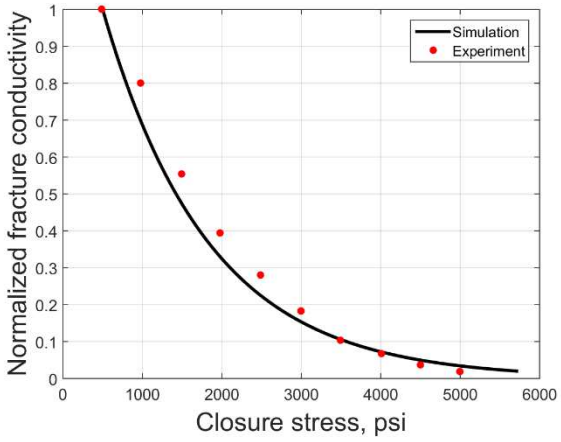


**Figure 2.7 Comparison of the fracture conductivity from proposed model and the directly measured data (Alramahi and Sundberg 2012)**

### *2.3.3 Effect of Depletion on Refracturing Geometry*

The major difference between refracturing and initial fracturing is that the reservoir conditions, such as pressure and stress, have changed due to the depletion. Without accounting for these effects, majority of the refracturing simulation work in the literature assume exactly the same re-fracture geometry as in the original fracture when using the same pumping schedule (Haddad et al. 2015; Jayakumar et al. 2013; Tavassoli et al. 2013). These assumptions need to be well examined before reaching the conclusions, and it may induce biased fracture geometry, especially when depletion effect is strong. In this section, we use a single fracture case to demonstrate the importance of reservoir pressure depletion on refracturing fracture propagation by comparing the fracture geometry in both depleted and virgin reservoirs with the same pumping schedule. Figure 2.8 shows the pressure depleted map of a closing single hydraulic fracture during the first 3 years production under the constant bottomhole pressure constraint. This single fracture is generated under 20 minutes injection and we allow the fracture to be gradually closed within 3 years as a consequence of the proppant degradation due to embedment, crushing and fines migration. By doing this, we have generated a closed fracture in the depleted zone, which is used to compare with the same fracturing schedule but in the virgin reservoir.

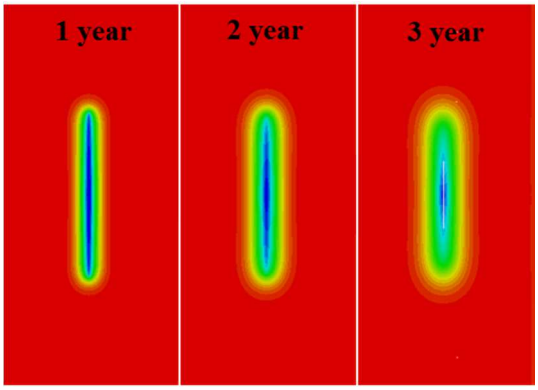


**Figure 2.8 Pressure depletion of gradually closing hydraulic fracture during 3 years production**

Figure 2.9 shows the comparison of fracture width against half-length, as well as corresponding fracture geometry map, for both depleted and virgin cases after 20 and 40 minutes injection, respectively. The solid line indicates the results at 20 minutes while dash line represents 40 minutes. In the virgin reservoir, the fracture width has the elliptical shape along fracture length direction. In the depleted reservoir, since total stress is decreased due to pressure depletion, the fracture is under smaller confinement so it is prone to grow wider compared with virgin case. This phenomenon also indicates that if we use the same pumping volume as initial fracturing for refracturing the previously completely closed fracture, it will only enhance the conductivity but not increase fracture length. To acquire a longer fracture, the larger pumping volume than initial is required. However, even with larger pumping volume, when the fracture propagates outside the major depletion zone, the fracture width drops drastically due to the stress contrast. As can be seen from Figure 2.9, after 40 minutes injection, half-length in depleted case only increases 23% from 315 ft to 387 ft, while for virgin case half-length increases 78% from 295ft to 525 ft.

According to above comparison, refracturing the existing perforation is more likely to create a wider but shorter fracture length compared with virgin case because fluid in the fractures has encountered less resistance in the depletion zone as a result of reduced pressure and total stress. The above fracture geometry contrast also demonstrates the importance of accounting for depletion-induced stress and pressure change in refracturing simulation. Thus, assuming the same fracture geometry for refracturing in depleted zone as the initial fracturing may not be appropriate and depletion effect has to be taken into consideration in refracturing simulation.

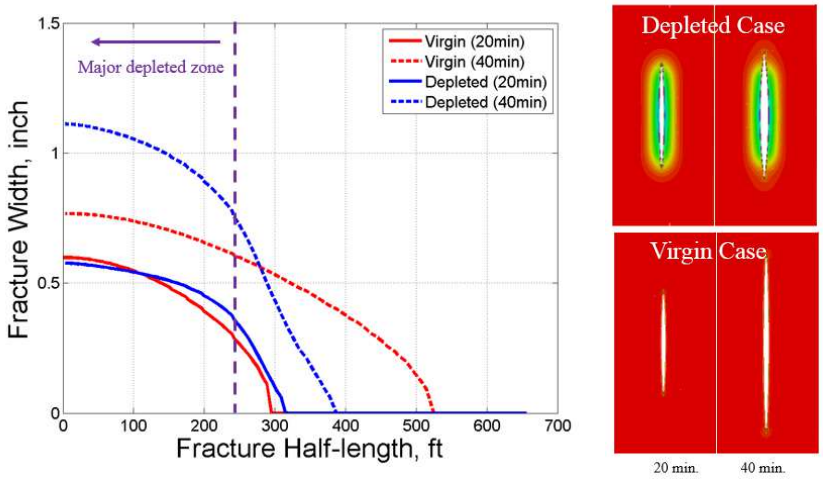


**Figure 2.9 Fracture profile comparison after 20 and 40 minutes injection (fracture width is magnified by factor 300)**

### *2.3.4 Multi-stage Sequential Hydraulic Fracturing*

In this section, we will compare different refracturing strategies using a horizontal well model with three fracture stages. In order to better capture the transient behavior around the fracture tip and leakoff behavior near the fracture surfaces, we utilize the tartan grid, as shown in Figure 2.10. The two refined regions between stages are reserved for modeling

refracturing process at new perforations. The stage spacing considered here is 200 ft and all other parameters are listed in Table 2.1. In this multi-stage sequential fracturing simulation, we assume there is only one dominant fracture in each fracture stage.

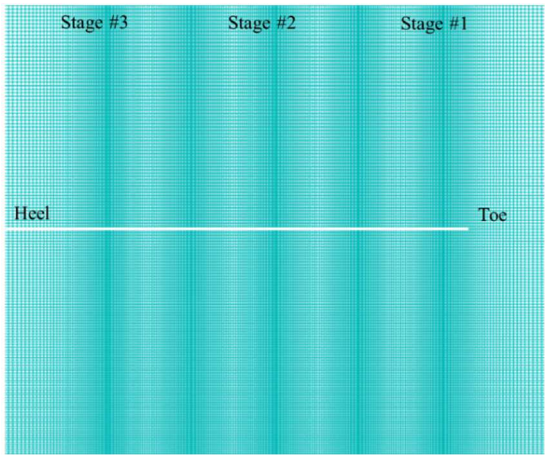


**Figure 2.10 Finite element mesh for a horizontal well with multiple transverse fractures**

Stress shadow effects from previous stages is introduced naturally by using proppants to maintain the opening of previous fractures. This treatment is of much advantage compared with constant displacement boundary condition that is widely used in most of previous works. By doing this, we allow the mutual influence between new and existing fractures, while constant displacement boundary condition does not allow the movement of existing fractures and only considers the one-way influence of existing fractures on current fracture, which significantly exaggerate the stress shadow effect.

Figure 2.11 shows the fracture width and length evolution during the multi-stage sequential fracturing process. The fracturing order is from toe to heel, which is from right to left in the plot. From the pictures we can observe that the first fracture stage has the

largest fracture width while the second fracture stage has the smallest width but a little longer length. The maximum width for these fractures (from right to left) are 0.6 inch, 0.46 inch and 0.5 inch, while the corresponding full fracture length are 580 ft, 620 ft and 592 ft. This variation is due to the stress shadow effect from propped fractures in previous stages. According to the stress distribution around the propped fracture, the induced stress perturbation (or stress shadow) at a particular point is a function of distance to the propped fracture and its fracture width (Warpinski and Branagan 1989). When pumping the first stage, there is no additional stress perturbation, so it is only under the in-situ stress and results in the maximum fracture width. For the second fracture stage, it is under the additional stress shadow of first stage and thus has a smaller fracture width but larger length due to the same fracturing volume. For the third fracture stage, it is under the stress shadow of both first and second stages. However, since the stress shadow effect declines fast with distance and the second stage has a smaller width, the accumulated stress shadow effect in third stage due to previous two stages is even smaller than that in second stage due to only first stage. As a result, in the picture we can observe that third stage has a relative larger width compared with second stage. It is worth to note that this conclusion will vary depending on the fracture spacing, pumping schedule, in-situ stress and formation properties.

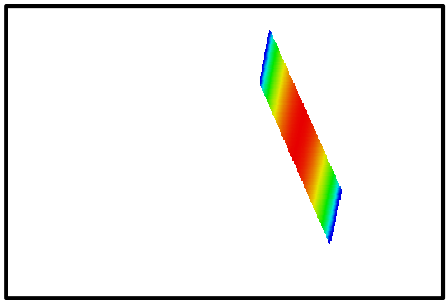

**(a) after first stage**

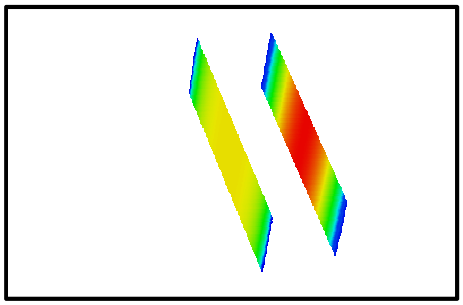

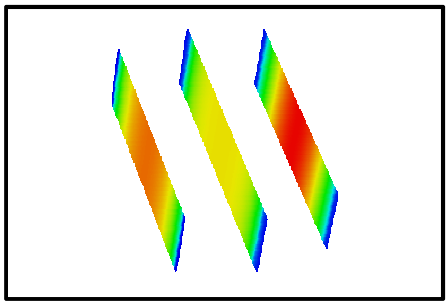

**(b) after second stage** **(c) after third stage**

**Figure 2.11 Fracture profile for multi-stage sequential hydraulic fracturing (spacing = 200 ft)**

### *2.3.5 Effect of Fracture Compaction*

The effective fracture conductivity is related to the performance of proppant pack under certain reservoir conditions. Guideline for proppant selection is to choose these with high proppant strength to withstand closure stress and avoid crushing or embedment. Table 2.2 shows the properties used in our simulation for modeling the proppant pack. We use three different equivalent viscosity coefficients in the viscoelastic model to cover a wide range of the various long-term sustainability of proppants. The corresponding values are listed in Table 2.3, which reflects the averaged deterioration rate of proppants and contacting rock. We use the three values as representatives for strong, medium and weak proppants. It should be clarified that, the term ‘strong’ or ‘weak’, used in this research, only reflects

the resistance of proppants to crushing, embedment, and pressure dissolution. For example, the curable resin coated sand is more 'stronger' than uncoated sand in our categorization.

| Parameter | Value | Unit |
|---|---|---|
| Mean Diameter | 0.01 | inch |
| Equivalent Modulus | 6E3 | psi |
| Initial Closure Stress | 3050 | psi |
| Initial Pack Permeability | 2E4 | md |
| Pack Porosity | 0.35 | - |
| Propped Fracture Concentration | 2.0 | $lbm/ft^2$ |

**Table 2.2 Properties for proppant pack**

| Parameter | Strong | Medium | Weak |
|---|---|---|---|
| Equivalent Viscosity Coefficient (MPa*s) | 13.6E9 | 6.8E9 | 3.4E9 |

**Table 2.3 Viscoelastic parameter for proppant pack**

In the Figure 2.9, we have already seen that the fracture width is not uniform but decreasing from wellbore to fracture tip. Due to this width variation, these fractures will have the non-uniform fracture conductivity distribution along fracture length. The initial maximum fracture conductivity, which occurs at the injection point of first fracture, is calibrated to 20 md-ft under 7900 psi, while the conductivity at other locations can be calculated accordingly. The long-term fracture conductivity reduction depends on the properties of proppants. Figure 2.12 shows the reduction of normalized fracture

conductivity with production time for the three kinds of proppants. The normalized fracture conductivity is defined as the actual fracture conductivity divided by the initial fracture conductivity. As shown in Figure 2.10, the conductivity reduction can generally be as high as several order of magnitudes. Chances are that the conductivity of fractures will turn to be the bottleneck of production after significant reduction.

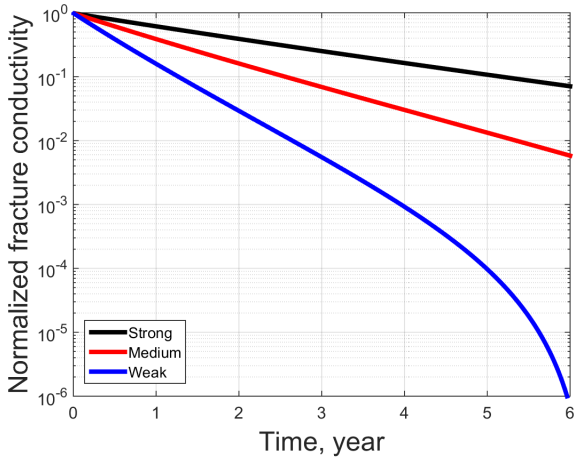


**Figure 2.12 Variation of the normalized fracture conductivity with time for different proppants**

Figure 2.13 and Figure 2.14 compares the pressure depletion maps for different proppants after 3 and 6 years production, respectively, while the corresponding production rate variation as a function of time is shown in Figure 2.15. As can be seen from the plots, with weaker proppants, the fracture width reduces much more and the corresponding production rate declines much faster after the first year. By considering the realistic fracture width variation along fracture length, these fractures will close gradually from tip to center. For example, at the third year, the majority of fractures with weak proppants are

closed, the corresponding rate is very low; while at 6th year, these fractures are almost fully closed and the corresponding rate becomes negligible.

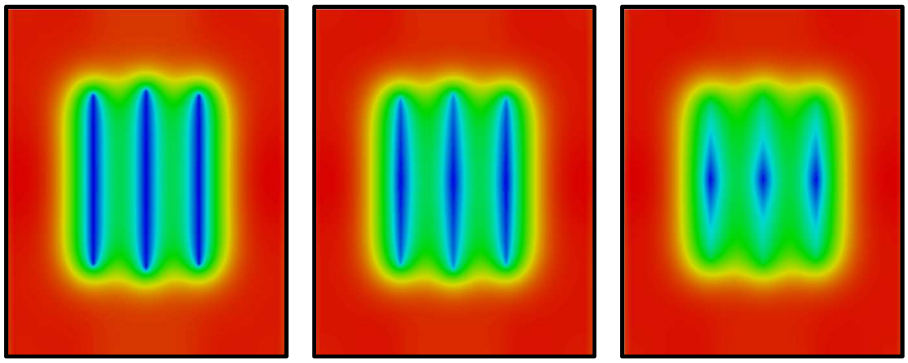

**(a) Strong proppant** **(b) Medium proppant** **(c) Weak proppant**

**Figure 2.13 Pressure depletion maps after 3 years production for different proppants**

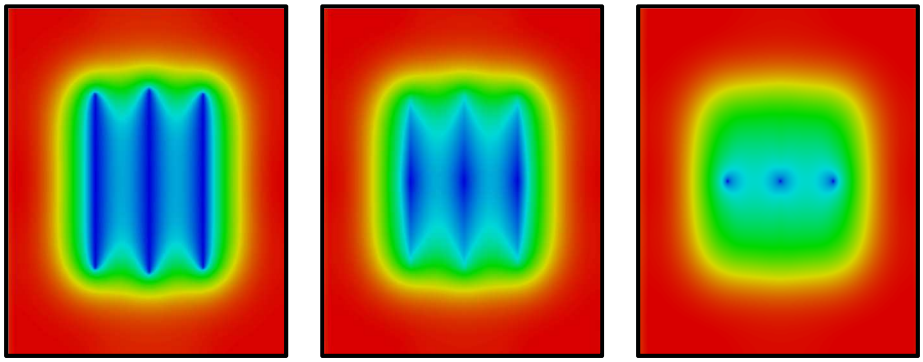

**(a) Strong proppant** **(b) Medium proppant** **(c) Weak proppant**

**Figure 2.14 Pressure depletion maps after 6 years production for different proppants**

Figure 2.15 shows the corresponding production rate comparison with different proppants. It shows that the production rate for weak proppants begins to deviate from others after the first year, indicating the conductivity becomes the bottleneck for the production. What is more, the production rate drops very fast and is almost negligible after

fifth year for weak proppants. Medium proppants deviate from the second year but production rate drops slowly. This is consistent with pressure depletion maps as shown in Figure 2.13 and Figure 2.14.

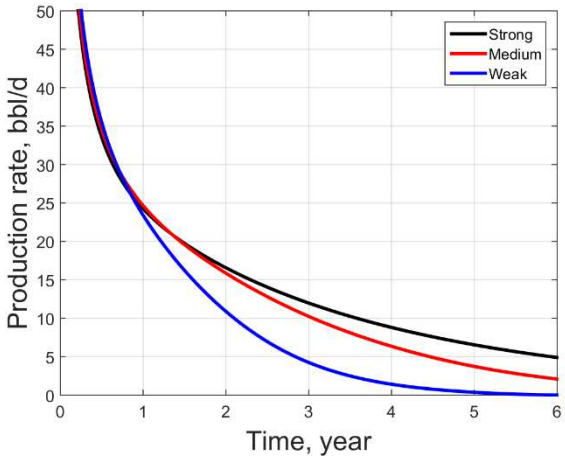


**Figure 2.15 Production rate comparison for the three-stage fracture system with different proppants**

### *2.3.6 Refracturing Strategy Comparison*

We assume that refracturing can be carried out from either the existing perforations that are already producing or the new perforations by using diversion techniques. The scenario without refracturing is referred to as “base case” for the comparative studies. As described earlier, by refracturing existing perforations, we can restore the fracture conductivity and further increase the fracture length; while by refracturing new perforations, we can create more fracture surface area in the undrained or less drained parts of the reservoir. The operational and economic feasibility for each option is beyond the scope of this study. The focus is on the well performance after refracturing in terms of cumulative production. The refracturing fluid volume is a variable that can be optimized based on the reservoir size,

well spacing and original fracturing job. Generally, the larger virgin reservoir is left, the more fracturing fluid is required for refracturing. Since the focus of this study is just on the refracturing performance in depleted reservoir, the same fracturing fluid volume is used for refracturing jobs. Another important assumption is that there is no limitation on the fracture length so that these fractures can further grow into the reservoir with the additional pumping. In other words, we assume fractures never reach the barrier or faults in horizontal direction. In following discussion, we first use the model with strong proppants, which is close to infinite conductivity situation, to investigate sensitivities of critical factors, and later use weak proppants to further investigate the sensitivity of fracture conductivity.

The reservoirs are produced for first 3 years and then sequentially refractured with the same schedule at existing perforations or new perforations. Figure 2.16 shows the comparison of fracture width and length for the two scenarios. By refracturing existing perforations with the same volume as initial fracturing, the averaged fracture length increases from 600 ft to 760 ft, while the maximum fracture width increases from 0.6 inch to 0.83 inch. As indicated in the previous section, due to the strong pressure depletion effect around the fracture, the fracture is under less confinement so that it becomes easier to enhance the fracture width within the depleted zone, rather than further elongate the fracture length into the new virgin zone. At the same time, the fracture width reduces slowly along fracture length, which can be observed directly from the figure where most section of fracture is in red color. On the other hand, by refracturing new perforations that are in the middle of existing ones, the additional fractures will be created. As a result of

stress shadow effect from existing fractures, the new generated fractures are a little narrower and longer, although pressure depletion can counteract the stress shadow to some extent in these new locations, depending on pressure and stress contrast. Overall, with the same refracturing fluid volume, the length and width increase in existing fractures is much smaller than surface area increase in new fractures.

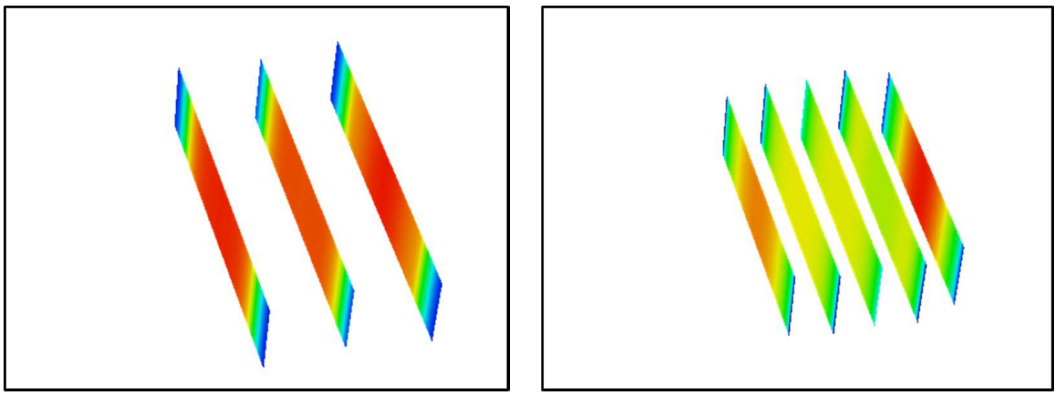

**(a)** **(b)**

**Figure 2.16 Fracture profile after 3 years production and refracturing in (a) existing perforations and (b) new perforations**

Figure 2.17 compares the production rate and cumulative production after 8 years production for cases without refracturing and with refracturing in different locations at the third year. The fracture spacing is 200 ft and matrix permeability is 100 nd. As observed in the plots, refracturing new perforation that induces the larger fracture surface area has the larger production rate at early time but declines much faster because of earlier interference between fractures, whereas refracturing existing perforation that induces the longer fracture shows the smaller production rate at early time but also slower decline. Eventually, refracturing existing perforations will outperform new perforations in terms

of cumulative production because of the larger stimulated reservoir volume (SRV) induced by longer fractures. This can be visually observed from the pressure distribution profile of three cases at the end of simulation, as shown in Figure 2.18.

It is worth noting that in this comparison we use strong proppants so that the degradation of fracture conductivity is negligible. That is why the percentage of overall production improvement by refracturing after a relatively long time is not that significant as expected, compared with base case without refracturing. In practice, this kind of wells, which have high fracture conductivity with strong proppant in relatively high permeability reservoir, may not be the potential candidate for refracturing. We use this case for the sensitivity studies of other critical designable parameters in following sections.

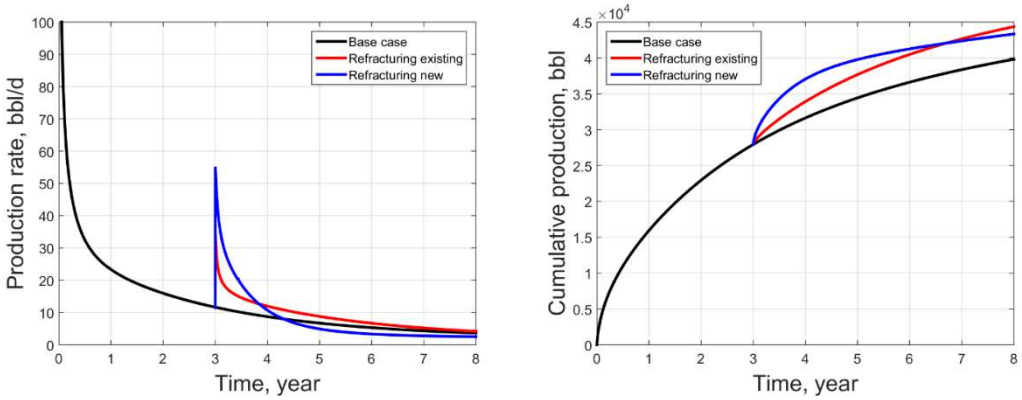


**Figure 2.17 Production rate and cumulative production by refracturing different locations**

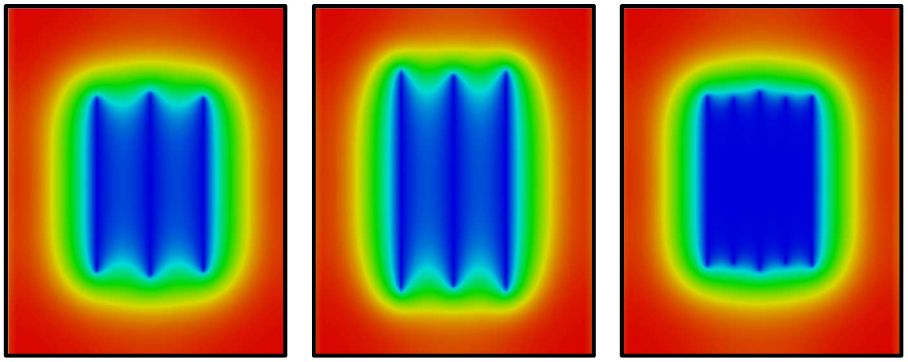

**(a) Base case** **(b) Refracturing existing** **(c) Refracturing new**

**Figure 2.18 Pressure depletion maps at end of simulation**

### *2.3.7 Sensitivity of Matrix Permeability*

In order to investigate different benefits of refracturing wells in different reservoir matrix permeability, we carried out sensitivity study by changing matrix permeability from 100 nd (base case) to both 50 nd and 200 nd. Figure 2.19 and Figure 2.20 compare the corresponding cumulative production after 8 years production for both base case and cases with refracturing at different locations after 3 years for 50 nd scenario, while Figure 2.21 and Figure 2.22 show the same results for 200 nd scenario.

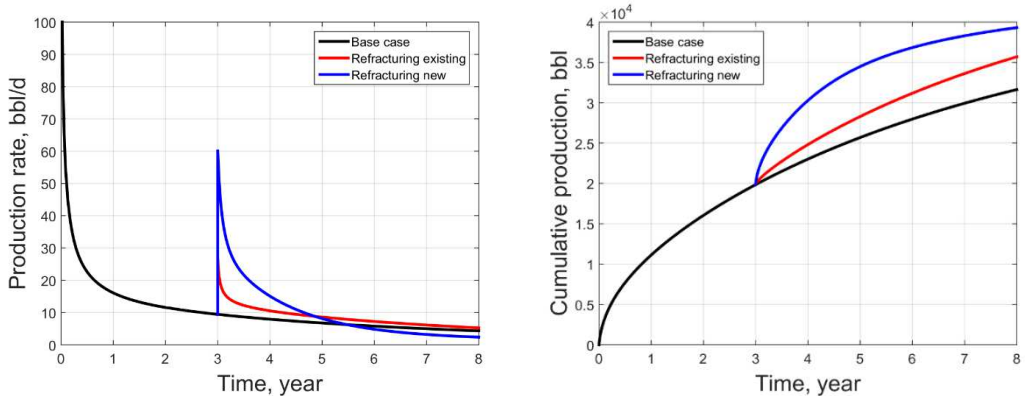


**Figure 2.19 Production rate and cumulative production comparison by refracturing different locations (permeability=50nd)**

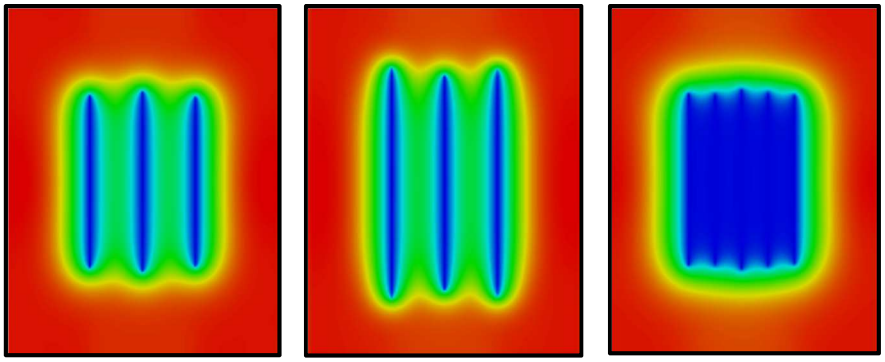

**(a) Base case** **(b) Refracturing existing** **(c) Refracturing new**

**Figure 2.20 Pressure depletion maps at end of simulation (permeability=50nd)**

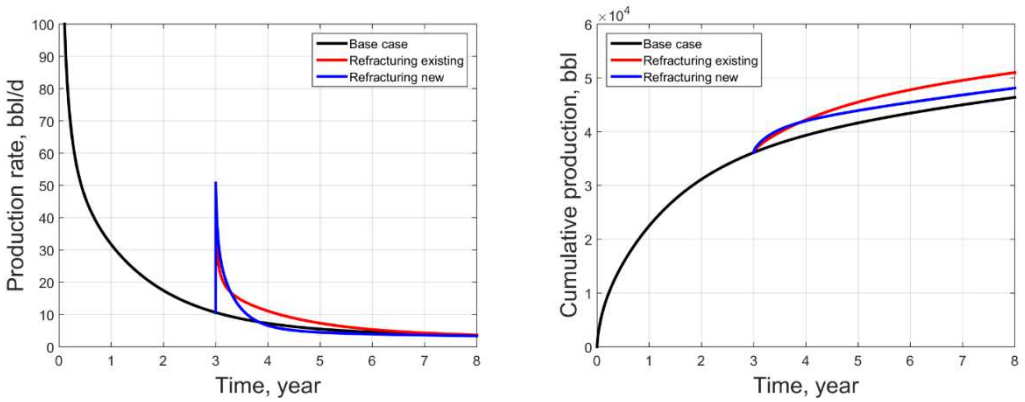


**Figure 2.21 Production rate and cumulative production comparison by refracturing different locations (permeability=200nd)**

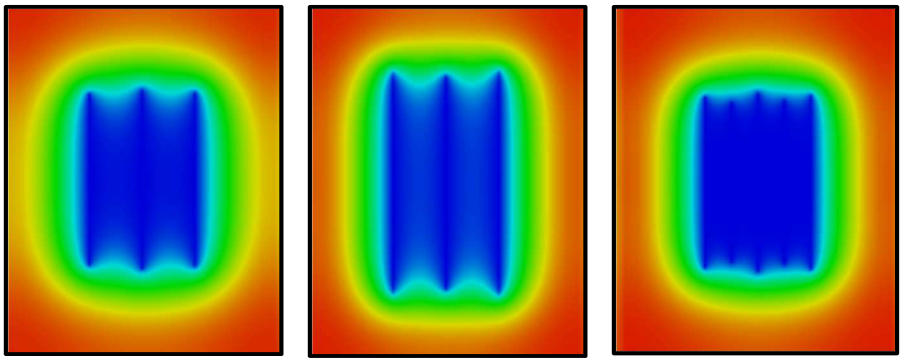

**(a) Base case** **(b) Refracturing existing** **(c) Refracturing new**

**Figure 2.22 Pressure depletion maps at end of simulation (permeability=200nd)**

From the production rate plots, we can see that the production rate curves from two different refracturing strategies cross each other. The main difference is the intersection time between two curves, which increases when the matrix permeability reduces. This means that refracturing new perforations outperforms the existing perforations for lower permeability reservoir because after the same production time lower permeability leaves more reservoir volume undrained near the new perforations. With larger permeability, the benefit of refracturing is reducing significantly as fractures might already have interference. By comparing the total production improvement we can see the huge potential for refracturing new perforations in low permeability reservoir.

### *2.3.8 Sensitivity of Stage Spacing*

To investigate the sensitivity of stage spacing, we change the stage spacing from 200 ft (base case) to both 100 ft and 400 ft. Figure 2.23 compares the fracture width and length evolution during the multi-stage sequential fracturing process. From the pictures we can observe that when stage spacing is reduced to 100 ft, the cumulative stress shadow is stronger and the maximum fracture width (from right to left) are 0.6 inch, 0.44 inch and 0.47 inch, while the corresponding full fracture length are 580 ft, 630 ft and 645 ft. On the contrary, for increased stage spacing at 400 ft, the stage interference is much smaller compared with the previous case as shown in Figure 2.11. The maximum width for these fractures (from right to left) are 0.6 inch, 0.52 inch and 0.57 inch, while the corresponding full fracture length are 580 ft, 600 ft and 585 ft. In this case, the third fracture has very similar geometry with the first fracture because stress shadow becomes small.

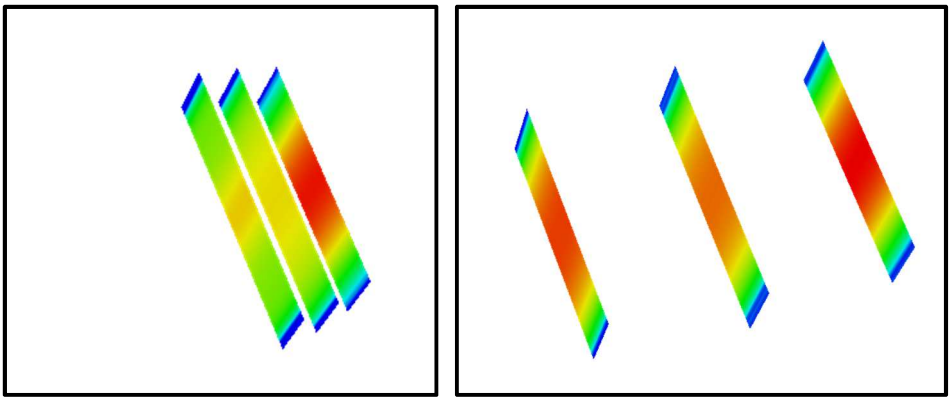

**(a) spacing = 100 ft** **(b) spacing = 400 ft**

**Figure 2.23 Fracture profile for multi-stage sequential hydraulic fracturing with different spacing**

Figure 2.24 shows the production rate and cumulative production for total 8 years production with different refracturing strategies for increased spacing 400 ft. The pressure depletion maps are shown in Figure 2.25. Similar as previous case with 200 ft spacing, the production improvement is not obvious for refracturing existing perforations because of original strong proppants used and limited fracture length increase. In contrast, refracturing new perforations results in significant production improvement about 60% more than the base case after 5 year since refracturing because of the large undrained reservoir left between the fractures.

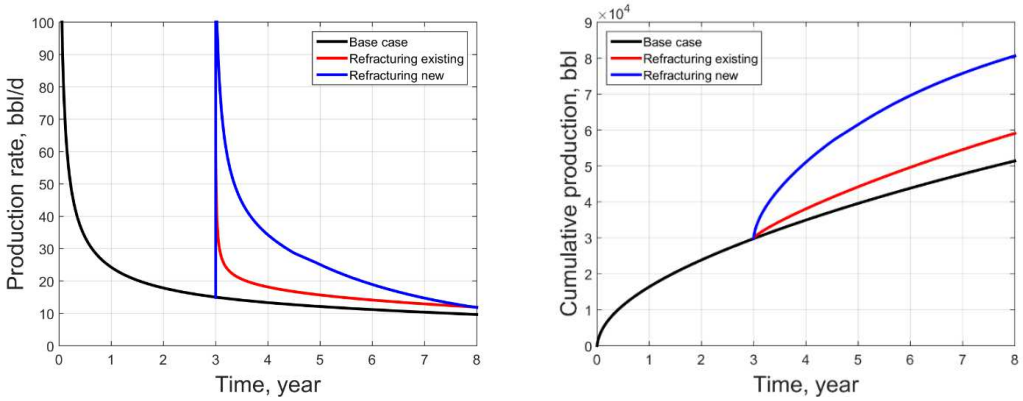


**Figure 2.24 Production rate and cumulative production comparison by refracturing different locations (spacing=400 ft)**

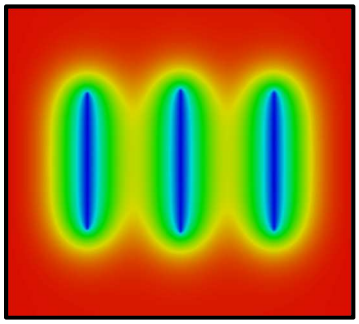

**(a) Base case**

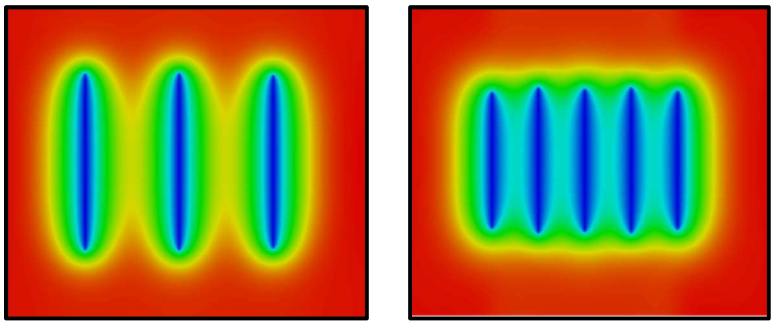

**(b) Refracturing existing** **(c) Refracturing new**

**Figure 2.25 Pressure depletion maps at end of simulation (spacing=400 ft)**

Figure 2.26 shows the production rate and cumulative production for total 3 years production for reduced spacing at 100 ft. As the fracture spacing becomes smaller, the fractures will interfere with each other earlier so that we start refracturing at 1.5 years and then look at the production after another 1.5 years. The simulation time and refracturing time here are not necessarily the same as 400ft spacing case since we are only comparing the relative performance of refracturing at existing perforations and new perforations. It is interesting that in this case, refracturing existing perforations performs better than refracturing new perforations, even in short term. The reason is that smaller spacing exerts stronger stress shadow effect on fractures. Therefore, refracturing existing perforation creates even longer fracture than that as shown in Figure 2.16 for the same fracturing volume, whereas refracturing new perforations makes the scenario complex since the stress shadow effect is so dominant at the location between the original close fractures. The first (rightmost) fracture has the largest fracture width, as a consequence, the new generated fracture next to it will be over-displaced with the same injection volume. As a result, the fracture width at perforation point is too small and thus choked as the bottleneck. Consequently, the refracturing at this location fails and the corresponding production contribution is negligible, as shown in Figure 2.27.

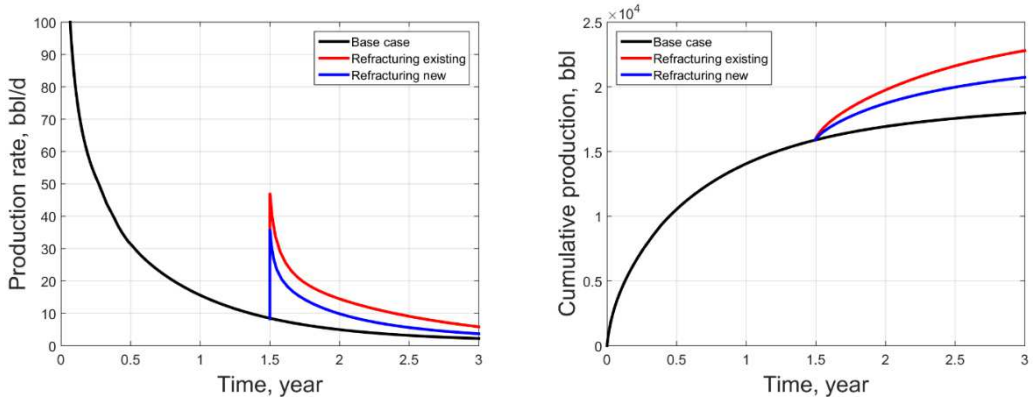


**Figure 2.26 Production rate and cumulative production comparison by refracturing different locations (spacing=100 ft)**

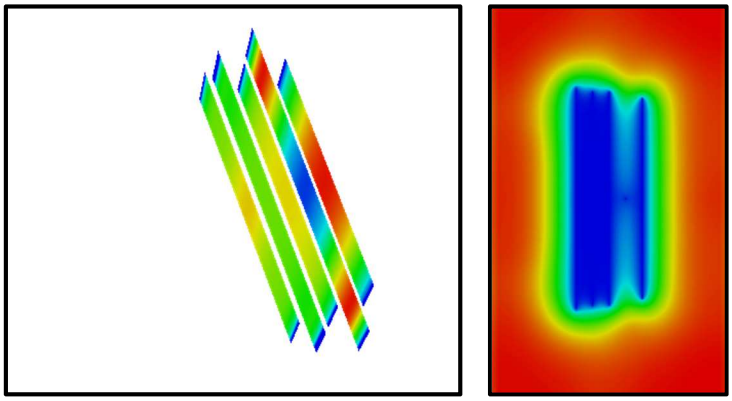

**Figure 2.27 Fracture profile after refracturing existing perforations and pressure map at the end of 3 years production**

### *2.3.9 Sensitivity of Refracturing Time*

Another important design parameter is the time for refracturing. In order to investigate the effect of refracturing time, we performed the sensitivity on both ‘strong’ and ‘weak’ proppants, because different degree of fracture conductivity degradation will induce different reservoir depletion and benefit of refracturing.

Figure 2.28 shows the cumulative production comparison when refracturing at different times for both refracturing strategies with strong proppants. As observed from the plots, at early time before fracture interference, refracturing new perforations can increase the cumulative production significantly up to twice. However, at late time, the production improvement becomes smaller because the regions between existing fractures have been depleted more. By contrast, the improvement by refracturing the existing perforations is not sensitive to the refracturing starting time since the increased production mainly comes from the region out of current SRV. But strictly speaking, refracturing earlier still gives slightly more cumulative production. Based on the simulation result with 'strong' proppant, if original fracture spacing permits (i.e., stress shadow effect is limited), refracturing new perforations is recommended as soon as possible. One extreme scenario suggests refracturing at the beginning is the best, which is corresponding to reduce the fracture cluster spacing as what currently industry is doing. This is just purely from the perspective of cumulative production, however, to which extent the spacing can be reduced must be constrained by the completion techniques and cost in practice.

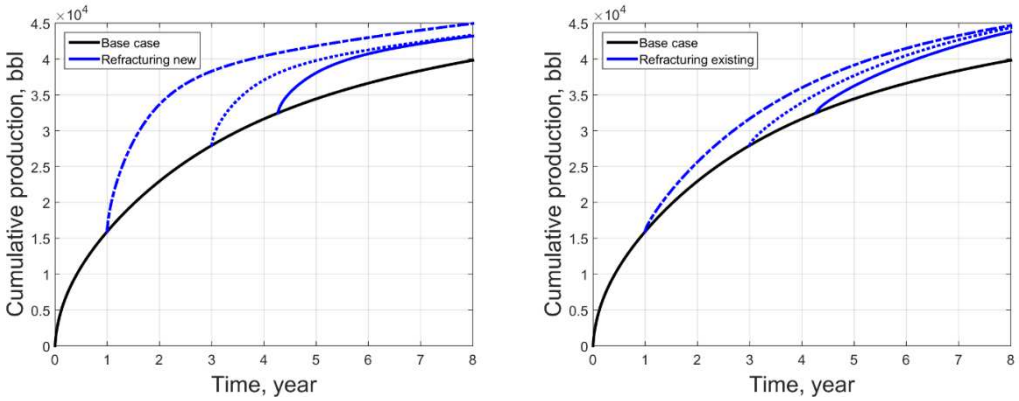


**Figure 2.28 Cumulative production comparison by refracturing at different time with strong proppants**

Figure 2.29 shows the cumulative production comparison when refracturing at different times for both refracturing strategies with weak proppants. For the curve of base case without refracturing, we can observe that the effective life time of these weak proppants only lasts about 3 year in terms of production improvement. Figure 2.30 shows the pressure depletion maps at these different refracturing times. For refracturing new perforations, the general trend is similar as that with strong proppants, as shown in Figure 2.28. As long as original fracture spacing permits and SRV region has not been fully depleted, refracturing new perforations is recommended as early as possible.

For refracturing existing perforations, the conclusion is different from the case with strong proppants because these is an optimal time to restore the existing fracture conductivity, which is about 3 year in our case. Too early refracturing will be at the waste of the previous treatment while late refracturing delays the production period. This is the most common situation in practice and the engineering practice is to perform refracturing whenever the production rate is below the economically acceptable limit.

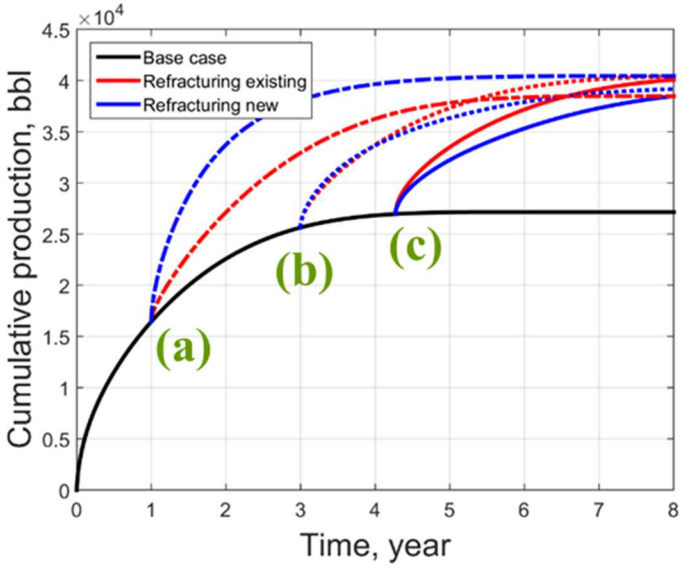


**Figure 2.29 Cumulative production comparison by refracturing at different time with weak proppants**

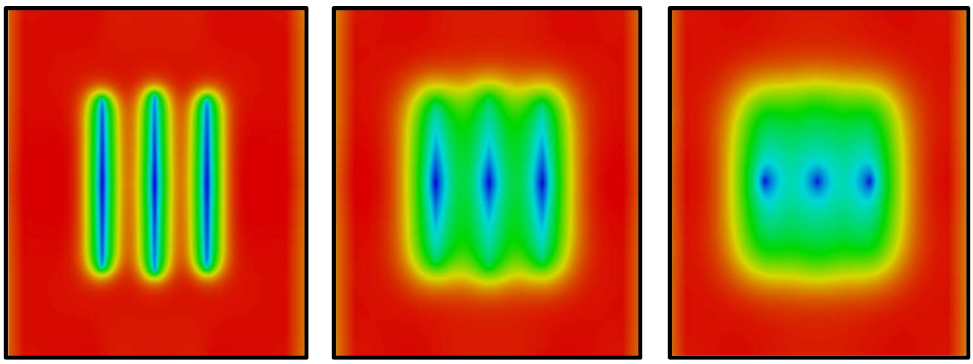

**(a) 1 year** **(b) 3 years** **(c) 4.3 years**

**Figure 2.30 Pressure depletion maps at different refracturing time**

## 2.4 Summary

In this chapter, we use a coupled fracture propagation and reservoir flow model to understand the critical factors that affect the performance of refracturing operation. By fully coupling geomechanics and flow, the depletion-induced stress is captured so that

subsequently generated fracture geometry strongly depends on the refracturing time and location. Based on fracture and reservoir conditions, different refracturing treatments will be favored. For example, refracturing existing perforations will restore the fracture conductivity while refracturing new perforations will stimulate new rock and create more surface contact area with the reservoir.

The results presented can provide insights into the evaluation of appropriate refracturing design. These key conclusion are summarized as follows:

1. Refracturing is likely to create wider but shorter fractures in the depleted parts of the reservoir compared to the un-depleted or virgin parts of the reservoir.
2. For very low permeability reservoirs, refracturing may be a good option, especially by refracturing new perforations to create more contact with the reservoir; but however, for relatively high permeability reservoirs, the benefit of refracturing new perforations may be limited if the SRV has been sufficiently depleted already.
3. Refracturing new perforations shows better short-term performance than refracturing existing perforations but worse long-term performance. The potential benefit of refracturing new perforations is reduced with later refracturing starting time and greater depletion in the current SRV.
4. When proppant degradation is severe, and fracture conductivity is the limiting factor for production, refracturing existing perforations becomes more attractive. Moreover, simulation results seem to indicate an optimum time window exists for refracturing in this scenario.

# CHAPTER III

# LIMITED ENTRY PERFORATIONS: IMPLICATIONS ON HYDRAULIC FRACTURE PROPAGATION AND WELL PERFORMANCE[*]

Production logs from horizontal wells in shale reservoirs indicate that more than 30% of the perforation clusters do not contribute to production. One major reason is recognized as the stress shadow effect which impedes the propagation of the interior fractures within a single fracture stage. Although limited entry perforations have been successfully introduced in horizontal wells to counteract this completion inefficiency, the complex mechanisms involved have not been fully understood.

In this chapter, a fully integrated workflow that incorporates fracture propagation, reservoir flow and wellbore hydraulics has been developed to evaluate the efficiency of limited entry perforations during multiple simultaneous fracture propagation. Darcy–Weisbach and classic orifice flow equations are adopted to describe the wellbore and perforation friction. The coupled reservoir and geomechanics model are solved by finite element code while a cohesive zone model, which accounts for the significant non-linear effects near fracture tip over the conventional linear elastic fracture mechanics, is used to simulate the fracturing process.

---

[*]Reprinted with permission from "Optimization of Hydraulic Fracture Development and Well Performance using Limited Entry Perforations" by Huang, J., et al. 2017: Paper SPE-185093-MS Presented at the SPE Oklahoma City Oil and Gas Symposium held in Oklahoma City, Oklahoma, USA, 27—30 March 2017. 

During the stimulation of multiple fractures, uneven fluid distribution will be observed once the fractures begin to interfere with each other. Meantime, the difference in perforation pressure loss due to uneven fluid rates will counteract the stress shadow effects and balance fluid distribution. Thus, a larger perforation friction coefficient is favorable but it also causes higher pumping pressure. A novel proppant model is proposed to represent both stress- and time-dependent fracture conductivity change due to proppant degradation in subsequent long-term production. Production simulation results demonstrate that deliberate deployment of limited entry technique can significantly increase production but this benefit is reduced with increased cluster spacing. Sensitivity study indicates that better well performance could be obtained by reducing number of shots in each cluster and increasing number of clusters in each stage. Non-uniform perforation shots distribution is proven to be an effective means to counteract the stress shadow effects while the cluster length is unchanged. Simulation results also indicate how the heterogeneity in reservoir properties affects the performance of limited entry perforations.

The proposed workflow has the advantage to integrate fracturing and production simulation in the same grid system and evaluate performance of different stimulation strategies. The comparison studies can provide critical insights to the application of engineered limited entry.

## 3.1 Introduction

Due to two modern technologies horizontal well and hydraulic fracturing, unconventional resources such as shale oil and gas have taken a major share in the energy supply in the

U.S. (Holditch 2010). Today's industry trend for unconventional reservoir development is gradually shifting towards to a much closer fracture spacing among multiple clusters in a single stage to maximize the production (Ingram et al. 2014). Therefore, the well-known 'stress shadowing' effect, which causes the interference on fracture propagation of each other (Lecampion et al. 2015; Peirce and Bunger 2015; Roussel and Sharma 2011; Wu and Olson 2015), becomes an unavoidable challenge for field operation. An amount of reported completion inefficiency and poor well performance have been believed to be associated with the stress shadowing effect. For example, the uneven distribution of injection fluid among clusters from a single stage is observed via downhole application of DTS and DAS (Molenaar et al. 2012); about 80% of production are observed to come from 20% of the clusters while about 30% of clusters do not contribute to the production (Miller et al. 2011); a peak stress value at the location above an active hydraulic fracture shortly after its start is measured (Jeffrey et al. 2013); in Montney field, the observed fluctuating ISIP and breakdown pressure from multistage hydraulic fracture treatment are recognized as an indicator of stress shadowing effect (Skomorowski et al. 2015). Meanwhile, conventional fracture models are mostly limited to consider the stress shadowing effect, a group of more sophisticated numerical models have been developed recently to simulate this effect among multiple simultaneous fracture propagation (Cheng et al. 2016; Shin and Sharma 2014; Wu and Olson 2015; Zhou et al. 2015).

Many completion techniques have been developed to promote an effective multi-fracture stimulation of horizontal wells but some of them are under high cost and risk that often make them unattractive. Limited entry technique is a fracturing practice of

promoting the development of perforation friction pressure during a reservoir stimulation treatment by limiting the number or size of perforation holes in a completion interval so that fracturing fluid can be diverted into the formation of interest through the selected perforations. The perforation holes work as chokes connecting wellbore and formation, where the flow resistance is related to perforation diameter and number (Bunger et al. 2014; Economides and Nolte 2000; Wu et al. 2016). This technique has been used successfully for decades in vertical wells.

Application of limited entry perforation is also extended to massive hydraulic fracturing of unconventional reservoir with ultra-low permeability and proved to be excellent stimulation approach for horizontal wells with an acceptable level of cost and risk recently (Oberhofer 2016; Ugueto C et al. 2016). Daneshy (2015) presented the theory of dynamic interaction within multiple fractures in horizontal wells which are in line with actual field trend. Lecampion et al. (2015) clarified the interplay between the impact of perforation friction and stress shadow on multiple fracture propagation and concluded that a sufficiently large pressure drop through perforation can inhibit the stress interference between different fractures. Wu et al. (2016) demonstrated that designing the limited entry perforations by intentionally tailoring perforation dimension in each cluster could promote uniform fracture propagation using the displacement discontinuity method. Besides limited entry technique, Peirce and Bunger (2015) suggested to use non-uniform fracture spacing to help mitigate the impact of stress shadowing effect. While these work focus on generated fracture geometry, the mechanism how limited entry perforations affect the well performance has not been fully studied.

On the other side, due to the existence of many natural weaknesses such as pores, vugs, grain boundaries, and pre-existing fractures, rock naturally displays strong heterogeneity (He et al. 2015; Yang et al. 2004). These heterogeneity can significant affect the interference between multiple fracture propagation (Ghassemi 2016; Zhou et al. 2016a).

In this chapter, we first use a fully coupled finite element poroelastic model to simulate multiple hydraulic fracture propagation in a single stage by coupling a wellbore model to account for wellbore and perforation friction. Our focus will be on the competition between multiple fracture initiation/propagation and perforation friction. Then, after well is shut in, we conduct the reservoir simulation based on generated fracture geometry to evaluate the relative performance along with a certain proppants degradation. The effect of reservoir heterogeneity within a stage on fracture initiation and propagation has been also investigated.

## 3.2 Methodology

A fully integrated workflow that incorporates fracture propagation, reservoir flow and wellbore hydraulics has been developed to evaluate the efficiency of limited entry perforation. To simulate multiple fracture simultaneous propagation in horizontal wells, a wellbore model connected to the formation through perforation holes must be incorporated to determine the fluid distribution into each clusters. This workflow notably accounts for the stress interaction between fractures and solves the fluid partition among clusters

iteratively in each time step. Material balance is maintained by that total injection volume into wellbore equals to hydraulically induced fracture volume and leakoff volume.

### *3.2.1 Coupled Fracture Propagation and Reservoir Model*

We use a fully coupled single phase flow and geomechanics model to describe the poroelastic effect in the reservoir, which are solved using conventional finite element methods. One advantage of the fully coupled model is that fracture propagation and subsequent production simulation can be performed on the same grid system (structured or unstructured) so that the induced stress and pressure change are retained for subsequent production simulation without requiring the upscale between different meshes.

To simulate hydraulic fracture propagation, conventional linear elastic fracture mechanics (LEFM) assumes pure elastic behavior of rock and predicts that a fracture will propagate as long as the stress intensity factor reaches the material toughness by ignoring the critical process zone, a small region near the fracture tip where the inelastic behavior occurs. This assumption applies to very brittle rock but fails when used to predict the fracture propagation in ductile and quasi-brittle rocks such as shales. Therefore, the cohesive zone model (CZM) is used to represent the fracture initiation and propagation, which considers the process zone near fracture tip and thus is able to capture the nonlinear material behavior near the fracture tip.

The cohesive zone model regards the fracture process as a gradual phenomenon in which separation of the fracture surfaces takes place along the predefined cohesive layer and is resisted by cohesive tractions. This cohesive traction reflects the intermolecular

strength and is much stronger than the macroscopic strength of material. Therefore, the traction-separation law, instead of simple linear elastic relationship, is used to describe the constitutive behavior of fractures in the formation. The fracture propagation is based on the energy criterion that states the fracture will start to propagate when the energy release rate reaches the critical fracture energy. More details of this model have been described in above chapter.

### *3.2.2 Proppant Model*

Proppant transport mechanism is critical for well performance since substantial field evidence have shown the strong correlations between the production of unconventional horizontal well and the amount of proppants pumped, even with slickwater treatment, such as being applied in the from Barnett shale (Coulter et al. 2004). For simplicity, this research will not explicitly simulate the proppant transport, instead, the portion of proppant between fractures in the same stage will be treated as the same with partition of injection fluid between fractures. Therefore, after well is shut in, the hydraulically opened fracture width will be used as a proxy for the propped fracture width for the following long-term production.

Different from the simulation in the literature that simply assume a constant fracture width or adopt a conductivity multiplier depending on closure stress, we explicitly simulate the mechanical interaction between fracture surface and proppants by introducing a proxy continuum model to represent the physical existence of proppants in the fracture. The major advantage of this method is that it provides a feasible and intuitive way to

incorporate both stress- and time-dependent fracture conductivity into long-term production simulation, which is missing in current unconventional reservoir simulation. The equivalent mechanical properties of proppant model requires calibration with experimental data.

### *3.2.3 Wellbore Model*

To facilitate the injection fluid distribution among fractures in the same stage, an effective model should be able to consider following characteristics: 1) fluid friction along the wellbore in long intervals; 2) fluid friction through the perforations; 3) hydrostatic pressure change along the lateral; 4) potential perforation erosion by proppant-laden slurry.

Figure 3.1 shows the coupled wellbore model connecting to multiple fractures through the perforation holes. The surface treating pressure is given by (Lord et al. 1994)

$$P_{surface} = P_{fracture} + \Delta P_{perf} + \Delta P_{wellbore} - \Delta P_{hydrostatic} \tag{3.1}$$

where $P_{surface}$ is surface treating pressure; $P_{fracture}$ is the fluid pressure in the fracture; $\Delta P_{perf}$ is friction through perforations; $\Delta P_{wellbore}$ is the pressure along wellbore; $\Delta P_{hydrostatic}$ is the hydrostatic pressure change. Since our simulation domain focus only on a single fracture stage in the horizontal section of wellbore, the hydrostatic pressure change is zero in our case.

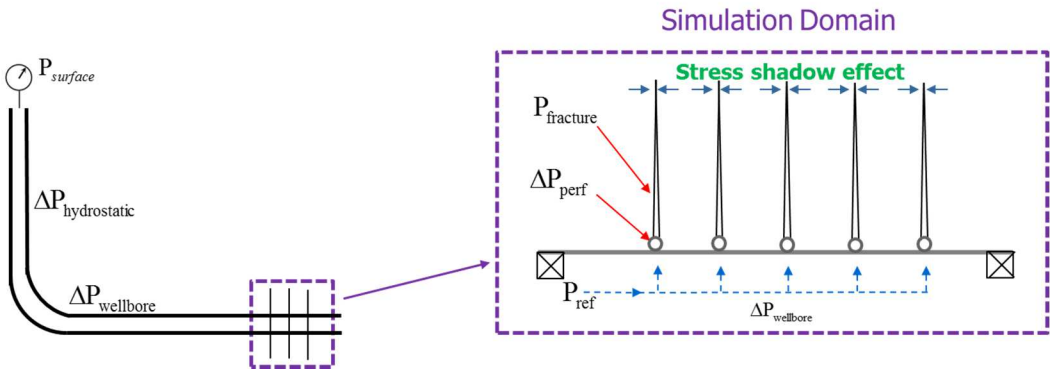


**Figure 3.1 Coupled wellbore and reservoir model for multiple fracture propagation**

Accurate simulation of fluid distribution relies on the calculation of perforation and wellbore friction. The classical orifice flow equation is typically adopted in petroleum industry to estimate the perforation friction drop (Cramer 1987; Economides and Nolte 2000)

$$\Delta P_{perf} = \frac{0.2369\rho}{D^4 C_d^2}\left(\frac{Q}{n}\right)^2 \tag{3.2}$$

where $\rho$ is density of fracturing fluid; $D$ is the perforation diameter; $C_d$ is dimensionless discharge coefficient; $Q$ is the total volumetric injection rate; $n$ is the number of perforations. Although perforation erosion only has a minor effect on fluid distribution in vertical wells, it can significantly affect the fluid distribution in horizontal well stimulation when following conditions are satisfied: 1) formation is connected to the wellbore through a limited number of perforations; 2) stress varies considerably at each perforation cluster; 3) large volume of proppants are injected under high injection rates (Cramer 1987; Harris and Pippin 2000). When proppants pass through the perforation and start to erode it, the value of diameter $D$ and discharge coefficient $C_d$ will increase

correspondingly. Cramer (1987) defined a new parameter named hydraulic perforation diameter that lumps $D$ and $C_d$ together. This new empirical parameter can be fitted as a simple linear function (Romero et al. 1995) and adopted to consider the potential perforation erosion when it is non-trivial.

For simplicity, we also assume an incompressible fluid in steady state along the wellbore so that Darcy–Weisbach equation can be used to describe the friction loss along wellbore

$$\Delta P_{wb} = f_D \cdot \frac{L}{D} \cdot \frac{\rho v^2}{2} \tag{3.3}$$

where $f_D$ is the Darcy friction factor depending on the flow regime; $L$ is wellbore interval; $v$ is the velocity of fluid flow in wellbore. Within a single stage (about hundreds of feet), the wellbore friction loss is much smaller than the perforation friction at regular pumping rate.

## 3.3 Results and Discussion

### *3.3.1 Stress Shadow Dominated Fracture Propagation*

In this section, we first look at the phenomenon of non-uniform fracture propagation in simultaneous fracturing due to the stress shadow via a series of synthetic examples. The base case we use here is a single stage with five perforation clusters where we assume only one possible dominant fracture in each cluster of perforation holes, therefore, the potential fracture spacing is the initially designed perforation cluster spacing. In the base case, reservoir is assumed to be homogeneous with uniform cluster spacing, as well as

completion designs like perforation number and diameter. The key parameters used in this modeling is listed in Table 2.1 which resembles a well completion practice in a shale reservoir. The base case is built in the way that the perforation friction is negligible compared with the induced stress shadow effect so that we can get insights about the situation without limited entry technique.

Figure 3.2 displays the simulated fracture geometry of the base case at the end of injection. From this plot, we can see the two outer fractures dominate the propagation while both the length and width of inside fractures are suppressed, leaving majority of inside volume unstimulated. This is expected because there is no constraint on their growth in the vicinity. Along the fracture length direction, fracture width decreases slightly in the majority of its length but significantly when close to fracture tip, indicating the segment near wellbore has larger flow path capability and dominant contribution to the production. In addition, within this single stage, wellbore pressure loss is so trivial that the fractures on left and right are almost symmetric. Therefore, in following plots we only show the symmetric half fractures.

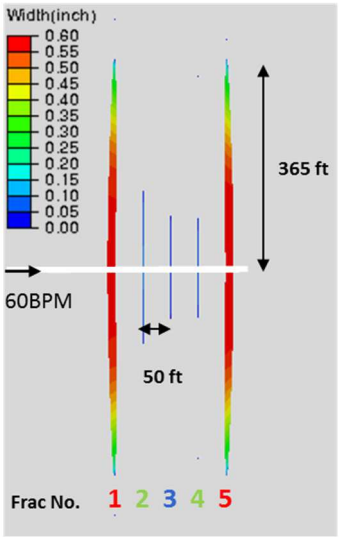


**Figure 3.2 Fracture propagation in a single fracture stage with five perforation clusters (base case)**

Figure 3.3 (a) and (b) show the dynamic evolution of fracture width at the wellbore and cumulative volume taken by each fracture during the injection. From both plots, we can observe that there is no significant difference in first two minutes when all fractures are relatively short compared with their spacing and have not yet started to interfere each other. But after that, fluid begins to distribute unevenly into each fracture due to the superposed stress shadow on the inner fractures which makes it harder to expand or extend than outer fractures. As a result, fluid tends to flow into the fractures under the least compressive stress. This uneven distribution deteriorates with time. Figure 3.3 (a) and (b) also indicate that while the inner fractures are still taking some fluid after late time, fracture width of these inner fractures is decreasing, rendering the high risk of proppant screen-out in field operation.

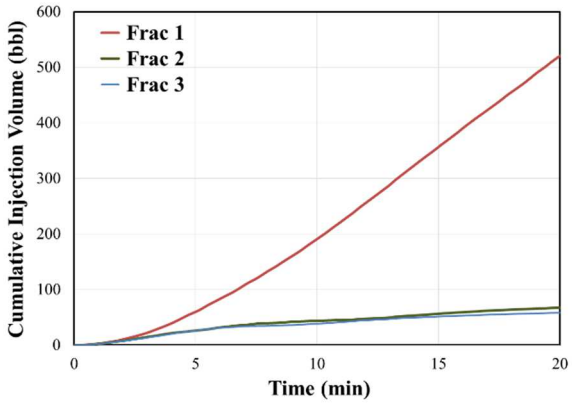


**(a)**

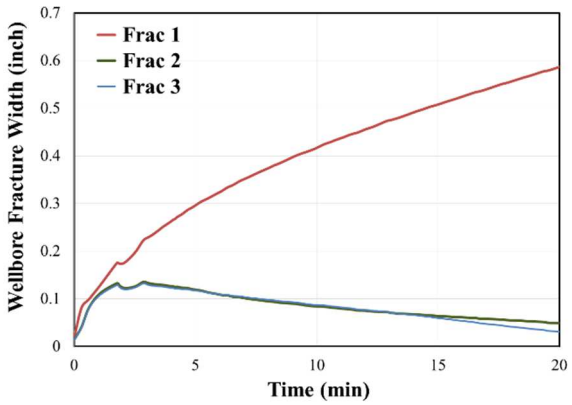


**(b)**

**Figure 3.3 (a) Cumulative injection volume distribution into each fracture; (b) Individual fracture width (at wellbore) evolution during fracturing. Numbering of fracture is marked in Figure 3.1.**

### *3.3.2 Limited Entry Perforations*

In above section, only two outer fractures propagate and dominate the whole fracture stage when perforation friction is trivial. In the section, we introduce the limited entry perforations to increase the pressure friction loss through the perforations and balance the fluid distribution among the clusters. The additional friction is gained by altering the number of shots in each cluster, as well as the diameter of perforation holes from our base

case. The description of these cases is listed in Table 3.1. Eq. (3.1) indicates that the perforation friction loss increases with the second power of number of shots and fourth power of perforation diameter.

| Cases | No. of clusters | No. of shots | Perf. diameter (inch) | Pumping rate (BPM) |
|---|---|---|---|---|
| Base case | 5 | 12 | 0.84 | 60 |
| Case 1 | 5 | 6 | 0.42 | 60 |
| Case 2 | 5 | 3 | 0.42 | 60 |

**Table 3.1 Description of comparison cases**

Figure 3.4 shows the fracture geometry at the end of pumping for the modified Cases 1 and 2, demonstrating the effect of limited entry perforation. Compared with base case, the second (and fourth) fractures in these cases are longer and wider. At the same time, the width of outer fractures have been reduced significantly. Overall, the fracture pattern is observed to be more uniform by reducing both number and diameter of perforation shots. The apparent explanation is that the increased friction will promote the uniform distribution of pumping fluid into each other. However, a hidden mechanism which can provide additional benefit on reducing stress shadowing on inner fractures is generally ignored. This is recently pointed out by Peirce and Bunger (2015). They demonstrated that when two fractures with comparable length are very close to each other (e.g., Fractures 1 and 2), the mutual interference has the effect of inhibiting the runaway growth of one dominant fracture that was previously observed in our base case. This

enhanced competition also reduces their constraint on the most inner fracture (Fracture 3), which results in a better growth in case 2.

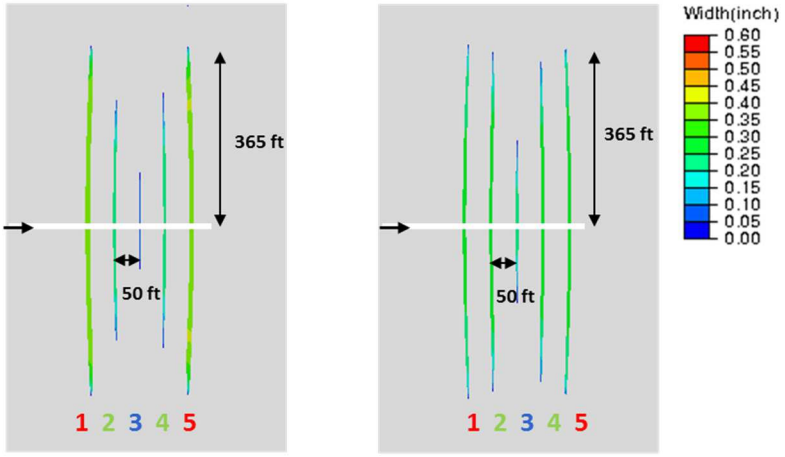


**(a) Case 1** **(b) Case 2**

**Figure 3.4 Fracture length and width distribution in a single fracture stage**

Figure 3.5 and Figure 3.6 show the cumulative injection volume distribution and fracture width changes versus time of each individual fracture of Case 1 and 2, illustrating the mechanism behind the observed fracture configuration. It is obvious that more fluid is going into the inner fractures. From the cumulative volume plot, we can see stress shadow induced fluid suppression on Fracture 2 is significantly delayed thus cumulative fluid into Fracture 2 is increasing compared with base case. In addition, different from Figure 3.3, the width of Fracture 2 in Figure 3.5 (b) is increasing monotonically within the 20 minutes, indicating stress shadow of outer fracture is not strong enough to fully suppress growth of nearby fractures as it did in the base case. With even larger friction loss, width of all fractures could be increasing during the 20 minutes, as indicated in Figure 3.6 (b). From

these plots, it is evident that limited entry perforation can effectively promote more uniform fracture propagation.

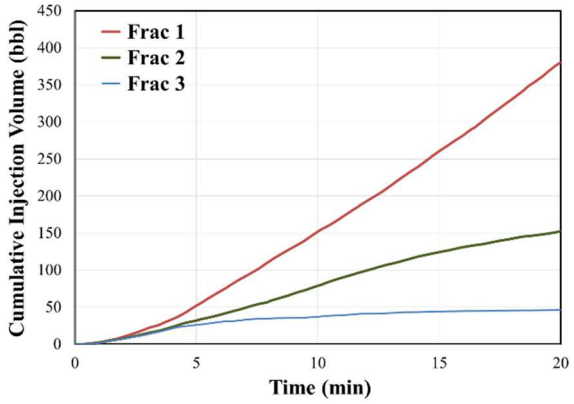


**(a)**

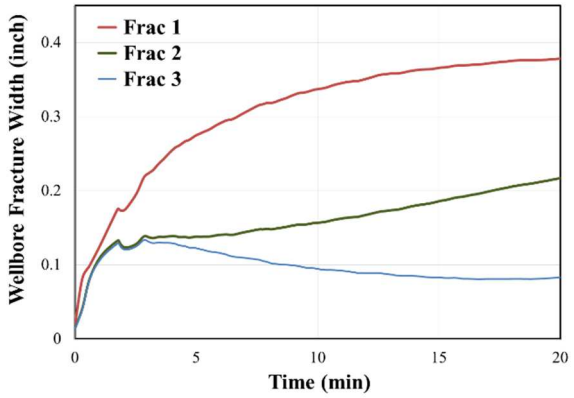


**(b)**

**Figure 3.5 (a) Cumulative injection volume distribution and (b) Fracture width of Case 1**

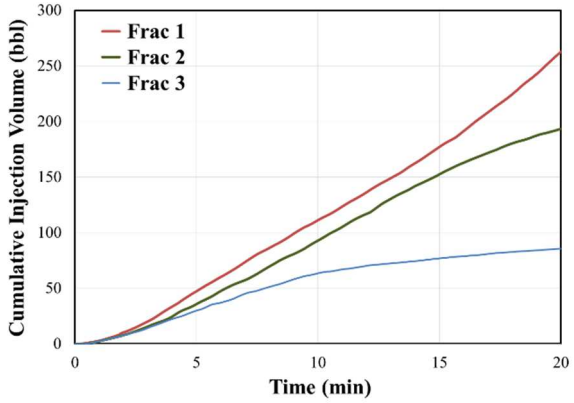


**(a)**

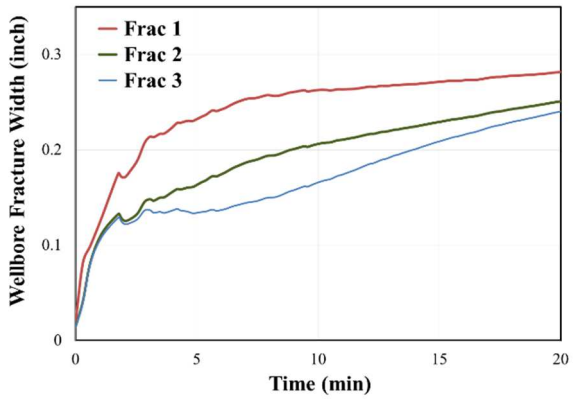


**(b)**

**Figure 3.6 (a) Cumulative injection volume distribution and (b) Fracture width of Case 2**

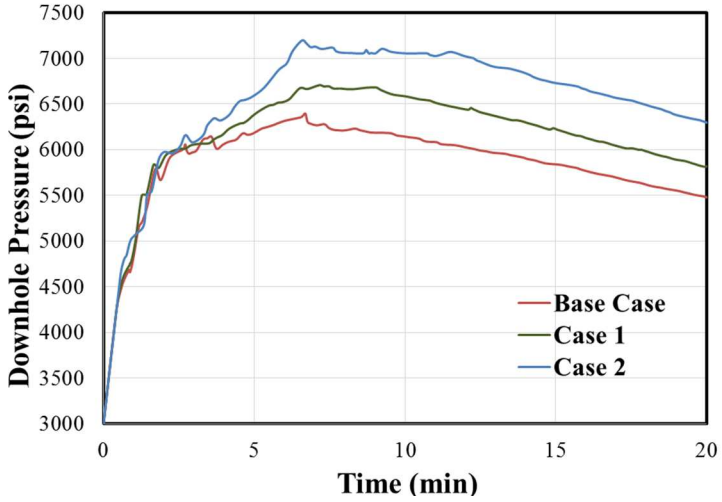


**Figure 3.7 Downhole pressure response for different limited entry cases**

Figure 3.7 shows the downhole pressure for each case with the injection rate linearly ramping up in early time and staying constant afterwards. Although these cases display a significant discrepancy in fracture geometry, their pressure curves have similar trend. This indicates that it is hard to infer the fracture geometry by analyzing the pressure record alone, as suggested by Lecampion et al. (2015).

In the preceding section, our focus is to promote the uniform fracture propagation from a completion point of view. Now we investigate the potential benefit of well production after applying limited entry perforations. More specifically, we take a close look at how each individual fracture contributes to the performance of the whole fracture stage. Figure 3.8 clearly show the individual fracture contribution to the cumulative production, as well as the pressure depletion map after 3 years. In the base case, the two outer fractures together contribute to 88% of the total production of this fracture stage, leaving the vast majority of the interior volume undepleted. In Case 1, this percentage drops to 50% but the magnitude just decreases slightly from 2950 bbl to 2810 bbl of Fracture 1, indicating that production interference is negligible and increased production mainly comes from the interior volume of this stage. When fractures become more uniform in Case 2, although fracture interference further reduces the production of Fracture 1, the enhancement from Fractures 2 and 3 is more pronounced. Overall, increasing perforation friction can boost the total production by promoting uniform production contribution among the fracture cluster, thus a deliberate deployment of limited entry technique is desired in practice.

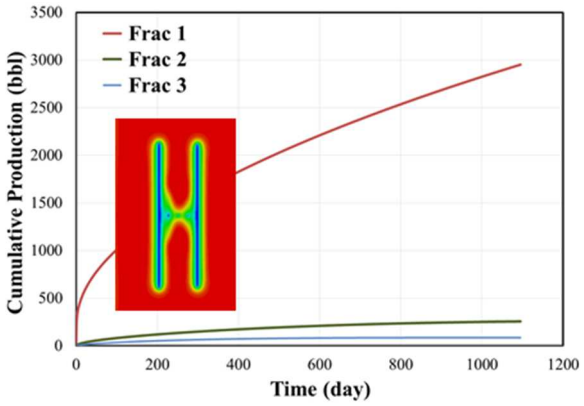


**(a) Base case**

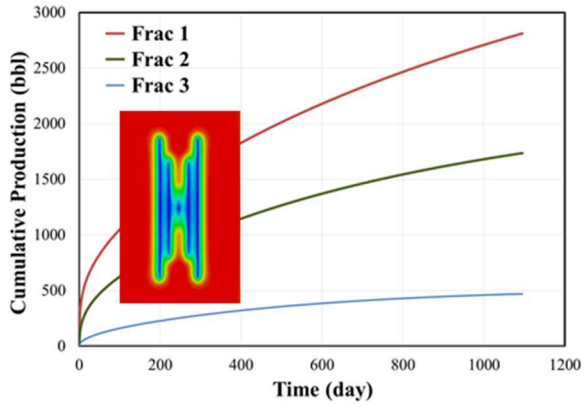


**(b) Case 1**

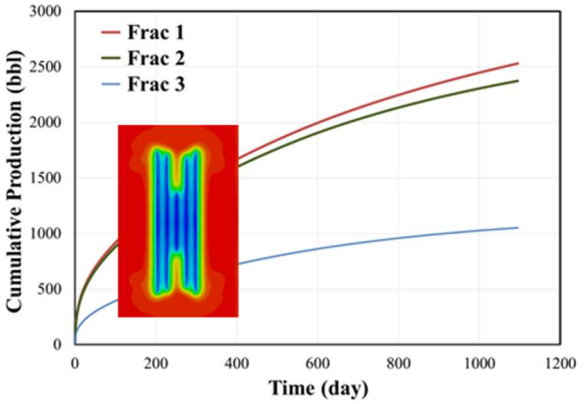


**(c) Case 2**

**Figure 3.8 Cumulative production of individual fractures**

### *3.3.3 Sensitivity of Cluster Spacing*

As discussed in the preceding section, the stress shadow is dominant when fractures are too close to each other, resulting in the nonuniform fluid distribution among clusters. Limited entry perforation could balance it by increasing the perforation friction loss to different magnitudes, depending on the rate. Therefore, it is necessary to understand the relationship between limited entry contribution and the cluster spacing. The above studies use a constant cluster spacing at 50 ft, now we investigate the sensitivity by changing it to 100 ft. Figure 3.9 displays the pressure depletion map after 3 year production for all cases with 100 ft. Compared with 50 ft, the fracture growth is much more uniform as expected because the stress shadow effect decays rapidly with fracture spacing.

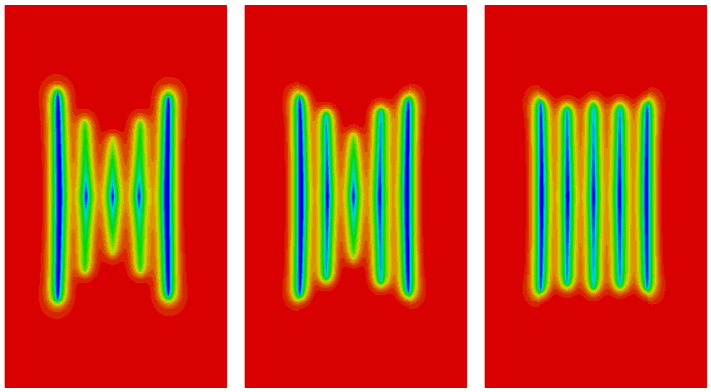

**(a)** **(b)** **(c)**

**Figure 3.9 Pressure map after 3 year for 100 ft cluster spacing: (a) Base case; (b) Case 1; (c) Case 2**

To make a fair comparison on well production from 50 and 100 ft cases, we normalize the production rate by well lateral length as shown in Figure 3.10. The improvement of production rate is considerable by employing limited entry perforations at 50 ft spacing, especially at early time when fracture production interference is

negligible. However, this rate boost is not significant at 100 ft spacing. In other words, the benefit from limited entry has been significantly reduced when spacing increases to 100 ft as a result of reduced stress shadow. This result provides an insight that we may not need to consider this technique when fracture spacing itself is large enough to avoid the impact from stress shadow effect. In additional, under the same treatment (same pumping volume), the normalized production rate in 50 ft spacing is better than that of 100 ft spacing, which agrees with industry experience.

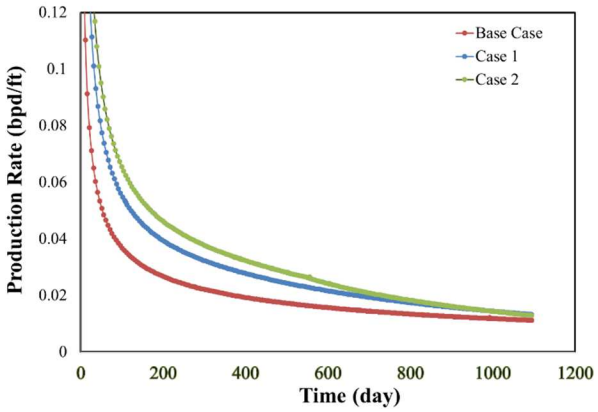


**(a) spacing = 50 ft**

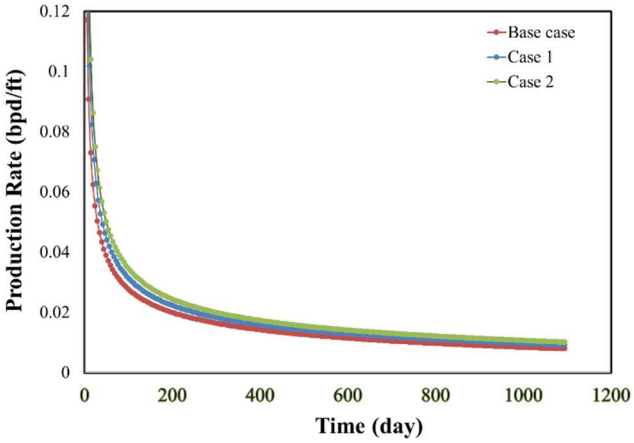


**(b) spacing = 100ft**

**Figure 3.10 Normalized Production rate (per lateral length) for different fracture spacing**

### *3.3.4 Sensitivity of Number of Clusters*

As we demonstrated in previous section, the additional friction can be achieved by reducing either the number of shots in each cluster or the diameter of perforation holes. In practice, the perforation hole, as the pathway of proppant-laden slurry, cannot be too small. Otherwise, there is risk for proppant screen out. A more common strategy is to reduce the number of perforations but increase the number of clusters within each stage at the same time so that the total number of perforation holes in each stage will not change too much. To this end, we consider another scenarios which maintain the same cluster spacing but extend the stage by adding two more clusters. As a consequence, the length of the stage is increased and less number of stages is required for the same horizontal lateral. To maintain the same loading of fluids and proppants, here we also consider increasing the pumping rate from 60 BPM to 84 BPM while pumping time is the same. Table 3.2 describes the details in the two additional comparison cases compared with Table 3.1. The cluster spacing is still 50 ft, same as Cases 1 and 2.

| **Cases** | **No. of clusters** | **No. of shots** | **Perf. diameter (inch)** | **Pumping rate (BPM)** |
|---|---|---|---|---|
| Case 3 | 7 | 3 | 0.42 | 60 |
| Case 4 | 7 | 3 | 0.42 | 84 |

**Table 3.2 Description of cases with extended number of clusters**

Figure 3.11 displays the pressure distribution after 3 year productions for above 4 comparison cases. From this map, we can see that by extending the stage spacing, Cases

3 and 4 have accessed a larger SRV than Cases 1 and 3. However, with the same pumping fluid in each stage, the average taken by each fracture in Case 3 is smaller than that in Case 2, resulting in a shorter fracture. When the pumping rate is increased to maintain same fluid and proppants density along the lateral in Case 4, the perforation friction loss is increased and fluid distribution is more uniform. Meanwhile, a pair of interferring fractures form on each side, which can benefit the inside fractures. Figure 3.12 shows the comparison of 3-year cumulative production normalized by Case 1. The increase from Case 1 to Case 2 has been explained in above section. Stage production from Case 3 is higher than Case 2 because it uses the same shots per cluster but two additional clusters. However, the production per cluster decreases because the pumping rate is not increased. To make a fair comparison, the total pumping rate is increased so that rate per cluster is the same in Case 4, where we see the increase not only in stage production but also in averaged cluster though it is not significant. This numerical experiment indicates that a more efficient and cost-effective strategy with fewer stages can be achieved by increasing number of clusters while reducing number of shots in each cluster.

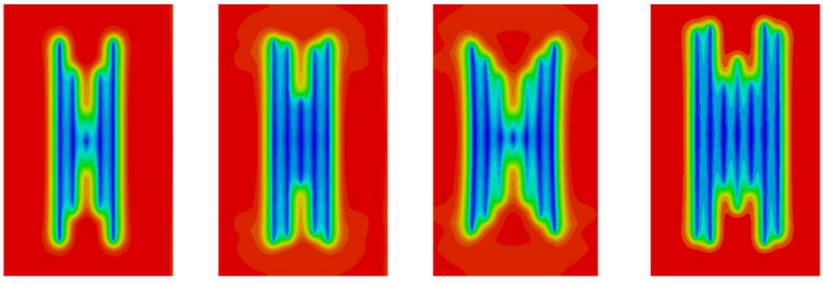

**(a) Case 1** **(b) Case 2** **(c) Case 3** **(d) Case 4**

**Figure 3.11 Pressure map after 3 year for 50 ft cluster spacing**

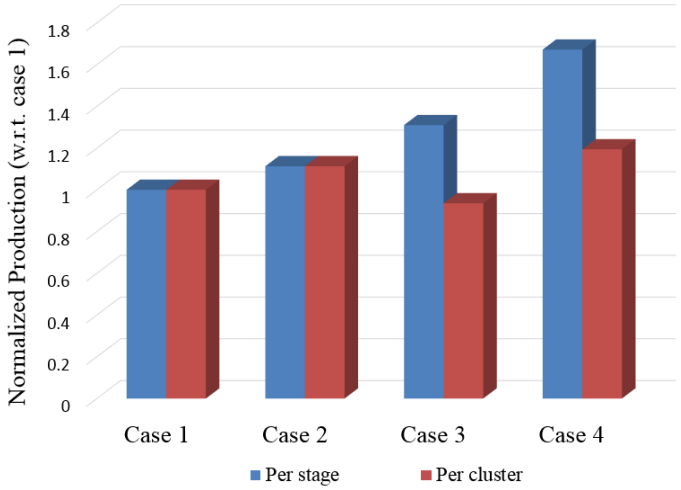


**Figure 3.12 3-year normalized cumulative production comparison**

### *3.3.5 Sensitivity of Nonuniform Perforations*

Through preceding sections, we understand that the growth of middle fractures within a single stage is suppressed by stress shadowing effect and reducing number of shots can mitigate it by significantly increasing friction loss at the outer clusters which takes most fluid. Now we investigate a more efficient way by adopting nonuniform perforation distribution. The objective is to divert more pumping fluid into the middle fractures, so we can either increase the number of shots in middle fractures or reduce it in outer fractures. Specifically, we create additional four cases by adjusting the number of perforation shots in Case 1: Case 5 and 6 increase the shots in middle fractures where Case 7 and 8 reduces the shots in outer fractures. The layout of shots are listed in Table 3.3.

| Cases | Perforation shot layout in a five-cluster stage |
|---|---|
| Case 1 | (6, 6, 6, 6, 6) |
| Case 5 | (6, 6, **12**, 6, 6) |
| Case 6 | (6, **9**, **12**, **9**, 6) |
| Case 7 | (**4**, 6, 6, 6, **4**) |
| Case 8 | (**2**, 6, 6, 6, **2**) |

**Table 3.3 Nonuniform perforation shot distribution in comparison cases**

Figure 3.13 shows the fracture geometry comparison by adjusting the number of perforation shots, as well as the volume percentage of both injection and production associated with each fracture. The bar charts show that the more injection fluid taken by a fracture, the more production it will contribute. Figure 3.14 shows the percentage of the 3-year cumulative production improvement from Case 1. Since the most middle fracture is under the largest stress shadow, its number of shots is changed to 12 to reduce friction in Case 5, which results in a longer middle fracture at the expense of suppressed neighboring fractures. Case 6 further increases the neighboring fracture from 6 shots to 9 shots, giving a more uniform geometry than Case 5, but the production from Figure 3.12 indicates that the marginal benefit by increasing the perforation shots in middle fractures is very limited because the pressure drop was already very small there compared with that in outer fractures. Thus, instead of increasing shots in middle fracture, reducing shots in the outer fracture could be more cost-effective because it creates enough friction loss to balance the resistance suffered by middle fractures due to stress shadowing. However, a very delicate calculation is required to determine the number of shots: a number which is too small can result in overbalanced fluid distribution where the fractures next to outer

fracture get a chance to propagate dominantly, as shown in Case 8. As a result, while Case 7 has the highest production, consistent to its most uniform fracture distribution in Figure 3.13, Case 8 uses only two perforation shots in outer fractures and shows the worst result, which could even harm the production.

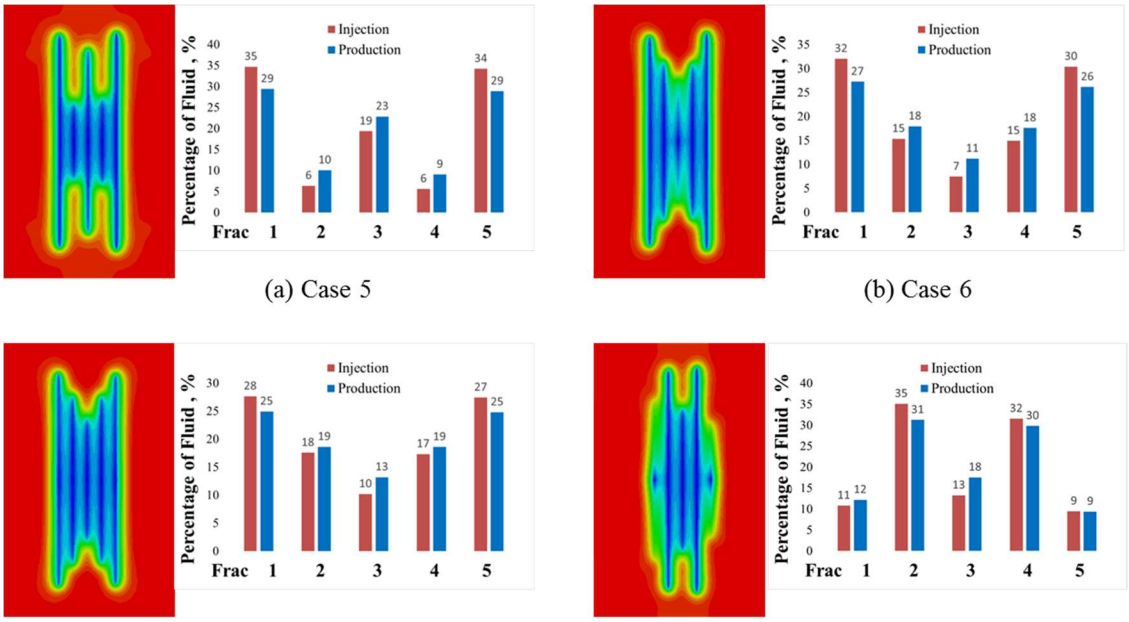


**Figure 3.13 Pressure map after 3 years and volume percentage of injection and production of each fracture for Case 5--8**

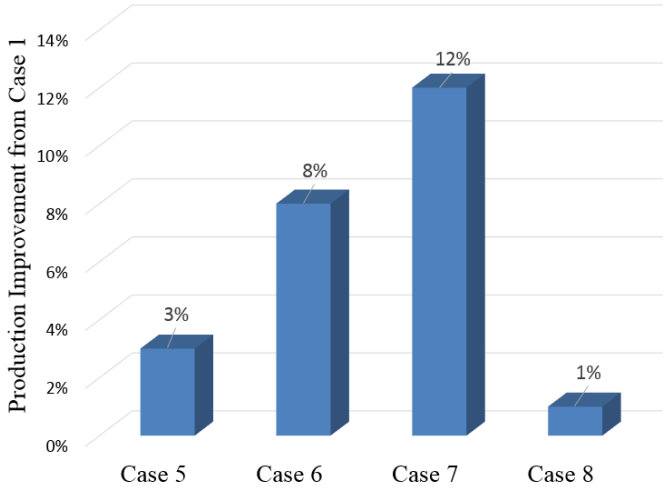


**Figure 3.14 Percentage of 3-year cumulative production improvement from Case 1**

### *3.3.6 Sensitivity of Mechanical Heterogeneity*

The conventional fracture design tools often ignore the vertical and horizontal heterogeneity of unconventional reservoirs. The well log data indicates the fractures sometimes are expected to penetrate a series of highly variable sandstone and shale formations along the vertical direction. Geologic heterogeneity along horizontal wellbore can also cause a wide variability of rock properties. These heterogeneities exist over a wide range of scales, from microns to hundreds of kilometers, which could directly affect the fracturing performance at different stages, or even fractures within the same stage. Consequently, the geometric placement of stages may result in completion inefficiency and poor well performance.

In this section, we investigate the effect of heterogeneity of mechanical properties on fracture propagation and limited entry performance. Based on the Case 1, we introduce the layered heterogeneity at some layers. The heterogeneity is introduced by reducing the

Young's modulus, Poisson's Ratio and fracture toughness to 60% of original properties, marked by the red color in Figure 3.15. The heterogeneous layers are less resistant to the fracture growth due to the weaker properties. Figure 3.15 shows the fracture geometry comparison in homogeneous and the layered heterogeneous formation, where fractures are less uniform in heterogeneous case. The reason is that two outside dominant fractures propagate faster and thus reach the weaker layer earlier. Once they reach there, the fracture resistance significantly decreases so that more fluid will go into these fractures. Since the weaker layers have smaller Poisson' Ratio and thus smaller horizontal stress, the fracture width is much larger at these layered that can hold more fluid. As a result, once fracture growth meets a lesser resistance at the layer interface, fluid would be more likely diverted into these fractures. Overall, we can see from the picture that the maximum fracture length is reduced from 365 ft to 320 ft. At the same time, the fracture width is also no longer monotonically decreasing from wellbore to fracture tip. For the middle fracture, these narrow widths near wellbore could be a bottleneck that deteriorate the productivity of these fractures.

Figure 3.16 shows the downhole pressure comparison. Unlike the monotonous decrease of pressure in homogeneous case, the pressure curve displays four dips corresponding to the weaker layers. The closer to wellbore, the more significant impact the weaker layer has. This plot demonstrates that pressure response can give some insights to the reservoir heterogeneity.

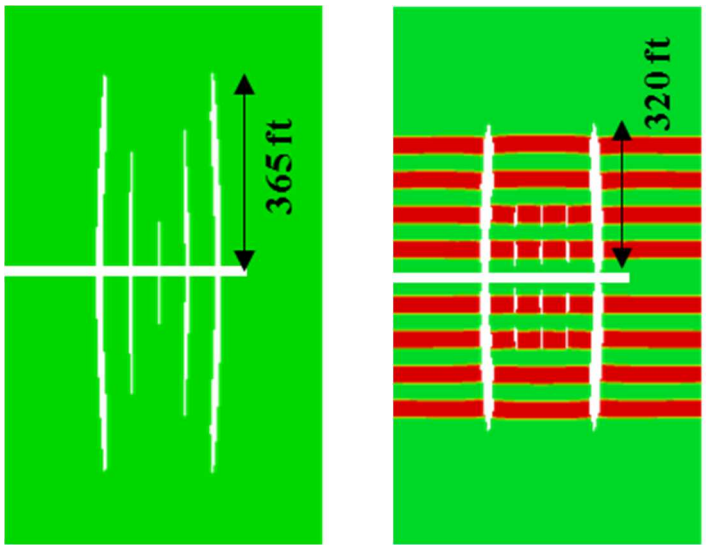


**(a)** **(b)**

**Figure 3.15 Fracture geometry in (a) homogeneous and (b) layered heterogeneous formation. Green color represents original properties while red color represents the weaker layer with 60% of original mechanical properties. Fracture width is magnified by a factor of 400.**

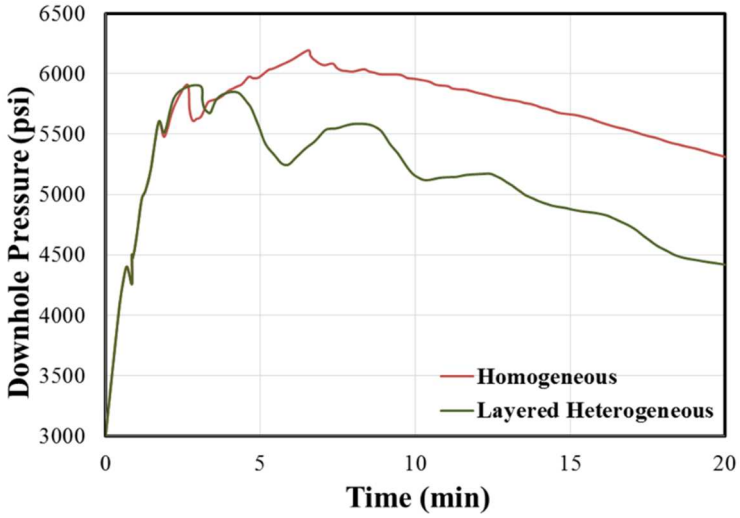


**Figure 3.16 Downhole pressure response for homogeneous and heterogeneous cases**

## 3.4 Summary

In this chapter, an integrated workflow that incorporates fracture propagation, reservoir flow and wellbore hydraulics has been adopted to evaluate the efficiency of limited entry perforation during multiple simultaneous fracture propagation. The nonuniform fracture growth can be mitigated by deliberate deployment of number of perforation shots and clusters within a single stage. The numerical results presented provide insights into the optimization of hydraulic fracturing design and well performance. These key conclusions are summarized as follows:

1. Stress shadow effect on multiple fractures propagating simultaneously in a single stage will cause uneven fluid volume and resulting non-uniform fracture development.
2. Perforation frictions are demonstrated to be effective to counteract the additional flow resistance exerted by stress shadowing.
3. Limited entry perforations could potentially promote more uniform fracture development and thus improve the well performance by altering the perforation layout in a stage.
4. Formation heterogeneity may benefit or harm the effect of limited entry perforations. Therefore, a more accurate engineered limited entry strategy is required to mitigate the flow imbalance.

# CHAPTER IV

# MULTIWELL PERFORMANCE PREDICTION AND WELL SPACING OPTIMIZATION USING THE FAST MARCHING METHOD

One of the challenges in the development planning of unconventional reservoirs is determining the optimal well spacing. It is essential to understand when and how the well performance has been impacted by surrounding wells. Modeling of well interference in unconventional reservoirs is complicated by the complexity and uncertainties in fracture geometry. In this chapter, we propose a novel and efficient approach based on fast marching method to identify well interference and quantify the relationship between well spacing and well performance in unconventional reservoirs. The proposed method can directly track the onset of well interference and thus the reservoir can be partitioned accordingly based on the competing drainage volumes amongst the wells. The drainage volume evolution within each subdomain associated with any particular well can be used to recast the 3-D diffusivity equation to a 1-D form which can be solved analytically or numerically for pressure and rate response. As a result, it not only allows us to rigorously compute the well drainage volume as a function of time but also to assess the potential impact of in-fill wells on the performance of existing wells. With these improvement, we then present a new workflow to optimize well spacing in unconventional reservoirs.

The novelty and advantage of our method are that it provides an intuitive way to characterize potential well interference and fracture connectivity in the reservoir, as well

as a rapid prescreening method for well spacing optimization with tremendous computational efficiency compared to traditional finite-difference simulation.

## 4.1 Introduction

To tap more hydrocarbons resources, today's industrial trend moves to the strategies that utilize more closely spaced hydraulic fractures, along with multiple horizontal wells with reduced spacing, to maximize the production from ultra-low permeability reservoir. For example, a very common practice is to use the drilling pad, which concentrates wellheads at the surface to reduce the footprint and increase efficiency. As a result, the horizontal wells/laterals that share the same wellhead could be very close to each other. Another practice is to drill infill wells (typically called child well) close to a producing well (typically called parent well), which could significantly decrease the average well spacing. The immediate challenge from above practices is to find the best well spacing design which minimizes the interference and maximizes the production.

Developing an efficient reservoir management strategy typically requires reasonable estimation of both drainage capacity of existing wells and impact of potential infill well to minimize the overlapping of drainage volumes. Analytical methods have been used for decades to quickly estimate the drainage volume. For example, production decline curve analysis has been proved to be an effective tool for computing drainage volumes and estimating economic ultimate recovery (EUR) (Blasingame and Rushing 2005; Cox et al. 1996; Fetkovich 1980; Rushing et al. 2008). In addition, pressure transient tests are also used to calculate the well productivity and potential improvement by

hydraulic fractures (Lee and Hopkins 1994). Although both decline curve and pressure transient analyses have played a critical role in the exploitation of hydrocarbon resources, such analytical tools cannot provide an intuitive way to visualize the drainage volume evolution of each individual well, the onset of well interference and the subsequent competition between them. Moreover, these existing analytic methods are initially proposed for conventional reservoirs, which makes it even worse to apply to the unconventional reservoir with the ultra-low permeability and strong heterogeneity due to existence of natural fractures.

To intuitively visualize the drainage volume evolution, numerical method like streamline has been used to help visualize the trajectories or flow paths, which are always tangential to the local flow velocity. As a representation of the instantaneous velocity field, streamlines form whenever underlying velocity field exists, no matter of the flow conditions such as compressible or incompressible flow, steady or unsteady flow, oil or gas reservoirs (Datta-Gupta and King 2007). Although the visualization power of streamlines have been proved to be very powerful to examine both swept and drainage volumes in conventional reservoirs, it requires the information of flux field that is generally calculated by full finite difference/volume simulation and cumbersome in high resolution reservoirs.

Another challenge during the application of the streamlines in unconventional reservoir comes from the diffusive nature of the governing equation. There are some efforts to extend the application. Kulkarni et al. (2001) extended the streamline-based time of flight approach to transient flow conditions by introducing a new concept of ‘diffusive

time of flight' (DTOF) and rigorously computed the radius of well drainage in heterogeneous reservoirs. He et al. (2002) demonstrated the good agreement between streamline-based drainage volume calculations with conventional decline type curve results. Kang et al. (2013) presented an effective approach to optimize well placement by using streamline method in unconventional reservoir for both synthetic and field applications.

In light of the complexity and limitation of streamline method in unconventional reservoirs, a novel formulation of the diffusivity equation has been developed to quickly model the pressure response and define the drainage volume for unconventional reservoirs (Datta-Gupta et al. 2011). The proposed drainage volume characterization utilizes the concept of drainage volume that relies on the definition of the radius of investigation by John Lee (1982), defined as the propagation distance of a "peak" pressure disturbance for an impulse source or sink. This formulation is derived from the asymptotic (high frequency) limit of the diffusivity equation for the impulse pressure solution and leads to the Eikonal equation, which generalizes the depth of investigation for heterogeneous and complex reservoirs, as well as provides an efficient way to calculate drainage volume, pressure depletion and well performance by introducing the concept of diffusive time of flight (DTOF). This kind of equation can be efficiently solved by the fast marching method (FMM).

The similar concept has also been used by other researchers. For example, Meyer et al. (2010) utilized the concept of radius of investigation (John Lee 1982) to examine fracture interference in the presence of multiple hydraulic fractures in horizontal wells and

predict behavior of multiple transverse hydraulic fractures in a horizontal well and optimization methodology to hydraulic fracture stages. However, much of these previous work have been limited to homogeneous medium. In contrast, the solution from fast marching method can be applied not only heterogeneous reservoir but also complex unstructured grid system (Zhang et al. 2013). However, the underlying assumption of asymptotic solution requires the pressure wave to propagate in the infinite domain, which cannot always be satisfied in unconventional reservoirs, especially considering the close spacing between neighbor fractures or wells. Just similar to optic rays and electromagnetic waves, the pressure wave is also reflected and transmitted on the interface between different media (Oliver 1994). Therefore, taking into account above mechanisms could compensate the solution discrepancy induced by the boundary effect.

The goal in this chapter is to develop a systematic procedure for a rapid multi-well performance prediction and infill well spacing optimization in unconventional reservoirs. The objectives of this work are threefold: first, we propose an extended FMM to incorporate the additional boundary reflection pressure wave front to improve the pressure solution of original FMM which only applies to the transient flow regime; second, we propose a novel partition method based on the principle of superposition and analytical asymptotic approximation to quantity the drainage volume interference between multiple wells; finally, we apply the above improvements into both homogeneous and heterogeneous reservoirs to identify the potential interference between existing and infill wells, as well as use the new partition as a basis for a rapid well performance prediction and well spacing optimization.

## 4.2 Methodology

### *4.2.1 Depth of Investigation and Drainage Volume*

Towards the objectives of this work, we first need to clearly define the concept of well drainage volume in multiple well scenarios. So far, there is no well-established method to define the well drainage volume in unconventional reservoirs. A common practice in the industry is to utilize the pressure/saturation contours to track evolution of well drainage behavior with time. This approach is very intuitive and straightforward but needs to set an arbitrarily defined pressure contour level for tracking.

In contrast, we adopt the concept of radius of investigation from John Lee (2003), defined as the propagation distance of 'peak' pressure disturbance resulting from an impulse source. For 2D radial flow in homogeneous reservoir, the radius of investigation can be derived in field units (John Lee 2003)

$$r = \sqrt{\frac{kt}{948\phi\mu c_t}} \tag{4.1}$$

For different flow patterns, the analytical solution of radius of investigation can be generally written as follows

$$r = \sqrt{\beta\alpha t} \tag{4.2}$$

where $r$ and $t$ are propagation distance and time of the pressure front and $\alpha$ is the hydraulic diffusivity defined as

$$\alpha = \frac{k}{\phi\mu c_t} \tag{4.3}$$

where $\beta$ is a geometric factor related to the flow regime. For instance, for linear, radial, and spherical flow, $\beta$ is 2, 4, and 6 respectively (Kim et al. 2009).

According to above definition, the concept of drainage volume is the 'footprint' of the pressure wave in the reservoir, confined by above radius of investigation. Since this concept is an indicator of the propagation distance of 'peak' pressure disturbance, the pressure drop actually also occurs beyond this pressure front. Therefore, as the cutoff for drainage volume, this radius of investigation is not necessarily the boundary of no flow condition in the infinite-acting reservoir. In a reservoir drained by multiple wells, once the pressure front of different well meets each other, flow competition happens between them, resulting in a no flow boundary that divides the reservoir volume between wells. Ultimately, the volume drained by any given well is proportional to that well's production rate

$$DV_i = DV_t \frac{q_i}{q_t} \tag{4.4}$$

where $DV_i$ is the drainage volume of Well $i$, $DV_t$ is the entire drainage volume of the reservoir, $q_i$ is the production rate from Well $i$, and $q_t$ is the total production rate from the reservoir.

### *4.2.2 Boundary Effect in Asymptotic Solution*

Like optics, the pressure wave can be reflected and transmitted at the boundary interface between different media. This happens when we apply the asymptotic solution to the reservoir with finite size or characterize the interference between multiple close wells.

Previous simulations based on asymptotic solution only consider the first arrival of pressure front and thus have difficulty to deal with these scenarios. As a result, in these situations, the calculated pressure solution may give misleading results when subsequent reflected pressure front is of significant amplitude, making it an additional valuable resource for pressure drop.

To eliminate the aforementioned drawback, an extended FMM for tracking multiple wave fronts has been proposed here. A vast variety of techniques are currently available for modeling the propagation of high frequency pressure waves in heterogeneous media but they are only capable of capturing first arrivals without modification. Therefore, the main difference of our proposed method is to track the arrival time at all boundaries and restart the reflected pressure front from that boundary at the recorded values, opposing to that traditional fast marching method is a single-pass sweeping method. By considering reflected pressure front, multiple values of arrival time will be obtained in the same computational domain. Each individual pressure wave will induce the pressure change when it arrives, therefore taking into account these later arrivals could improve the pressure results.

Traditionally, the analytical solution of pressure drop can be obtained by using image well and superposition theorem, based on Green's function and source functions. Here we apply the same methodology to extend current fast marching based simulation. An image well is not a real well but used mathematically to achieve the same boundary effect from a flow barrier. The boundaries may be either no flow boundaries or fixed pressure boundaries. The disadvantage of image well method is that in some situations it

is inadequate. For example, particular complications are encountered when handling boundary arrangements which comprise one or more pairs of parallel boundaries. Such arrangements theoretically require an image well system extending to infinity. In practice, it is impossible to implement a virtual system that extends into infinity and thus, a limited number of pressure front has been typically accounted. Experience shows that one or two additional reflected fronts is accurate enough for most smoothly varying media. Furthermore, the principle of superposition indicates that the total pressure at any point in a reservoir is the sum of the pressure drops at that point caused by flow in each of the wells in the reservoir. To get the improved pressure solution, superposition is then applied to the pressure drops caused by each pressure front. This procedure will be illustrated in the following application section.

### *4.2.3 Proof of Extended FMM in Bounded Reservoir*

As mentioned in above section, the proposed extended FMM will introduce an additional $\tau$ coordinate to improve the pressure solution in a bounded system. Following is to prove that it works with an arbitrary no flow boundary. Recall the diffusivity equation:

$$\phi c_t \frac{\partial p}{\partial t} + \nabla \cdot \vec{u} = 0 \quad where \quad \vec{u} = -\frac{1}{\mu} \vec{\vec{k}} \cdot \nabla p \tag{4.5}$$

With a second reflection $\tau$ coordinate, asymptotic approximation for a fixed rate draw-down can be written as

$$c_t \frac{\partial p}{\partial t} = -\frac{q_w}{V_p(t)} \left\{ e^{-(\tau_1 - \tau_w)^2 / 4t} + e^{-\tau_2^2 / 4t} \right\} \tag{4.6}$$

Here $\tau_1$ is the usual outwardly moving $\tau$ coordinate and $\tau_2$ is the new inwardly moving coordinate, calculated by the extended FMM. For convenience, let's assume that $\tau_w$ is small (no negative skin) and simplify the equations, $\tau_w << \tau_1$. If necessary, a finite wellbore correction can always be re-introduced.

For drainage volume, we can integrate the solution over the finite domain (no flow outer boundaries) to obtain the equation for $V_p(t)$

$$\begin{aligned} q_w &= \iiint_{Domain} d^3x \nabla \cdot \vec{u} = \frac{q_w}{V_p(t)} \iiint_{Domain} d^3x \phi \left\{ e^{-\tau_1^2/4t} + e^{-\tau_2^2/4t} \right\} \\ V_p(t) &= \iiint_{Domain} d^3x \phi \left\{ e^{-\tau_1^2/4t} + e^{-\tau_2^2/4t} \right\} \end{aligned} \tag{4.7}$$

For a fixed rate drawdown, the drainage volume can be defined in terms of the derivative of the pressure drop at the wellbore

$$c_t \frac{d\Delta p_{wf}}{dt} = \frac{q_w}{V_d(t)} \tag{4.8}$$

The drainage volume is defined as

$$\begin{aligned} \frac{1}{V_d(t)} &= \frac{1}{V_p(t)} \left\{ 1 + e^{-\tau_{20}^2/4t} \right\} \\ V_d(t) &= V_p(t) \Big/ \left\{ 1 + e^{-\tau_{20}^2/4t} \right\} \end{aligned} \tag{4.9}$$

where $\tau_{20}$ is the second arrival of pressure front at wellbore.

At the boundary, the normal component of the velocity must be continuous. We may express the continuity requirements in terms of flux, but it is simpler for us to work with the continuity of its time derivative.

$$\left[\frac{\partial \vec{u}}{\partial t} = 0\right] \quad where\,[\ ] = discontinuity \tag{4.10}$$

where

$$\frac{\partial \vec{u}}{\partial t} = -\frac{1}{\mu}\vec{\vec{k}} \cdot \nabla \frac{\partial p}{\partial t} \tag{4.11}$$

Plugging Eq. (4.6) into above equation,

$$\begin{aligned} \frac{\partial \vec{u}}{\partial t} &= \frac{q_w}{\mu c_t V(t)}\vec{\vec{k}} \cdot \nabla\left\{e^{-\tau_1^2/4t} + e^{-\tau_2^2/4t}\right\} \\ &= -\frac{q_w}{\mu c_t 2tV(t)}\vec{\vec{k}} \cdot \left\{\tau_1 \nabla \tau_1 e^{-\tau_1^2/4t} + \tau_2 \nabla \tau_2 e^{-\tau_2^2/4t}\right\} \end{aligned} \tag{4.12}$$

On the boundary, $\tau_1 = \tau_2$, but for no flow boundary $\vec{n} \cdot \frac{\partial \vec{u}}{\partial t} = 0$, it requires

$$\vec{n} \cdot \vec{\vec{k}} \cdot \nabla(\tau_1 + \tau_2) = 0 \tag{4.13}$$

As shown in the Figure 4.1, for the cell at the boundary, both the outwardly moving $\tau$ value at cell center and the value at boundary will be calculated in the first FMM run. Within each individual boundary cell, from its cell center or boundary (face) center, the shortest path is the straight line between them, thus multidimensional Eikonal equation is reduced to 1-D equation, as shown in the Figure 4.1.

$$\tau_1^c + \Delta\tau = \tau_1^e \tag{4.14}$$

The above boundary value will be calculated and recorded to start the calculation of inwardly moving $\tau$ coordinate.

$$\tau_1^e = \tau_2^e \tag{4.15}$$

Similarly, from boundary to its closest cell center value it is along the same path:

$$\tau_2^e + \Delta\tau = \tau_2^c \tag{4.16}$$

Substituting Eqs.(4.14)--(4.16) into Eq. (4.13) gives

$$\vec{n} \cdot \vec{\vec{k}} \cdot \nabla\left(\tau_1 + \tau_2\right) = 2 \cdot \vec{n} \cdot \vec{\vec{k}} \cdot \nabla\tau_1^e \tag{4.17}$$

The $\tau^e$ at boundary has a reduced dimension compared that in the domain so it only varies along the boundary face, thus its gradient $\nabla\tau^e$ and associated velocity $\vec{\vec{k}} \cdot \nabla\tau^e$ vary along the boundary surface and are always perpendicular to the normal direction of boundary, i.e.,

$$\vec{n} \cdot \vec{\vec{k}} \cdot \nabla\tau^e = 0 \tag{4.18}$$

This justify that no flow boundary condition $\vec{n} \cdot \frac{\partial \vec{u}}{\partial t} = 0$ is always guaranteed in our extended FMM when dealing with boundary effect.

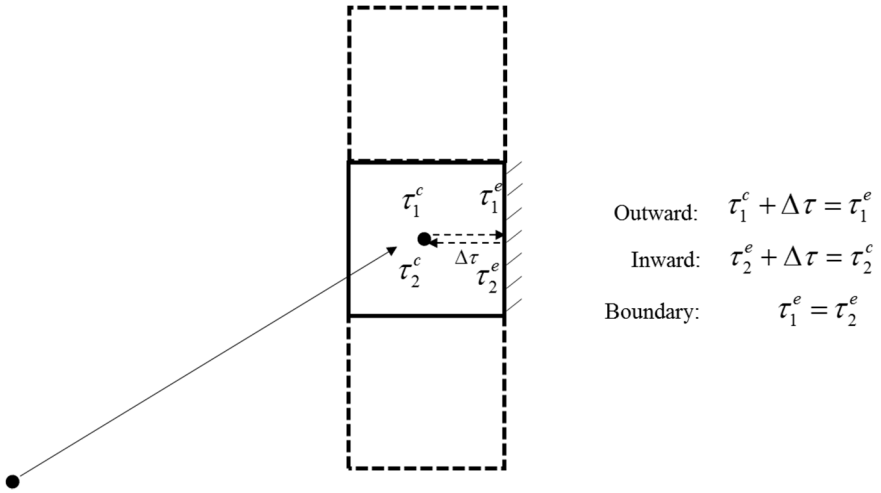


**Figure 4.1 Illustration of $\tau$ values at boundary cells in extended FMM**

### *4.2.4 Drainage Volume Partition with Streamline*

When multiple active wells are involved in a reservoir, the potential interference must be accounted for. One rising question is how the drainage volume of each well has been influenced. This kind of diagnostic information could be very valuable for well placement optimization and reservoir management. Regarding above question, streamline-based method has been demonstrated as an effective tool for accessing these information.

In a typical streamline workflow, we first obtain the flux field from full finite difference simulator to construct the streamlines. Then these fluxes can be analytically integrated on a cell by cell basis, e.g., Pollock's algorithm, to trace out the trajectories. It is very powerful and comprehensive for complex situations and can be used for general grid reservoir geometries with complex grid system. To obtain the drainage volume partition, the streamlines are started from the grid block centers and traced backwards to the associated producers. Once the partition is completed, one can easily define drainage

volumes, sweep volumes, well-pair connections, well allocation factors, etc. Although we realize the power and strength of streamline-based flow diagnostics, there are some disadvantages. For example, due to the transient nature of the flow in unconventional reservoirs, the streamlines are required to be recomputed every time step based on the updated flux field. Special care is also demanded to handle the general corner point grids where pinch out, degeneration or distorted hexahedral cells are often met.

### *4.2.5 Drainage Volume Partition with Fast Marching Method*

Besides the streamline-based method, we are more interested in developing a rapid and less complex partition method that can fully take advantage of the transient nature of unconventional reservoir. The fast marching method can naturally capture the fronts from multiple sources at the same time but there is an underlying assumption that pressure front stops when it meets another. Therefore it only gives correct solution for the special situation when the pressure fronts carry the same strength. For general application, the original fast marching algorithm must be modified to take into account the competition between different fronts. In the following discussion, we call the modified version as "superposition FMM" since it is based on the principle of superposition.

To elaborate the superposition FMM, let us first review the procedure in original FMM. The rationale behind this method is that the wells in unconventional reservoirs always display a long-term transient flow behavior, in direct contrast with conventional reservoirs where transient flow only last few days or weeks. Therefore, we can transform the diffusivity equation and apply the high frequency limit to it. Eventually, applying

asymptotic expansion to the diffusivity equation will lead to the Eikonal equation that governs the pressure front propagation in an isotropic medium (Vasco et al. 2000)

$$\sqrt{\alpha}\left|\nabla \tau(\vec{x})\right| = 1 \tag{4.19}$$

where $\tau$ is the diffusive time of flight (DTOF). Fast marching method can be used to efficiently solve Eq. (4.19) to compute the pressure front propagation. It is a single-pass method which utilizes the fact that the value of $_{\tau}$ for the first-order PDE depends only on the value of $\tau$ along the characteristics passing through the point $\vec{x}$ (Sethian 1996). Thus, the solution of $\tau$ can be constructed in an orderly one-pass fashion from smaller values to larger values. The basic framework of fast marching method comprises the following steps (Sethian 1999).

During the marching process, a min-heap data structure is generally used to systematically store $\tau$ and locate the proper grid point to update. The original FMM algorithm only stores the information of $\tau$ at each grid block and does not include the information about the original source of a particular pressure front, which is crucial for the coexistence of propagating fronts from multiple sources.

The superposition FMM will include two critical steps to remedy this drawback. In the first step, we would extend our data structure to include more information like the source well of each pressure front and cumulative drainage volume during the marching process. By doing this, we can separate the early drainage volume covered by different sources. However, this partition does not take into account the strength difference between fronts. Therefore, in the second step, we propose a new criterion to dynamically shift the partition boundary when fronts meet each other, as shown in Figure 4.2. More specifically,

we compare the normal component of velocity induced by each wells, which is proportional to pressure derivative, and shift the partition boundary until the normal component is the same.

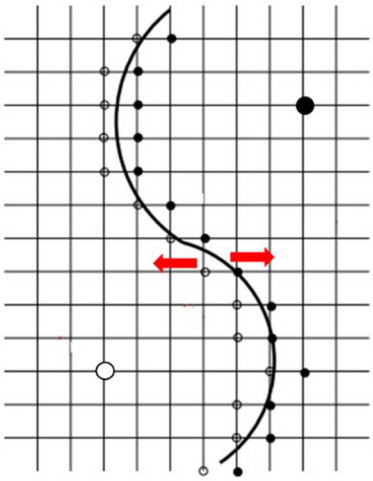

**Figure 4.2 Pressure front competition between different sources in superposition FMM**

The rationale behind this criterion is based on the superposition, where the total pressure drop at any location is the sum of the pressure drops at that point caused by each pressure front $\tau$

$$\Delta p\left(\vec{x},t\right)=\Delta p_1\left(\tau_1,t\right)+\Delta p_2\left(\tau_2,t\right)+\ldots \tag{4.20}$$

Since the pressure drop caused by a particular front *i* is independent of others, the pressure derivative along the front *i* is only a function of itself, i.e.,

$$\left(\partial\Delta p/\partial\tau\right)_i=\partial\Delta p\left(\tau_i,t\right)/\partial\tau_i \tag{4.21}$$

Therefore, the largest value among normal components of velocity due to each individual well at that location indicates the largest contribution of that particular well, thus we

associate this location to that source well, as shown in Figure 4.3. Following section will show how we derive the mathematical expression for this magnitude.

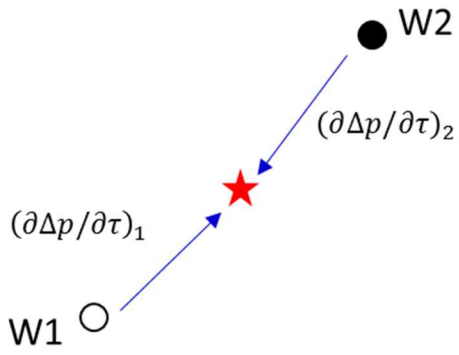


**Figure 4.3 Schematic diagram of drainage volume partition criterion**

### *4.2.6 Asymptotic Pressure Approximation*

In above section, the criterion of drainage volume partition requires the solution of pressure derivative that can be efficiently obtained from the semi-analytical asymptotic pressure approximation, as an extension of the methodology of pressure transient analysis. This semi-analytical method is capable to capture not only reservoir heterogeneity but also the complex fracture and well configurations. It has been developed and applied to unconventional reservoir to simulate the pressure response and estimate the drainage volume (Datta-Gupta et al. 2011; Xie et al. 2012; Zhang et al. 2013). The key asymptotic solutions will be summarized in the following.

The main idea of asymptotic pressure approximation is to reduce the 3-D diffusivity equation into an equivalent 1-D form and then integrate it over a streamtube volume from the well into the reservoir, up to a certain $\tau$ value. The pressure can be

expressed as a function of contour $\tau$ and the two bi-streamfunction, $\psi$ and $\chi$ (Bear 1972), therefore the Darcy's law for inward flux is linked to the pressure derivative by using Eq. (4.19)

$$\begin{aligned} q &= -\frac{1}{\mu}\vec{n}\cdot\vec{\vec{k}}\cdot\nabla p \\ &= -\frac{1}{\mu}\left(\frac{w(\tau)}{\phi}\nabla\tau\right)\cdot\vec{\vec{k}}\cdot\nabla p \\ &= -\frac{1}{\mu}\left(\frac{w(\tau)}{\phi}\nabla\tau\right)\cdot\vec{\vec{k}}\cdot\left(\frac{\partial P}{\partial\tau}\nabla\tau+\frac{\partial P}{\partial\psi}\nabla\psi+\frac{\partial P}{\partial\chi}\nabla\chi\right) \\ &\approx -c_t w(\tau)\frac{\partial P}{\partial\tau} \\ &\approx c_t w(\tau)\frac{\partial\Delta P}{\partial\tau} \end{aligned} \tag{4.22}$$

where $c_t$ is the compressibility and the function $w(\tau)$ is related to the drainage pore volume by

$$w(\tau)=\frac{dV_p(\tau)}{d\tau} \tag{4.23}$$

From Eq. (4.22), we can see that once flux is given, the pressure derivative can be calculated and plugged into the criterion Eq. (4.20).

King et al. (2016) show the detailed derivation of asymptotic pressure solution under different well conditions. For fixed rate drawdown,

$$c_t\frac{\partial p}{\partial t}=-\frac{q_w}{V_p(t)}e^{-\tau^2/4t} \tag{4.24}$$

where we can integrate the solution over the finite domain (no flow outer boundaries) to obtain the equation for $V_p(t)$:

$$q_w = \iiint_{Domain} d^3x \nabla \cdot \vec{u} = \frac{q_w}{V_p(t)} \iiint_{Domain} d^3x \phi e^{-\tau^2/4t}$$
$$V_p(t) = \iiint_{Domain} d^3x \phi e^{-\tau^2/4t} \tag{4.25}$$

Flux solution can be obtained by integrating its spatial gradient from a location in the reservoir to the far field boundary where $q \to 0$ and $\tau \to \infty$, thus at that location the flux is related to flux in the wellbore by

$$q(\tau,t) = q_w \frac{V_0(\tau,t)}{V_0(t)} \tag{4.26}$$

where

$$V_0(\tau,t) = \int_{\tau'=\tau}^{\infty} dV_p(\tau') e^{-\tau'^2/4t}$$
$$V_0(t) = V_0(0,t) = V_p(t) \tag{4.27}$$

In above expression of $V_0(\tau,t)$, exponential term indicates the timing of the contribution of a volume increment to depletion within the reservoir. Eq. (4.26) indicates the flux at any location is proportional to the well rate by the volume ratio. Plugging Eq. (4.26) into Eq. (4.22) gives

$$\frac{\partial \Delta P}{\partial \tau} = \frac{q_w}{c_t w(\tau)} \frac{V_0(\tau,t)}{V_0(t)} \tag{4.28}$$

Similarly, for fixed bottle-hole pressure drawdown, the pressure drop at a particular location is proportional to the bottle-hole pressure drawdown by a volume ratio, defined as

$$\Delta p(\tau,t)=\Delta p_{wf}\frac{W_1(\tau,t)}{W_1(t)} \tag{4.29}$$

where

$$\begin{aligned} W_1(\tau,t) &= \int_{\tau'=\tau}^{\infty}\frac{d\tau'}{w(\tau')}\cdot\int_{\tau''=\tau'}^{\infty}dV_p(\tau'')\cdot\tau''\cdot e^{-\tau''^2/4t} \\ W_1(t) &= W_1(0,t) \end{aligned} \tag{4.30}$$

Taking the derivative of Eq. (4.29) w.r.t. $\tau$ gives

$$\frac{\partial\Delta P}{\partial\tau}=\frac{\Delta p_{wf}}{w(\tau)}\frac{V_1(\tau,t)}{W_1(t)} \tag{4.31}$$

where

$$V_1(\tau,t)=\int_{\tau'=\tau}^{\infty}dV_p(\tau')\cdot\tau'\cdot e^{-\tau'^2/4t} \tag{4.32}$$

For the detailed derivation of above formulation, the readers are referred to King et al. (2016).

## 4.3 Applications: Results and Discussion

### *4.3.1 Improved Simulation of Single Well*

The FMM-based 1-D pressure solution has been successfully applied to multiple unconventional reservoirs for transient flow regime simulation (Fujita et al. 2015; Zhang et al. 2016). However, when the pressure front ‘touches’ the boundary or ‘interferes’ with others, the pressure solution needs additional improvement. In our proposed methodology,

the reflected $\tau$ map from boundary/interface will be incorporated to solve the additional pressure drop on the new $\tau$ map, as illustrated in Figure 4.4.

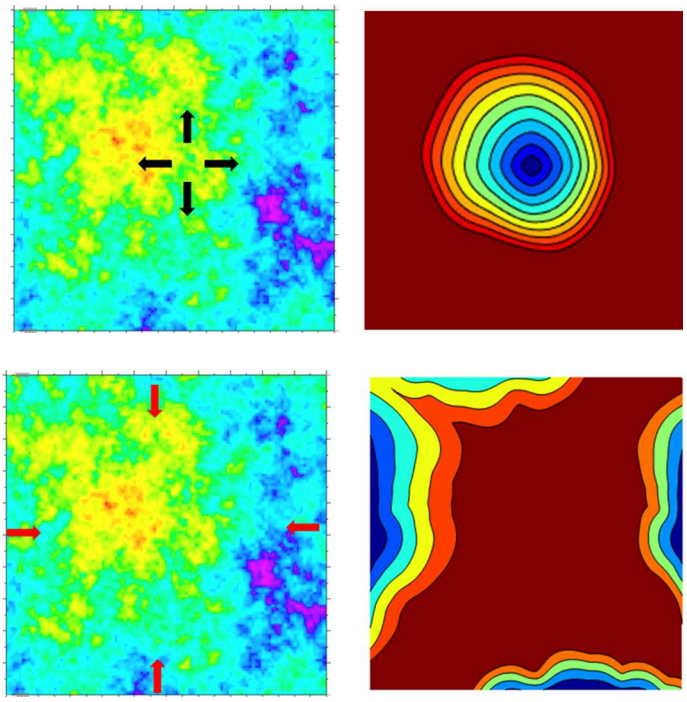

**Figure 4.4 Outward (incident) and inward (reflected) $\tau$ map**

Recall the diffusivity equation after 1-D transformation (Fujita et al. 2015; Zhang et al. 2016)

$$\frac{\partial}{\partial \tau}\left( w(\tau)\frac{\partial P}{\partial \tau}\right) = w(\tau)\frac{\partial P}{\partial t} \tag{4.33}$$

In this equation, the only variable describing reservoir properties is $w(\tau)$, which is the derivative of drainage volume $V_p(\tau)$ w.r.t. $\tau$. This equation works well for single $\tau$ coordinates. When we consider the multiple front arrivals, we need to combine these $\tau$

maps into a single system that is required in 1-D FMM Eq. (4.33), therefore at any location, we sum up the volumetric elements reached by each front arrival

$$V_p(\tau) \equiv \sum_n \sum_{ijk} PV_{ijk} \left\{ \max\left[ 1, \min\left[ 0, \frac{\tau - \tau_{n,\min}}{\tau_{n,\max} - \tau_{n,\min}} \right] \right] \right\} \tag{4.34}$$

where *i*, *j*, *k* are cell locations and n represents *n*th arrival of pressure front. The corresponding drainage volume for multiple $\tau$ coordinates can be reduced to the definition in Eq. (4.7)

$$\begin{aligned} V_p(t) &= \int dV_p(\tau) e^{-\tau^2/4t} \\ &= \sum_n \sum_{ijk} PV_{ijk} e^{-\tau^2/4t} \frac{d\tau}{\tau_{n,\max} - \tau_{n,\min}} \\ &= \sum_{ijk} PV_{ijk} \sum_n e^{-\tau_n^2/4t} \\ &\Leftrightarrow \iiint_{Domain} d^3x \phi \left\{ e^{-\tau_1^2/4t} + e^{-\tau_2^2/4t} + \ldots + e^{-\tau_n^2/4t} \right\} \end{aligned} \tag{4.35}$$

As a result, the corresponding $w(\tau)$ is the derivative of $V_p(\tau)$ combined w.r.t the mixed $\tau$ system. Figure 4.5 shows an example of function $w(\tau)$ vs. $\tau$ from single and multiple arrivals. We can see that before the pressure front reaches the boundary, there is no difference between them because no additional drainage volume will be accounted for. After that, the drainage volume will be enlarged by additional reflection front, therefore giving a larger $w(\tau)$.

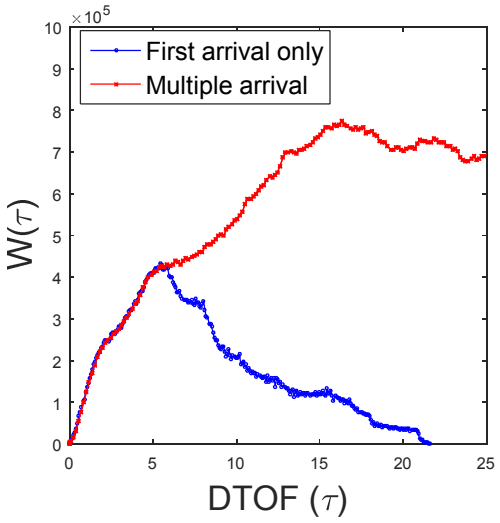


**Figure 4.5 Comparison of function $w(\tau)$ vs. $\tau$ from single and multiple arrivals**

Plugging above improved function $w(\tau)$ into original 1-D form Eq. (4.33) will give multiple pressure drops at the same location since it will have multiple arrivals. With superposition, we will collect the total pressure drop at that location

$$\begin{aligned} \Delta p\left(\vec{x},t\right) &= \sum_{i=1}^{n} \Delta p\left(\tau_i,t\right) \\ \tau(\vec{x}) &= \left\{\tau_1,\tau_2,\tau_3,...,\tau_n\right\} \end{aligned} \tag{4.36}$$

From this equation, we can see that the pressure gradient will be no longer aligned with any particular $\tau$ contour, which is the basic assumption in original FMM-based 1-D simulation. In addition, the accuracy of pressure solution depends on the number of reflection terms that in turn relies on the total simulation time $t$. It is important to recognize that no matter how many terms we use in the superposition, we only need to solve the partial differential equation Eq. (4.33) once. In practice, it is impossible to account for infinite reflection fronts. We use the criterion that when the exponential term

$e^{-\tau^2/4t}$, which indicates the timing of the contribution of a volume increment to depletion within the reservoir, is very small, the additional pressure drop will be negligible. For example, when the cutoff $\tau$ satisfies $\tau/\sqrt{4t} > 2$, the corresponding exponential value will be less than 1.8%.

In order to compare the effects of considering multiple pressure fronts, we design a synthetic example with a single producer well in a typical shale gas reservoir, described in Table 4.1. Figure 4.6 shows the well location in the permeability map and the corresponding DTOF $\tau$ map from original FMM that only considers first arrival, as well as the DTOF $\tau$ map from boundary reflection. This reflection map requires a second run of fast marching algorithm with starting points along the boundary whose initial values are recorded in the first run.

| **Properties** | **Value** | **Unit** |
|---|---|---|
| Reservoir Porosity | 10 | % |
| Fluid Viscosity | 0.03 | cp |
| Total Compressibility | 1.2E-4 | $psi^{-1}$ |
| Initial Reservoir Pressure | 5470 | psi |
| Production Rate | 100 | MSCF/D |
| Reservoir Thickness | 100 | ft |
| Reservoir Size | 2000 x 2000 | $ft^2$ |
| Total Simulation Time | 34 | year |

**Table 4.1 Basic reservoir properties used for the simulation**

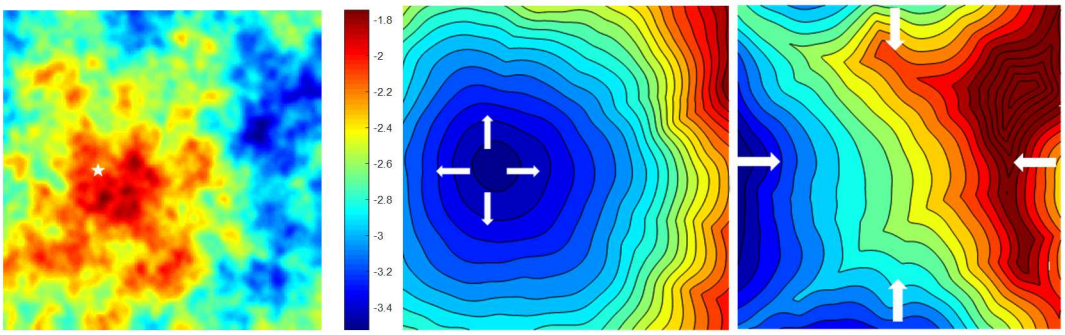


**(a)** **(b)** **(c)**

**Figure 4.6 (a) Permeability field (log); Corresponding (b) incident and (c) reflected DTOF ( $\tau$ ) map**

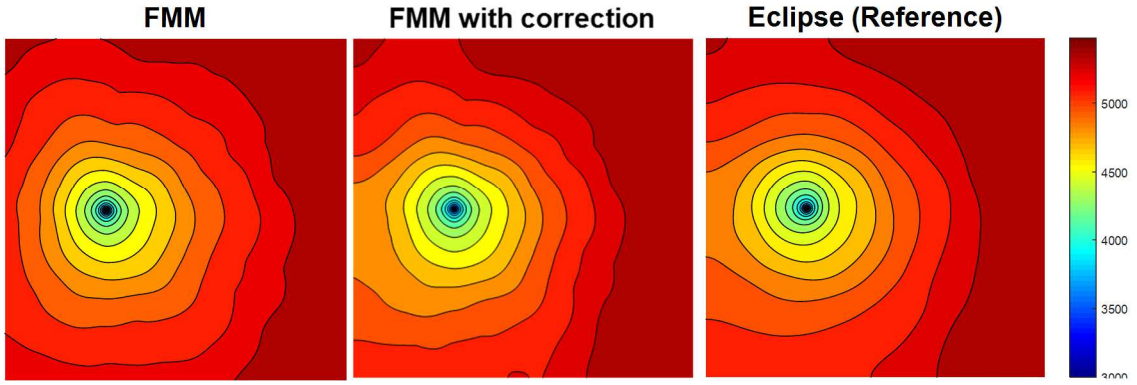


**(a)** **(b)** **(c)**

**Figure 4.7 Comparison of pressure distribution from (a) original FMM; (b) extended FMM with additional reflection correction and (c) standard finite difference simulation from Eclipse**

Figure 4.7 compares the final pressure distribution comparison between original and extended FMM 1-D results against standard full finite difference solution from Eclipse. Comparing the original FMM 1-D result with the Eclipse results, we can see some obvious discrepancy in the region close to the boundary. Note that in original 1-D coordinate transformation, we made an assumption that pressure contour coincide with the $_{\tau}$ contour (see Eq. (4.22)), therefore, the calculated pressure distribution has the same pattern with DTOF map but different from Eclipse solution after pressure front reaches the boundary.

Realizing the discrepancy, we introduce additional pressure drop from reflection DTOF map to compensate the difference. As we can see from Figure 4.7 (b) and (c), after the additional pressure drop from reflection DTOF, the pressure contour is much closer to the full simulation result. Beyond the pressure contour, the Figure 4.8 also shows the comparison of bottom-hole pressure (BHP) corresponding to the results in Figure 4.7. It indicates that at early time the curves coincide with each other because there is no boundary effect. Once the boundary has been touched, the BHP calculated from original FMM deviates from Eclipse result and difference increases with time. The addition of pressure drop from reflection pressure front can effectively bring the curve back to the full simulation result. From these figures, we can clearly see that both pressure distribution and well result have been improved by considering multiple front arrivals. This conclusion will provide a solid foundation for us to deal with following well interference problems.

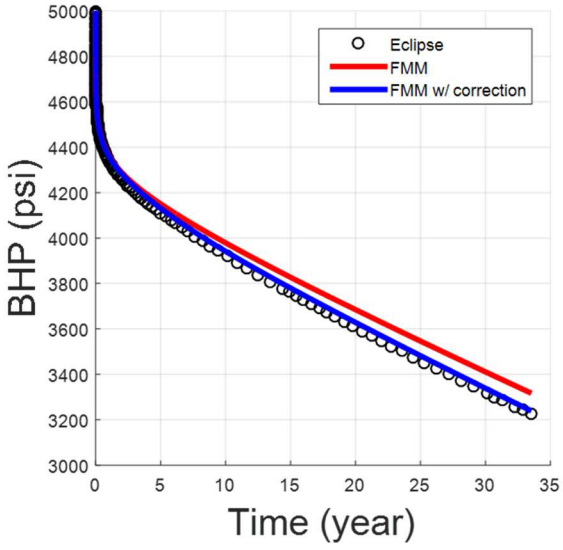


**Figure 4.8 Comparison of bottom-hole pressure (BHP) from original and extended FMM 1-D simulations and standard finite difference simulation from Eclipse**

### *4.3.2 Verification: FMM vs. Streamline*

While above section explains how to deal with the boundary effect, this section will focus on how to get reasonable drainage volume partition when multiple well coexists. Traditionally, streamline method has been proved to a very efficient and reasonable method to visualize the drainage volume partition between multiple wells. Figure 4.9 illustrates the basic procedure. It relies on the standard finite difference simulator to give the flux field and trace out the streamlines from cell center back to the well based on the given flux. The partition is given by grouping the cells with same associated well. As a widely used method, streamline method gives reasonable and reliable partition in terms of flux. In this chapter, we will the partition results from streamline method as a reference for our proposed superposition FMM method.

Unlike streamline method that relies on the flux field from standard finite difference method, original FMM procedure is more straightforward, as shown in Figure 4.10. It directly mimics the outward pressure wave and tracks the pressure fronts from different sources, thus it is easy to associates the cell to the source whose front arrives there first. The resulting partition boundary thus is a line which has the same ‘travel’ time to arrive at neighboring sources.

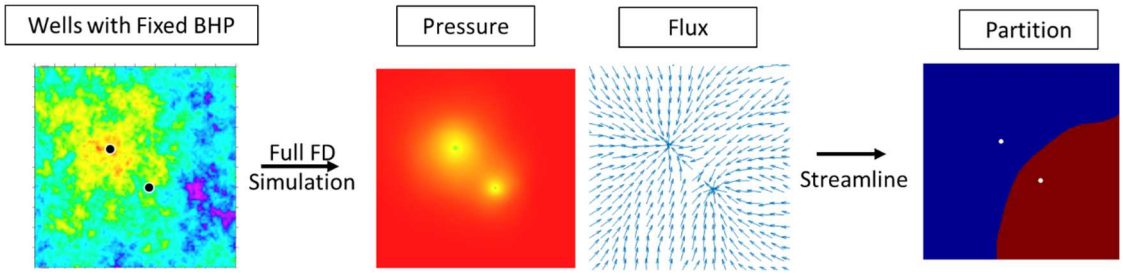


**Figure 4.9 Drainage volume partition using streamline method**

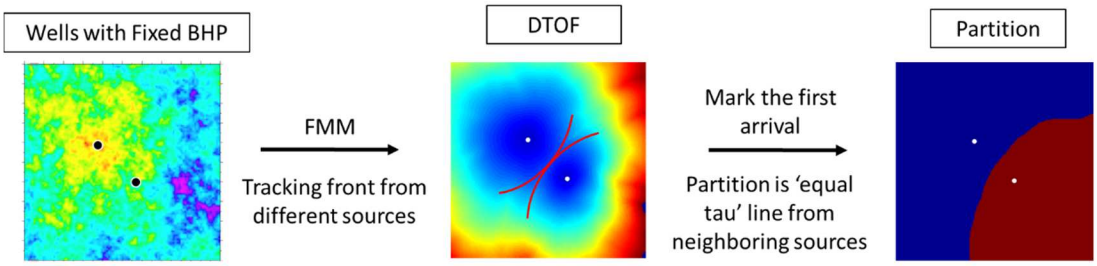


**Figure 4.10 Drainage volume partition using FMM**

From comparison between Figure 4.9 and Figure 4.10, we can see that FMM can give similar partition with streamline method. However, this is not always true for more general situations. Figure 4.11 shows three cases that original FMM has limitation to capture the correct partition between wells. Figure 4.11 (a) indicates two wells but left well has a twice rate of right well, therefore it should not be an equal partition, instead the left well will take over more volume, as indicated from streamline results. FMM partition gives an equal partition and thus fails to capture the correct one because this method only tracks the impulse of source without specific well schedule information like well constraints and values. Another case in Figure 4.11 (b) indicates that even the two wells have the same rate, FMM still fails to capture the same trend with streamline if the wells start at different time. In this case, left well starts much earlier followed by the right well,

so the FMM the partition boundary stops at the region where they first meet, close to the right well because it only tracks the first arrival of pressure front. This is in contrast to the 'almost equal' partition from streamline method. The last case in Figure 4.11 (c) indicates that even the wells have same rate and starting time, the discrepancy between FMM and streamline method could be innegligible because FMM does not consider the decay of pressure front strength through the heterogeneous reservoir.

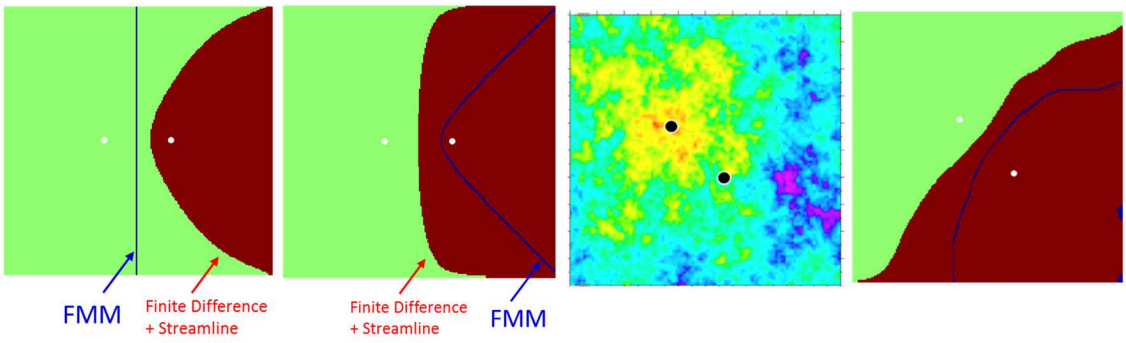


**Figure 4.11 Limitation cases of original FMM volume partition (contrast by streamline): (a) wells with different rates but same starting time; (b) wells with same rate but different starting time; (c) wells with same rates and starting time but in heterogeneous reservoir**

To amend above issues, superposition FMM utilizes Eq. (4.21) to shift the boundary during the marching process. The new comparisons between streamline and superposition FMM are shown in Figure 4.12--Figure 4.14, where the original FMM partition boundary are marked as blue curve for reference. To exclude the boundary influence, we look at the partition at some time when pressure front has not yet arrived at the boundary. This represents the majority of what happens in unconventional reservoir. From Figure 4.12(a), we can see that with the proposed criterion, the boundary between

wells has been shifted from original ‘equal’ partition boundary to a curve close to the right well that operates under a half rate of left well. This new result gives pretty close partition from streamline solution.

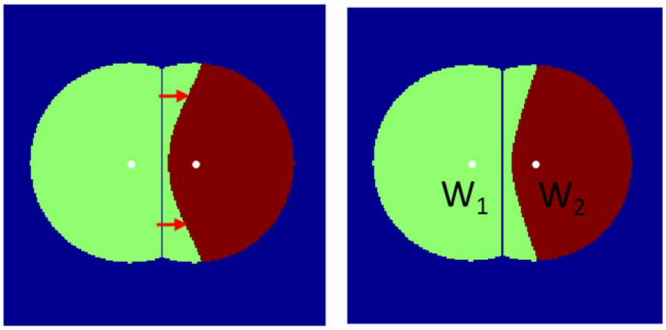


**(a) Superposition FMM** **(b) Streamline**

**Figure 4.12 Comparison of streamline and superposition FMM partition: wells with different rates but same starting time**

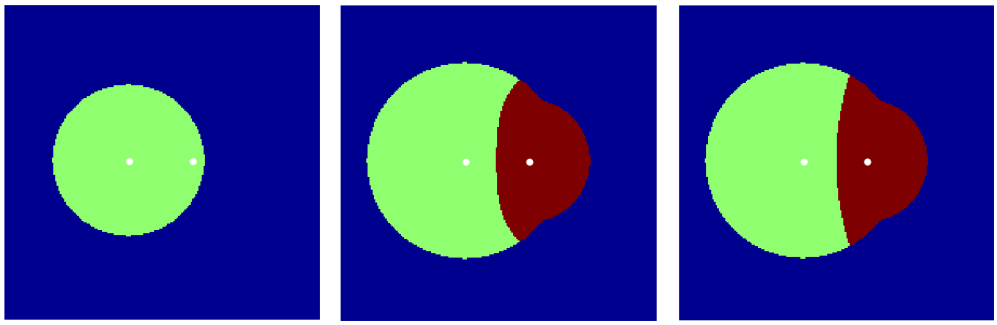

**(a) Drainage volume (@ 3rd year)** **(b) Superposition FMM (@ 5 th year)** **(c) Streamline (@ 5th year)**

**Figure 4.13 Comparison of streamline and superposition FMM partition: wells with same rate but right well starts 3 year later**

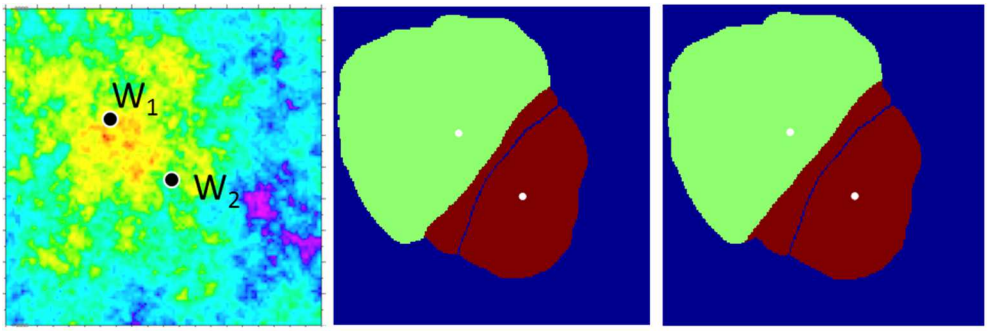


(a) Permeability (log) field (b) Superposition FMM (c) Streamline

**Figure 4.14 Comparison of streamline and superposition FMM partition: wells with same rates and starting time but in heterogeneous reservoir**

Figure 4.13 demonstrates that proposed FMM also works for wells with same rate but starting at different time. In this demo case, the left well produces 3 years earlier than the right well and pressure front has already reached the right well. Original FMM cannot capture the subsequent partition because it only record the earliest arrival. In contrast, the superposition FMM can effectively capture the partition and give the consistent result with streamline. It has also shown the capability to capture the correct partition in complex heterogeneous case, compared with original FMM (blue line) in Figure 4.14. Although it does not give exactly the same partition with streamline, the result is still very reasonable considering the simple and fast algorithm used in FMM.

### *4.3.3 Application to Multi-Well Performance*

In multi-well interference scenario, after we get the partition from superposition FMM, we can separate each well with associated drainage volume and then solve the well performance using 1-D transformation, respectively. To verify the proposed superposition FMM, a synthetic case with two wells is built using the properties listed in Table 4.1 and

permeability field in Figure 4.14 (a). These two wells are operated under the same fixed production rate and they are set to produce at the same time.

Figure 4.15 shows the partition comparison of two wells using streamline and superposition FMM at late time when pressure fronts pass through the whole domain. To get a reasonable partition, we also need to consider the boundary effect in our asymptotic pressure formulations. Note that it is not a perfect match between the superposition FMM and streamline results, but still much better compared with original FMM. It would be more demonstrated to understand the importance of this improvement by looking at the individual well performance using its own partitioned drainage volume. Figure 4.16 gives both well performance based on original FMM partition result, benchmarked with Eclipse full simulation results. We can clearly see that FMM results deviate significantly from Eclipse results because of the incorrect drainage volume partition between wells. We also introduce the aforementioned boundary reflection term into FMM. The curves show that it can improve the well solution at late time when boundary effect matters but it won't help reduce the gap due to incorrect drainage volume partition. In other words, the associated drainage volume has dominant effect in multi-well interference scenarios with FMM. Figure 4.17 plots the same comparison between Eclipse solution and extended FMM using the improved drainage volume partition from superposition FMM. We can see the significant improvement from Figure 4.16 to Figure 4.17. It is worthy to mention that we still see pressure discrepancy at very late time, which reflects the partition error near boundary, as shown in Figure 4.15.

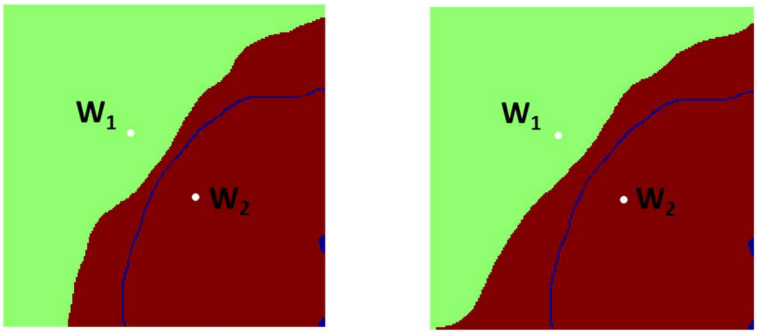


(a) Superposition FMM (b) Streamline

**Figure 4.15 Comparison of streamline and superposition FMM partition at late time (blue line represents original FMM for reference)**

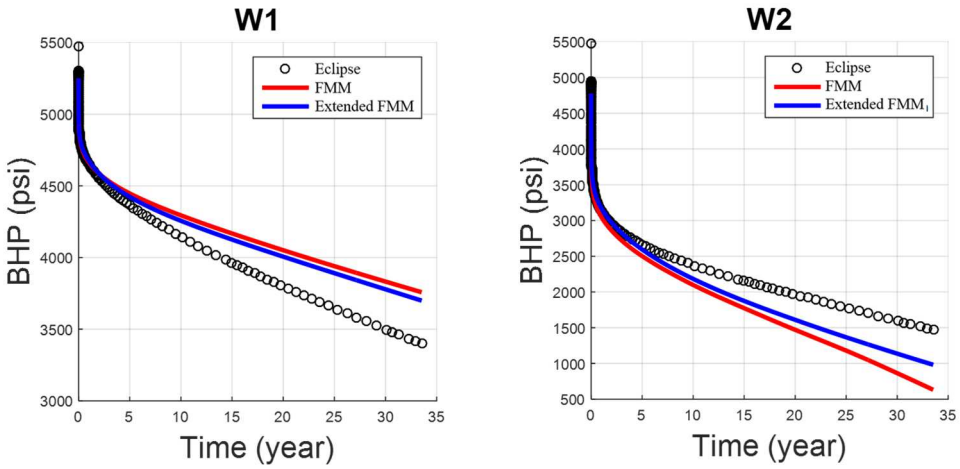


**Figure 4.16 Individual well performance based on original FMM partition**

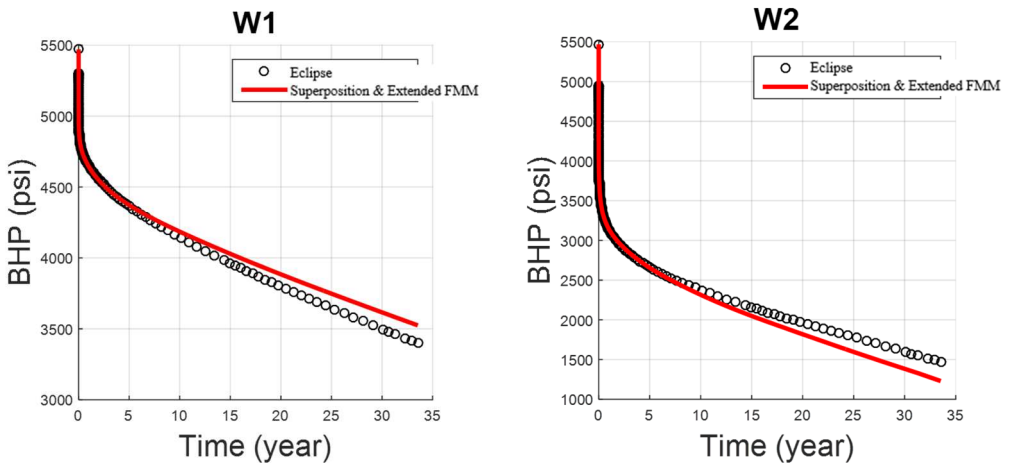


**Figure 4.17 Individual well performance based on superposition FMM partition**

Besides above conventional two well competition problem, another more intriguing application in unconventional reservoir development is the strong infill horizontal well interference because the new well are generally placed close to the existing well. This is usually described using the terminology “parent-child well interference”. This interference, as well as long-term transient nature, has implications on the well performance. For a multi-stage fractured horizontal well in an unconventional reservoir, the actual drainage volume is eventually confined to the so-called “stimulated reservoir volume” (SRV), which represents the rock volume that has been effectively stimulated using hydraulic fracture, because the reservoir permeability is so low that only stimulated fracture with permeability several orders of magnitude greater than matrix can provide a flow path. However, with the multi-well interference, the assessment of effective drainage volume or contributing SRV is not straightforward and becomes a priority for the estimated ultimate recovery and pressure depletion in the reservoir near producing well.

In other words, it is not always prudent to drill “child” well (infill) close to the “parent” well (existing) due to strong pressure depletion.

To examine the power of superposition FMM workflow, we apply it to a synthetic example to illustrate how the performance of “parent” well has been degraded when “child” (infill) well is turned to production. This workflow can provide insights into well interference in terms of drainage volume competition, which is hard to directly acquire through conventional finite difference simulation. This example is comprised of three parallel horizontal wells: one existing and two surrounding infill wells. Every well has ten stages with assumption of one main fracture in each stage. To simplify, the fracture conductivity is considered to have infinite conductivity compared with ultra-low matrix permeability. The basic reservoir and fluid properties remain the same as those with Table 4.1 except that all horizontal wells are under the constant BHP constraint of 2000 psi. Before the addition of infill wells, the parent well (HW1) has been put on production for 2 years.

Figure 4.18 indicates the corresponding drainage area after 2 years but just before the addition of child wells. It is clear that this well has started to drain the area of potential infill wells. Figure 4.19 (a) shows the separated drainage volume partition between three wells after another 3 years production (at the end of fifth year) with superposition FMM method. It is clear that the infill child wells (HW2 and HW3) have taken over some volume supposed to be part of HW1’s. Again, Figure 4.19 (b) shows the partition from streamline as a reference that supports the effectiveness of superposition FMM. Once the partition is given, the next step is to use each associated drainage volume to solve the transformed 1-

D diffusivity equation Eq. (4.33) for each well. Since our focus in this case is the impact on parent well due to child wells, therefore, we only look at the performance of parent well HW1.

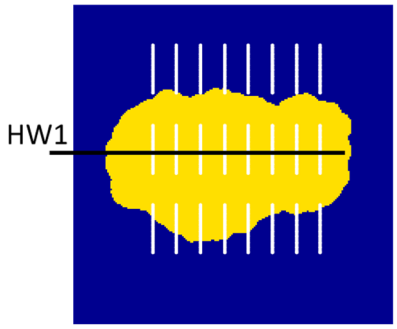


**Figure 4.18 Drainage area of one single parent well without child wells (at second year)**

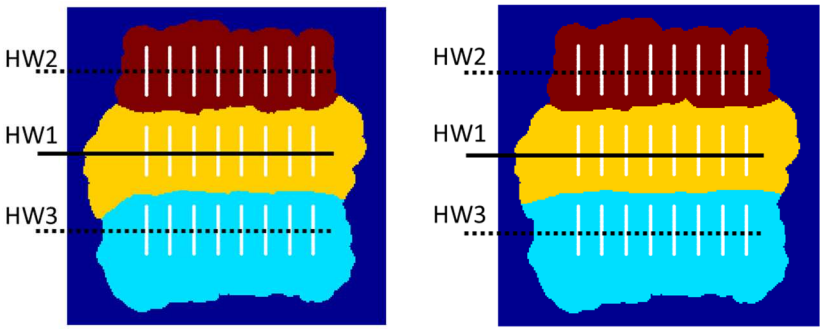


**(a) Superposition FMM** **(b) Streamline**

**Figure 4.19 Drainage volume partition after introducing two child wells (at fifth year)**

Figure 4.20 shows how the drainage volume curve and its derivative $w(\tau)$ function change once the infill wells have been turned to production. With the extension of timeframe from 2 years to 5 years, the maximum $\tau$ increases but drainage volume of HW1 decrease, which was taken over by child wells. The corresponding $w(\tau)$ function,

i.e., the derivative of drainage volume, deviate from each other at a certain $\tau$ value where well interference starts. It is important to emphasize again that in our 1-D diffusivity equation Eq. (4.33), $w(\tau)$ function is the only parameter that contributes to the transmissibility term. By introducing this change into $w(\tau)$ function into FMM 1-D equation, we can see the production rate jump after 2 years, as shown in Figure 4.20. However, for a longer time, the production rate from FMM (solid blue line) matches well with Eclipse (black circle). This result demonstrates the accuracy of drainage volume partition from FMM. For illustrating purpose, we also plot rate response of HW1 in the case there is no infill well added so that we can get a sense of the impact on HW1 by infill wells.

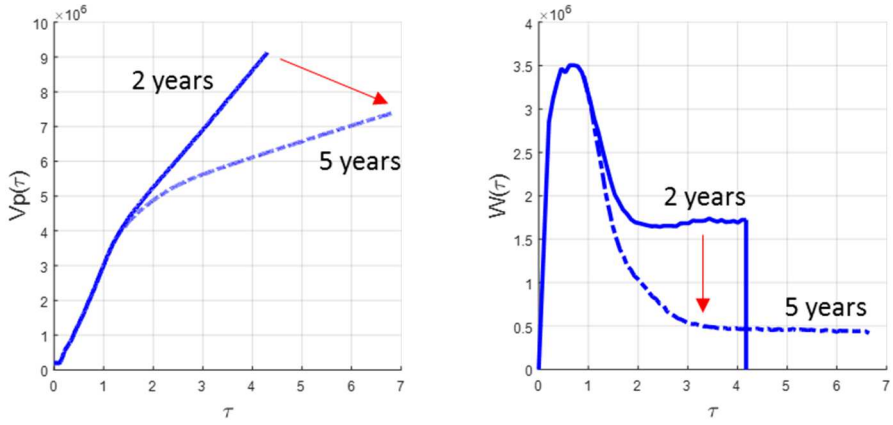


**Figure 4.20 Variation of drainage volume and $w(\tau)$ function of HW1**

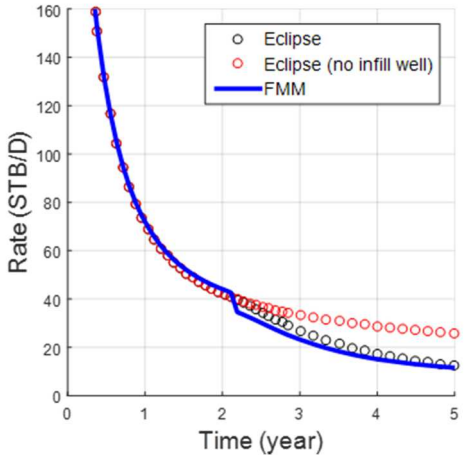


**Figure 4.21 Comparison of predicted rate of HW1 from FMM and Eclipse**

### *4.3.4 Rapid Well Spacing Optimization*

For the multi-well design in a high-resolution large-scale reservoir, the idea of reservoir compartmentalization provides an efficient approach to optimize the well layout and avoid solving all wells simultaneously in conventional finite difference method. We have shown in above section that drainage volume associated with individual well is the dominant factor of accurate well performance prediction and demonstrated the potential of proposed superposition FMM in the application of multi-well optimization.

In this section, we combine the drainage volume partition and asymptotic pressure approximation to achieve a rapid simulation-free optimization of horizontal well spacing. The objective function of our optimization problems represents the best production performance of the placed wells. According to integrability condition in asymptotic pressure approximation (King et al. 2016), for the fixed bottom-hole flowing pressure, the sandface flux is related to pressure drawdown and drainage volume by

$$q_{sf}(t) = c_t \Delta p_{wf} \frac{V_1(t)}{W_1(t)} \tag{4.37}$$

where the quantities $V_1(t)$ and $W_1(t)$ is given in Eq. (4.30) and Eq. (4.32). Similarly, for the fixed production rate, the pressure drawdown is related by

$$\frac{d\Delta p_{wf}}{dt} = \frac{q_w}{c_t V_0(t)} \tag{4.38}$$

For rare cases the horizontal well will be under rate constraint, therefore, in our following numerical experiments, the objective function is the cumulative production

$$Q(t) = \int_0^t q_{sf}(t')dt' \tag{4.39}$$

The reservoir model is constructed based on the available data from literation as listed in Table 4.2. Considering the complexity of hydraulically fractured reservoirs, we perform the FMM optimization to maximize the total gas production from two horizontal wells with nine fracture stages, assuming one dominant fracture in each stage (Cipolla et al. 2010), as shown in Figure 4.22.

| Properties | Value | Unit |
|---|---|---|
| Reservoir size | 2000 x 2000 x 100 | $ft^3$ |
| Simulation grid | 200 x 200 x 1 | - |
| Fracture height | 100 | ft |
| Porosity | 10 | % |
| Total simulation time | 3 & 30 | years |
| Bottom hole pressure | 3000 | psi |
| Fluid viscosity | 0.03 | cp |
| Initial reservoir pressure | 5470 | psi |
| Total compressibility | 1.2e-4 | $psi^{-1}$ |
| Fracture half-length | 200 | ft |
| Number of fracture stage | 9 | - |
| Fracture conductivity | 100 | md-ft |

**Table 4.2 Basic reservoir properties used for the simulation**

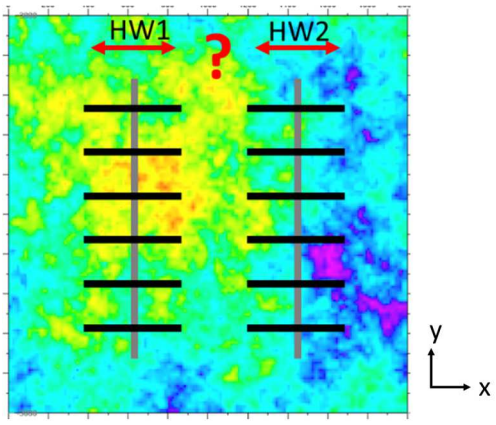


**Figure 4.22 Well spacing optimization of two horizontal wells in heterogeneous reservoir**

For illustrating purpose here, the varying fracture length and spacing is not considered, therefore, the major variable we work on is the well spacing. We use single porosity approach with planar fractures with very high permeability values, in contrast to the matrix permeability. One thing to emphasize is that, in single porosity approach, each fracture stage is usually modelled using a tartan grid system, i.e., logarithmically local grid refinement near fracture. In our optimization problem, a uniform grid system is used to avoid reconstructing the grid system whenever fracture location is changed. As a result, the fracture cell does not reflect the realistic fracture dimension. To offset this negative effect, we adjust the permeability of the fracture cells in accordance to the given fracture conductivity. This adjustment may have some impact on the duration of flow regimes at the vicinity of the fractured wellbore and affect the very early performance, but for relatively longer simulation time, the resulting gas production prediction is still consistent with that from very fine model.

There are a variety of optimization algorithm available to update the variable with the given objective function. Since our main purpose is to demonstrate the effectiveness and efficiency of proposed FMM workflow compared with traditional finite difference method, we only optimize one parameter (well spacing) within this small size reservoir and thus do not necessarily to use the optimization algorithm. In Figure 4.22, we assume the direction of horizontal wells is fixed (along y direction) and our goal is to find the best location in x direction for both wells. To simplify it, we consider all possible locations every 50ft along x direction but exclude these at the very end where fracture is out of domain. There are 30 candidates locations and we need to examine every combination of

2 locations, which involves 435 runs of simulation. Since the model size is small, we choose to exhaustive run of all simulations using both proposed FMM workflow and Eclipse simulator.

To better understand the effect of well spacing on well recovery, we investigate the well performance at both short-term (3 year) and long-term (30 year) using Eq. (4.39) and rank the first few combinations that gives the best well performance. The FMM workflow utilizes the analytical pressure approximation, instead of full numerical simulation, thus it shows overwhelming advantage in terms of computational cost. Table 4.3 is the comparison of CPU time cost by FMM and Eclipse for all 435 runs. Besides the computational cost, we further validate the FMM result against Eclipse result. Figure 4.23 shows the FMM best ranking versus Eclipse best ranking in terms of cumulative production for both short term and long term. We can see that for short term (3 years) the points are more concentrated around the diagonal reference line, indicating that FMM gives a similar ranking with Eclipse. However, in the plot for long term (30 years), the distribution is less concentrated, indicating this accuracy of FMM workflow should be further improved. The main reason is due to the asymptotic pressure approximation is deviated from true solution at late time when flow regime transits from transient to pseudo-steady state. Realizing the tremendous computational time saving, we can apply the proposed FMM workflow for high-resolution reservoir optimization problem or use it as a rapid pre-screening tool before detailed reservoir simulation.

| Method | CPU Time of single run | Total CPU Time |
|---|---|---|
| FMM | < 1s | 3 min |
| Eclipse | 2 min | ~15 hour |

**Table 4.3 CPU time comparison between FMM and Eclipse**

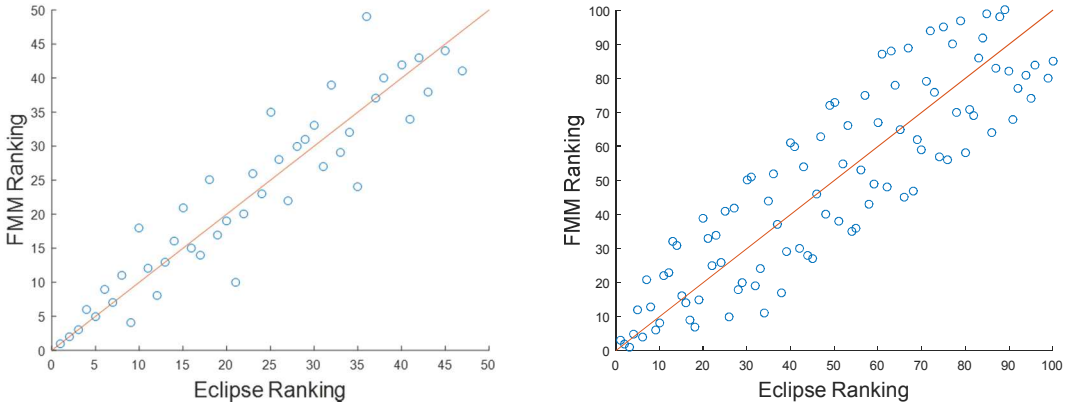


**(a) 3 years** **(b) 30 years**

**Figure 4.23 FMM ranking versus Eclipse ranking for both short term and long term**

Despite of some discrepancy between FMM ranking and Eclipse ranking, they still give the same results for the best optimization results: for short term, the best locations of two wells are 350 ft and 1250 ft along x direction; while for long term, the best locations of two wells are 650 ft and 1650 ft along x direction. Figure 4.24 and Figure 4.25 display the pressure map at 3 years and 30 years in case of these optimized locations, respectively. Since the permeability field in Figure 4.22 is relatively high on the left side but low on the right side, it is reasonable that the optimized well locations are close to the left side for short term but to the right side for long term. In other words, to maximize the production, wells are generally preferred to be in high permeability zone to maximize the production

during early transient flow state, while for long term part of wells are preferred to be in low permeability zone to access more drainage volume as possible.

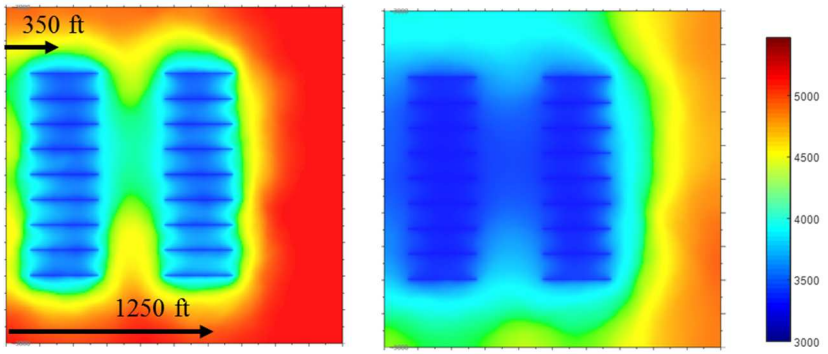


**(a) 3 years** **(b) 30 years**

**Figure 4.24 Pressure distribution at 3 years and 30 years with optimized well location for short term**

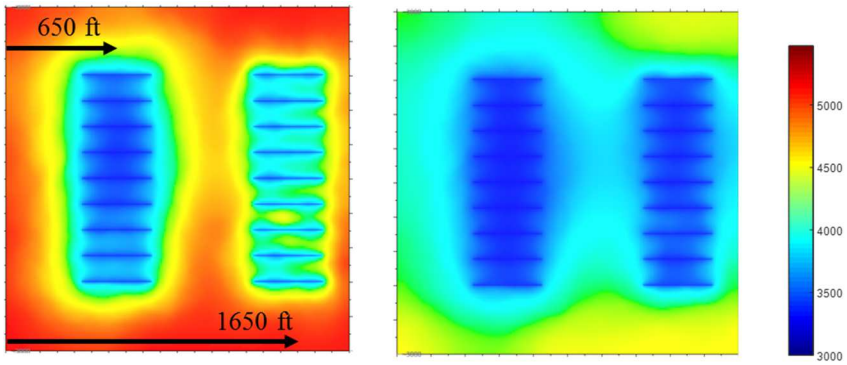


**(a) 3 years** **(b) 30 years**

**Figure 4.25 Pressure distribution at 3 years and 30 years with optimized well location for long term**

Figure 4.26 plots the cumulative production of individual well and combined wells in both short term and long term optimized locations. Red curves are the result from 3 years optimization and it shows the two wells give very close results since they are both in high permeability zone. Blue curves are the result from 30 years optimization and it shows that the well in high permeability zone has very good performance because of no

interference. The total production in Figure 4.26 (b) indicates that it is not always a good idea to put all wells in high permeability zone considering the long term production.

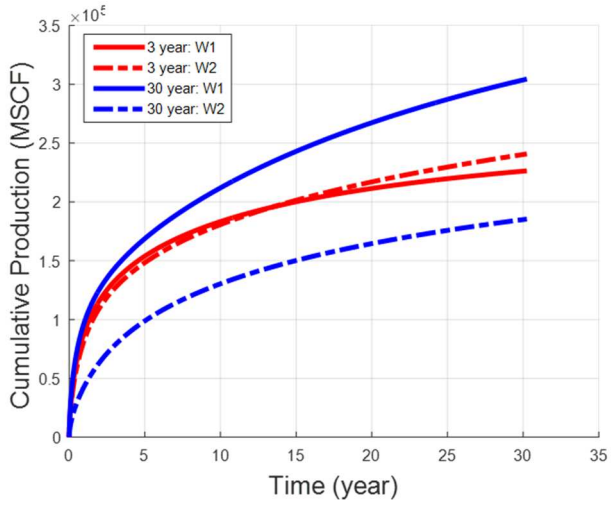


**(a) Individual well performance**

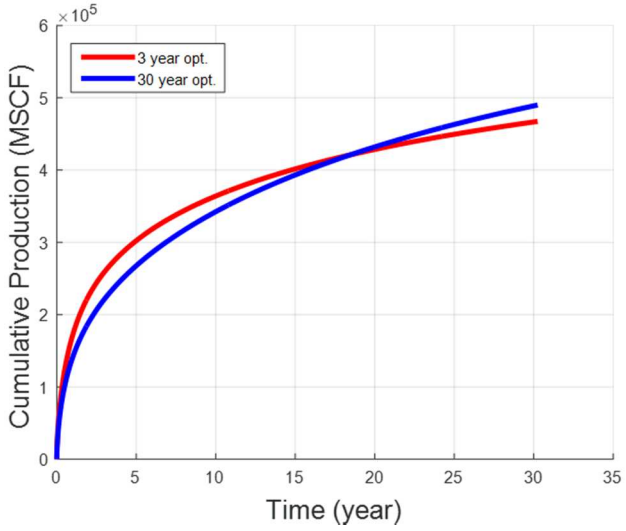


**(b) Field production**

**Figure 4.26 Comparison of cumulative production under different optimized locations**

## 4.4 Summary

In this chapter, we first proposed an approach to incorporate the additional arrival time of pressure front from boundary reflection into existing FMM 1-D equation to correct the pressure solution when boundary effect appears. Then we proposed a new drainage volume partition method based on asymptotic pressure solution by modifying the fast marching method and validated it against the streamline method. Last, we combined them together to predict the well performance and rapidly optimize the well spacing for multi-well interference problems. The benefits of the proposed approach were demonstrated with synthetic examples of unconventional reservoir. The main findings are summarized as follows:

1. Considering additional pressure front arrivals with superposition principle can improve the well performance and pressure contour when boundary effect dominates. The required number of arrivals is depends on the total simulation time, but for most scenario one additional reflection is adequate for the accuracy.

2. Multi-well interference problem can be partitioned based on the criterion of local maximum pressure directional derivative, which is analytically given by asymptotic pressure approximation. This criterion is equivalent to flux based partition in streamline method. Our results show reasonable approximation to the conventional flux-based partition method.

3. Based on above improvement, the proposed FMM workflow provides an intuitive way to characterize potential well interference and fracture connectivity in the reservoir,

as well as a rapid prescreening method for well spacing optimization with tremendous computational efficiency compared to traditional finite-difference simulation.

# CHAPTER V

# CONCLUSIONS AND RECOMMENDATIONS

## 5.1 Conclusions

In this dissertation, we have presented the applications of geomechanical model and Fast Marching Method in the field of hydraulic fracture propagation, refracturing and fracture/well performance that are recently emerging in unconventional reservoirs.

First, we adopted a coupled fracture propagation and reservoir flow model to understand the critical factors that affect the performance of refracturing operation. The depletion-induced stress can be accurately captured so that subsequently generated fracture geometry strongly is observed to highly depend on the refracturing time and location.

Second, we developed an integrated workflow that incorporates fracture propagation, reservoir flow and wellbore hydraulics to evaluate the efficiency of limited entry perforation during multiple simultaneous fracture propagation. The potential inefficiency of perforation layout has been investigated and sensitivity analysis has been performed.

Last, we presented a novel method to incorporate the additional arrival time of pressure front from boundary reflection into existing FMM 1-D equation to extend its applications into boundary-dominated flow regime. We then proposed a new drainage volume partition method based on asymptotic pressure solution by modifying the fast marching method, which is further validated against the conventional streamline method.

The main findings in this work are summarized below:

1. It has been numerically proved that refracturing is more likely to create wider but shorter fractures in the depleted reservoir compared to the virgin reservoir. Therefore, refracturing existing perforations is an effective way to restore the deteriorated fracture conductivity while refracturing new perforations is generally used to stimulate new rock and create more surface contact area with the reservoir. The selection of appropriate refracturing strategy relies on the accurate identification of mechanisms that induce the production decline. Generally, refracturing new perforations shows better short-term performance than refracturing existing perforations but may give worse long-term performance, depending on how much the proppants will degrade.
2. Stress shadowing effect has been proved to be one major reason for perforation inefficiency and non-uniform fracture development during multiple fractures simultaneous propagation within a single stage. The perforation frictions are demonstrated to be effective approach to counteract the additional flow resistance in neighboring fractures exerted by stress shadowing. Therefore, the limited entry perforations that uses deliberate deployment of number of perforation shots and clusters within a single stage can mitigate the influence and thus promote more uniform fracture development to improve the ultimate well performance
3. In FMM pressure calculation, the proposed method that considers additional pressure front arrivals, along with superposition principle, can effectively improve

the well performance and pressure contour when it enters into the boundary-dominated flow regime.

4. A criterion based on local maximum pressure directional derivative, which can be analytically acquired by asymptotic pressure approximation, is proposed to partition the drainage volume in multi-well interference problem. This criterion is equivalent to flux based partition in streamline method, where new formulation enables the calculation of corresponding drainage volume during the marching process of pressure wavefront. The new formulation has been benchmarked with streamline method by using various test cases. Due to the overwhelming numerical efficiency, it can serve as a rapid prescreening method for well spacing optimization problems.

## 5.2 Recommendations

Although the methods and workflow proposed can provide insightful results and guidance for emerging challenges in the development of unconventional resources, there is still large room for improvement when applied to complex reservoir conditions. The following are the recommendations for possible further work:

1. In order to better understand the hydraulic fracture geometry in the complex layered formation, a fully 3D model needs to be adopted to study the fracture propagation in both height and length directions. The pressure response from 2D model can only simulate fracturing behavior in one direction and thus is biased, whereas the pressure response from 3D model can capture the full signatures of

critical stages during fracture propagation in two directions. The accurate prediction of pressure response could be very helpful for the fracture model calibration. The major challenge for 3D model is the tremendous computational cost, especially for a reservoir-scale model. A sector model may allow detailed simulation studies to be performed while keeping running time at an acceptable level.

2. A non-planar model needs to be adopted to simulate the fracture geometry under strong stress shadow effect. The current simulation results based on the planar CZM model ignore the potential fracture bending behavior during both initial fracturing and subsequent refracturing. The potential stress reorientation could not only affect the fracture length but also the propagation direction, which could significantly impact the eventual well performance. A XFEM-based non-planar model can be used to study the fracture geometry under these circumstances.
3. A workflow to integrate the simulated fracture geometry into FMM simulator could take advantage of the speed superiority and multi-continuum multi-component capabilities of FMM in modeling the production in fractured unconventional reservoirs. The accurate prediction of pressure depletion, especially near producing fractures, could benefit the subsequent refracturing simulation in geomechanical model.
4. A more rigorous formulation in pressure front competition under FMM framework is desired to accurately describe the production interference between producing

fractures/wells. It is expected to be not only efficient and also robust under the complex operating conditions.

# NOMENCLATURE

| | | |
|---|---|---|
| $\alpha$ | = | Hydraulic diffusivity coefficient |
| $c_t$ | = | Total compressibility |
| $C_L$ | = | Leakoff coefficient |
| $D$ | = | Wellbore diameter |
| $C_D$ | = | Dimensionless discharge coefficient |
| $f_D$ | = | Darcy friction factor |
| $G_n^c$ | = | Critical fracture energy in mode I |
| $G_s^c$ | = | Critical fracture energy in mode II |
| $k$ | = | Reservoir permeability |
| $k_t$ | = | Tangential resistance to fracture fluid flow |
| $K$ | = | Fluid consistency |
| $p$ | = | Reservoir pressure |
| $p_f$ | = | Fracture pressure |
| $\Delta p$ | = | Reservoir pressure drop |
| $\Delta p_{wb}$ | = | Wellbore pressure drop |
| $\Delta p_{perf}$ | = | Perforation pressure drop |
| $\Delta p_{hydro}$ | = | Hydrostatic pressure drop |
| $q$ | = | Darcy flux |
| $Q$ | = | Total volumetric rate |

| | | |
|---|---|---|
| $r$ | = | Radius |
| $t$ | = | Time |
| $t_n$ | = | Normal component of stress |
| $t_s$ | = | First shear component of stress |
| $t_t$ | = | Second shear component of stress |
| $\tau$ | = | Diffusive time of flight |
| $S$ | = | Slowness |
| $\sigma$ | = | Total stress |
| $\sigma'$ | = | Effective stress |
| $\varepsilon$ | = | Strain |
| $\rho$ | = | Fluid density |
| $\phi$ | = | Porosity |
| $\mu$ | = | Fluid viscosity |
| $w_f$ | = | Fracture width |
| DV | = | Drainage volume |
| FMM | = | Fast Marching Method |
| $\langle \cdot \rangle$ | = | Macaulay brackets |

# REFERENCES


Alramahi, B. and Sundberg, M.I. 2012. Proppant Embedment and Conductivity of Hydraulic Fractures in Shales. Paper presented at the 46th U.S. Rock Mechanics/Geomechanics Symposium, Chicago, Illinois. American Rock Mechanics Association ARMA-2012-291.

Barree, R.D., Cox, S.A., Barree, V.L. et al. 2003. Realistic Assessment of Proppant Pack Conductivity for Material Selection. Society of Petroleum Engineers. DOI: 10.2118/84306-MS.

Barree, R.D., Miskimins, J.L., Conway, M.W. et al. 2016. Generic Correlations for Proppant Pack Conductivity. Society of Petroleum Engineers. DOI: 10.2118/179135-MS.

Barree, R.D., Miskimins, J.L., and Svatek, K.J. 2017. Reservoir and Completion Considerations for the Refracturing of Horizontal Wells. Paper presented at the SPE Hydraulic Fracturing Technology Conference and Exhibition, The Woodlands, Texas, USA. Society of Petroleum Engineers SPE-184837-MS. DOI: 10.2118/184837-MS.

Bear, J. 1972. *Dynamics of Fluids in Porous Media*: Mineola, NY: Dover. Original edition. ISBN 0486656756.

Benzeggagh, M.L. and Kenane, M. 1996. Measurement of Mixed-Mode Delamination Fracture Toughness of Unidirectional Glass/Epoxy Composites with Mixed-Mode Bending Apparatus. *Composites Science and Technology* **56** (4): 439-449. DOI: http://dx.doi.org/10.1016/0266-3538(96)00005-X

Blasingame, T.A. and Rushing, J.A. 2005. A Production-Based Method for Direct Estimation of Gas in Place and Reserves. Paper presented at the SPE Eastern Regional Meeting, Morgantown, West Virginia. Society of Petroleum Engineers SPE-98042-MS. DOI: 10.2118/98042-MS.

Bunger, A., Jeffrey, R.G., and Zhang, X. 2014. Constraints on Simultaneous Growth of Hydraulic Fractures from Multiple Perforation Clusters in Horizontal Wells. *SPE Journal* **19** (04). DOI: 10.2118/163860-PA

Bunger, A.P. and Peirce, A.P. 2014. Numerical Simulation of Simultaneous Growth of Multiple Interacting Hydraulic Fractures from Horizontal Wells. Paper presented at the Shale Energy Engineering 2014.

Bunger, A.P., Zhang, X., and Jeffrey, R.G. 2012. Parameters Affecting the Interaction among Closely Spaced Hydraulic Fractures. *SPE Journal* **17** (1). DOI: 10.2118/140426-PA

Cheng, C., Bunger, A.P., and Peirce, A.P. 2016. Optimal Perforation Location and Limited Entry Design for Promoting Simultaneous Growth of Multiple Hydraulic Fractures. Paper presented at the SPE Hydraulic Fracturing Technology Conference, The Woodlands, Texas, USA. Society of Petroleum Engineers SPE-179158-MS. DOI: 10.2118/179158-MS.

Cipolla, C.L., Lolon, E.P., Erdle, J.C. et al. 2010. Reservoir Modeling in Shale-Gas Reservoirs. *SPE Reservoir Evaluation & Engineering* **13** (4). DOI: 10.2118/125530-PA

Coulter, G.R., Benton, E.G., and Thomson, C.L. 2004. Water Fracs and Sand Quantity: A Barnett Shale Example. Paper presented at the SPE Annual Technical Conference and Exhibition, Houston, Texas. Society of Petroleum Engineers SPE-90891-MS. DOI: 10.2118/90891-MS.

Coulter, G.R. and Wells, R.D. 1972. The Advantages of High Proppant Concentration in Fracture Stimulation. *Journal of Petroleum Technology* **24** (6). DOI: 10.2118/3298-PA

Cox, D.O., Kuuskraa, V.A., and Hansen, J.T. 1996. Advanced Type Curve Analysis for Low Permeability Gas Reservoirs. Paper presented at the SPE Gas Technology Symposium, Calgary, Alberta, Canada. Society of Petroleum Engineers. DOI: 10.2118/35595-MS.

Craig, M.S., Wendte, S.S., and Buchwalter, J.L. 2012. Barnett Shale Horizontal Restimulations: A Case Study of 13 Wells. Paper presented at the SPE Americas Unconventional Resources Conference, Pittsburgh, Pennsylvania. Society of Petroleum Engineers SPE-154669-MS. DOI: 10.2118/154669-MS.

Cramer, D.D. 1987. The Application of Limited-Entry Techniques in Massive Hydraulic Fracturing Treatments. Paper presented at the SPE Production Operations Symposium, Oklahoma City, Oklahoma. Society of Petroleum Engineers SPE-16189-MS. DOI: 10.2118/16189-MS.

Dahi-Taleghani, A. and Olson, J.E. 2011. Numerical Modeling of Multistranded-Hydraulic-Fracture Propagation: Accounting for the Interaction between Induced and Natural Fractures. *SPE Journal* **16** (3). DOI: 10.2118/124884-PA

Dahl, J., Dhuldhoya, K., Vaidya, R. et al. 2016. An Evaluation of Completion Effectiveness in Hydraulically Fractured Wells and the Assessment of Refracturing Scenarios. Paper presented at the SPE Hydraulic Fracturing Technology Conference, The Woodlands, Texas, USA. Society of Petroleum Engineers SPE-179136-MS. DOI: 10.2118/179136-MS.

Daneshy, A.A. 2015. Dynamic Interaction within Multiple Limited Entry Fractures in Horizontal Wells: Theory, Implications, and Field Verification. Paper presented at the SPE Hydraulic Fracturing Technology Conference, The Woodlands, Texas, USA. Society of Petroleum Engineers SPE-173344-MS. DOI: 10.2118/173344-MS.

Datta-Gupta, A. and King, M.J. 2007. *Streamline Simulation: Theory and Practice*. Spe Textbook Series: Society of Petroleum Engineers. Original edition. ISBN 978-1-55563-111-6.

Datta-Gupta, A., King, M.J., and Society of Petroleum, E. 2007. Streamline Simulation : Theory and Practice. In. Richardson, TX :: Society of Petroleum Engineers. 1613991649 9781613991640

Datta-Gupta, A., Xie, J., Gupta, N. et al. 2011. Radius of Investigation and Its Generalization to Unconventional Reservoirs. *Journal of Petroleum Technology* **63** (7). DOI: 10.2118/0711-0052-JPT

Economides, M.J. and Nolte, K. 2000. *Reservoir Stimulation, 3rd Edition*. Chichester, UK: John Wiley & Sons. Original edition. ISBN 0471491926.

Fetkovich, M.J. 1980. Enlarged Type Curves Supporting. *Journal of Petroleum Technology* (June 1980).

French, S., Rodgerson, J., and Feik, C. 2014. Re-Fracturing Horizontal Shale Wells: Case History of a Woodford Shale Pilot Project. Paper presented at the SPE Hydraulic Fracturing Technology Conference, The Woodlands, Texas, USA. Society of Petroleum Engineers SPE-168607-MS. DOI: 10.2118/168607-MS.

Fujita, Y. 2014. Fast Marching Method with Multiphase Flow and Compositional Effects. Master Thesis, Texas A&M University.

Fujita, Y., Datta-Gupta, A., and King, M.J. 2015. A Comprehensive Reservoir Simulator for Unconventional Reservoirs Based on the Fast Marching Method and Diffusive Time of Flight. Paper presented at the SPE Reservoir Simulation Symposium, Houston, Texas, USA. Society of Petroleum Engineers SPE-173269-MS. DOI: 10.2118/173269-MS.

Geertsma, J. and De Klerk, F. 1969. A Rapid Method of Predicting Width and Extent of Hydraulically Induced Fractures. *Journal of Petroleum Technology* **21** (12). DOI: 10.2118/2458-PA

Ghassemi, A. 2016. Impact of Fracture Interactions, Rock Anisotropy and Heterogeneity on Hydraulic Fracturing: Some Insights from Numerical Simulations. Paper presented at the 50th U.S. Rock Mechanics/Geomechanics Symposium, Houston, Texas.

Glover, K., Naser, G., and Mohammadi, H. 2015. Creep Deformation of Fracture Surfaces Analysis in a Hydraulically Fractured Reservoir Using the Finite Element Method. *Journal of Petroleum and Gas Engineering* **6** (6): 62-73.

Grieser, B., Calvin, J., and Dulin, J. 2016. Lessons Learned: Refracs from 1980 to Present. Paper presented at the SPE Hydraulic Fracturing Technology Conference, The Woodlands, Texas, USA. Society of Petroleum Engineers SPE-179152-MS. DOI: 10.2118/179152-MS.

Guo, J. and Liu, Y. 2012. Modeling of Proppant Embedment: Elastic Deformation and Creep Deformation. Paper presented at the SPE International Production and Operations Conference & Exhibition, Doha, Qatar. Society of Petroleum Engineers SPE-157449-MS. DOI: 10.2118/157449-MS.

Haddad, M., Sanaei, A., Al-Shalabi, E.W. et al. 2015. Major Obstacles in Production from Hydraulically Re-Fractured Shale Formations: Reservoir Pressure Depletion and Pore Blockage by the Fracturing Fluid. Paper presented at the Unconventional Resources Technology Conferenc, San Antonio, Texas, USA. Society of Petroleum Engineers SPE-178587-MS. DOI: 10.2118/178587-MS.

Haddad, M. and Sepehrnoori, K. 2014. Simulation of Multiple-Stage Fracturing in Quasibrittle Shale Formations Using Pore Pressure Cohesive Zone Model. Paper presented at the Unconventional Resources Technology Conference, Denver, Colorado. Society of Petroleum Engineers. DOI: 10.15530/urtec-2014-1922219.

Harris, P.C. and Pippin, P.M. 2000. High-Rate Foam Fracturing: Fluid Friction and Perforation Erosion. *SPE Production & Facilities* **15** (01). DOI: 10.2118/60841-PA

Hassouna, M.S. and Farag, A.A. 2007. Multistencils Fast Marching Methods: A Highly Accurate Solution to the Eikonal Equation on Cartesian Domains. *IEEE Transactions on Pattern Analysis and Machine Intelligence* **29** (9): 1563-1574. DOI: 10.1109/TPAMI.2007.1154

He, J., Killough, J.E., Fadlelmula F, M.M. et al. 2015. A Unified Finite Difference Model for the Simulation of Transient Flow in Naturally Fractured Carbonate Karst Reservoirs. Paper presented at the SPE Annual Technical Conference and Exhibition, Houston, Texas, USA. Society of Petroleum Engineers PE-175098-MS. DOI: 10.2118/173262-MS.

He, Z., Parikh, H., Datta-Gupta, A. et al. 2002. Identifying Reservoir Compartmentalization and Flow Barriers Using Primary Production: A Streamline Approach. Paper presented at the SPE Annual Technical Conference and Exhibition, San Antonio, Texas. Society of Petroleum Engineers SPE-77589-MS. DOI: 10.2118/77589-MS.

Holditch, S.A. 2010. Shale Gas Holds Global Opportunities. *The American Oil & Gas Reporter*.

Huang, J., Safari, R., Lakshminarayanan, S. et al. 2014. Impact of Discrete Fracture Network (Dfn) Reactivation on Productive Stimulated Rock Volume: Microseismic, Geomechanics and Reservoir Coupling. Paper presented at the 48th U.S. Rock Mechanics/Geomechanics Symposium, Minneapolis, Minnesota. American Rock Mechanics Association ARMA-2014-7017.

Ingram, S.R., Lahman, M., and Persac, S. 2014. Methods Improve Stimulation Efficiency of Perforation Clusters in Completions. *Journal of Petroleum Technology* **66** (04). DOI: 10.2118/0414-0032-JPT

Jayakumar, R., Rai, R., Boulis, A. et al. 2013. A Systematic Study for Refracturing Modeling under Different Scenarios in Shale Reservoirs. Society of Petroleum Engineers. DOI: 10.2118/165677-MS.

Jeffrey, R.G., Chen, Z., Mills, K.W. et al. 2013. *Monitoring and Measuring Hydraulic Fracturing Growth During Preconditioning of a Roof Rock over a Coal Longwall Panel*. Effective and Sustainable Hydraulic Fracturing Original edition. ISBN.

John Lee, J.B.R., John P. Spivey. 1982. *Well Testing*. Spe Textbook Series: Society of Petroleum Engineers. Original edition. ISBN 978-089520-317-5.

John Lee, J.B.R., John P. Spivey. 2003. *Pressure Transient Testing*. Spe Textbook Series: Society of Petroleum Engineers. Original edition. ISBN 978-1-55563-099-7.

Kang, S., Datta-Gupta, A., and John Lee, W. 2013. Impact of Natural Fractures in Drainage Volume Calculations and Optimal Well Placement in Tight Gas Reservoirs. *Journal of Petroleum Science and Engineering* **109**: 206-216. DOI: http://dx.doi.org/10.1016/j.petrol.2013.08.024

Kanninen, M.F. and Popelar, C.H. 1985. *Advanced Fracture Mechanics*. Oxford: Oxford University Press. Original edition. ISBN 0195035321.

Kassis, S.M. and Sondergeld, C.H. 2010. Gas Shale Permeability: Effects of Roughness, Proppant, Fracture Offset, and Confining Pressure. Paper presented at the International Oil and Gas Conference and Exhibition in China, Beijing, China. Society of Petroleum Engineers SPE-131376-MS. DOI: 10.2118/131376-MS.

Khristianovic, S.A. and Zheltov, Y.P. 1955. Formation of Vertical Fractures by Means of Highly Viscous Liquid. Paper presented at the 4th World Petroleum Congress, Rome, Italy. WPC-6132.

Kim, J.U. 2009. Production Data Integration into High Resolution Geologic Models with Trajectory-Based Methods and a Dual Scale Approach. PhD Dissertation, Texas A&M University.

Kim, J.U., Datta-Gupta, A., Brouwer, R. et al. 2009. Calibration of High-Resolution Reservoir Models Using Transient Pressure Data. Paper presented at the SPE Annual Technical Conference and Exhibition, New Orleans, Louisiana. Society of Petroleum Engineers SPE-124834-MS. DOI: 10.2118/124834-MS.

King, M.J., Wang, Z., and Datta-Gupta, A. 2016. Asymptotic Solutions of the Diffusivity Equation and Their Applications. Paper presented at the SPE Europec featured at 78th EAGE Conference and Exhibition, Vienna, Austria. Society of Petroleum Engineers SPE-180149-MS. DOI: 10.2118/180149-MS.

Kong, J. and Yuan, J. 2010. Application of Linear Viscoelastic Differential Constitutive Equation in Abaqus Paper presented at the International Conference On Computer Design And Appliations, Qinhuangdao. V5-152-156. IEEE. DOI: 10.1109/ICCDA.2010.5541456.

Kulkarni, K.N., Datta-Gupta, A., and Vasco, D.W. 2001. A Streamline Approach for Integrating Transient Pressure Data into High-Resolution Reservoir Models. *SPE Journal* **6** (03). DOI: 10.2118/74135-PA

Lagrone, K.W. and Rasmussen, J.W. 1963. A New Development in Completion Methods-the Limited Entry Technique. *Journal of Petroleum Technology* **15** (7). DOI: 10.2118/530-PA

Lecampion, B., Desroches, J., Weng, X. et al. 2015. Can We Engineer Better Multistage Horizontal Completions? Evidence of the Importance of near-Wellbore Fracture Geometry from Theory, Lab and Field Experiments. Paper presented at the SPE Hydraulic Fracturing Technology Conference, The Woodlands, Texas. Society of Petroleum Engineers SPE-173363-MS. DOI: 10.2118/173363-MS.

Lee, W.J. and Hopkins, C.W. 1994. Characterization of Tight Reservoirs. *Journal of Petroleum Technology*. DOI: 10.2118/29091-PA

Lelièvre, P.G., Farquharson, C.G., and Hurich, C.A. 2011. Computing First-Arrival Seismic Traveltimes on Unstructured 3-D Tetrahedral Grids Using the Fast Marching Method. *Geophysical Journal International* **184** (2): 885-896. DOI: 10.1111/j.1365-246X.2010.04880.x

Li, C. and King, M.J. 2016. Integration of Pressure Transient Data into Reservoir Models Using the Fast Marching Method. Paper presented at the SPE Europec featured at 78th EAGE Conference and Exhibition, Vienna, Austria. Society of Petroleum Engineers SPE-180148-MS. DOI: 10.2118/180148-MS.

Lord, D.L., Shah, S.N., Rein, R.G. et al. 1994. Study of Perforation Friction Pressure Employing a Large-Scale Fracturing Flow Simulator. Paper presented at the SPE Annual Technical Conference and Exhibition, New Orleans, Louisiana. Society of Petroleum Engineers SPE-28508-MS. DOI: 10.2118/28508-MS.

Malpani, R., Sinha, S., Charry, L. et al. 2015. Improving Hydrocarbon Recovery of Horizontal Shale Wells through Refracturing. Paper presented at the SPE/CSUR Unconventional Resources Conference, Calgary, Alberta, Canada. Society of Petroleum Engineers SPE-175920-MS. DOI: 10.2118/175920-MS.

Meyer, B.R., Bazan, L.W., Jacot, R.H. et al. 2010. Optimization of Multiple Transverse Hydraulic Fractures in Horizontal Wellbores. Paper presented at the SPE Unconventional Gas Conference, Pittsburgh, Pennsylvania, USA. Society of Petroleum Engineers SPE-131732-MS. DOI: 10.2118/131732-MS.

Miller, C.K., Waters, G.A., and Rylander, E.I. 2011. Evaluation of Production Log Data from Horizontal Wells Drilled in Organic Shales. Paper presented at the North American Unconventional Gas Conference and Exhibition, The Woodlands, Texas. Society of Petroleum Engineers SPE-144326-MS. DOI: 10.2118/144326-MS.

Molenaar, M.M., Hill, D., Webster, P. et al. 2012. First Downhole Application of Distributed Acoustic Sensing for Hydraulic-Fracturing Monitoring and Diagnostics. *SPE Drilling & Completion*. DOI: 10.2118/140561-PA

Nagel, N.B., Damjanac, B., Garcia, X. et al. 2011. Discrete Element Hydraulic Fracturing Modeling: Evaluating Changes in Fracture Transmissivity. Paper presented at the Canadian Unconventional Resources Conference, Calgary, Alberta, Canada. Society of Petroleum Engineers SPE-148957-MS. DOI: 10.2118/148957-MS.

Nordgren, R.P. 1972. Propagation of a Vertical Hydraulic Fracture. *Society of Petroleum Engineers Journal* **12** (4). DOI: 10.2118/3009-PA

Oberhofer, R. 2016. Application of Ball-Drop Technology to Improve Efficiency and Stimulation of Limited Entry Completion Systems. Paper presented at the Abu Dhabi International Petroleum Exhibition & Conference, Abu Dhabi, UAE. Society of Petroleum Engineers SPE-183427-MS. DOI: 10.2118/183427-MS.

Oliver, D. 1994. Application of a Wave Transform to Pressure Transient Testing in Porous Media. *Transport in Porous Media* **16** (3): 209-236. DOI: 10.1007/BF00617148

Peirce, A. and Bunger, A. 2015. Interference Fracturing: Nonuniform Distributions of Perforation Clusters That Promote Simultaneous Growth of Multiple Hydraulic Fractures. *SPE Journal* **20** (2). DOI: 10.2118/172500-PA

Perkins, T.K. and Kern, L.R. 1961. Widths of Hydraulic Fractures. *Journal of Petroleum Technology* **13** (9). DOI: 10.2118/89-PA

Qian, J., Zhang, Y., and Zhao, H. 2007. Fast Sweeping Methods for Eikonal Equations on Triangular Meshes. *SIAM Journal on Numerical Analysis* **45** (1): 83-107. DOI: 10.1137/050627083

Romero, J., Mack, M.G., and Elbel, J.L. 1995. Theoretical Model and Numerical Investigation of near-Wellbore Effects in Hydraulic Fracturing. Paper presented at the SPE Annual Technical Conference and Exhibition, Dallas, Texas. Society of Petroleum Engineers SPE-30506-MS. DOI: 10.2118/30506-MS.

Roussel, N.P. and Sharma, M.M. 2011. Optimizing Fracture Spacing and Sequencing in Horizontal-Well Fracturing. *SPE Production & Operation*. DOI: 10.2118/127986-PA

Rushing, J.A., Perego, A.D., and Blasingame, T.A. 2008. Applicability of the Arps Rate-Time Relationships for Evaluating Decline Behavior and Ultimate Gas Recovery of Coalbed Methane Wells. Paper presented at the CIPC/SPE Gas Technology Symposium, Calgary, Alberta, Canada. Society of Petroleum Engineers SPE-114514-MS. DOI: 10.2118/114514-MS.

Sesetty, V. and Ghassemi, A. 2015. Simulation of Simultaneous and Zipper Fractures in Shale Formations. Paper presented at the 49th U.S. Rock Mechanics/Geomechanics Symposium, San Francisco, California. American Rock Mechanics Association ARMA-2015-558.

Sethian, J. 1999. Fast Marching Methods. *SIAM Review* **41** (2): 199-235. DOI: 10.1137/S0036144598347059

Sethian, J.A. 1996. A Fast Marching Level Set Method for Monotonically Advancing Fronts. *Proceedings of the National Academy of Sciences of the United States of America* **93** (4): 1591-1595.

Shin, D.H. and Sharma, M.M. 2014. Factors Controlling the Simultaneous Propagation of Multiple Competing Fractures in a Horizontal Well. Paper presented at the SPE Hydraulic Fracturing Technology Conference, The Woodlands, Texas. Society of Petroleum Engineers SPE-168599-MS. DOI: 10.2118/168599-MS.

Simulia. 2014. *Abaqus User's Manual, Version 6.14*. Dassault Systèmes.

Sinha, S. and Ramakrishnan, H. 2011. A Novel Screening Method for Selection of Horizontal Refracturing Candidates in Shale Gas Reservoirs. Paper presented at the North American Unconventional Gas Conference and Exhibition, The Woodlands, Texas, USA. Society of Petroleum Engineers SPE-144032-MS. DOI: 10.2118/144032-MS.

Skomorowski, N., Dussealut, M.B., and Gracie, R. 2015. The Use of Multistage Hydraulic Fracture Data to Identify Stress Shadow Effects. Paper presented at the 49th U.S. Rock Mechanics/Geomechanics Symposium,, San Francisco, California. American Rock Mechanics Association ARMA-2015-624.

Sone, H. and Zoback, M.D. 2010. Strength, Creep and Frictional Properties of Gas Shale Reservoir Rocks. Paper presented at the 44th U.S. Rock Mechanics Symposium and 5th U.S.-Canada Rock Mechanics Symposium, Salt Lake City, Utah. American Rock Mechanics Association ARMA-10-463.

Tavassoli, S., Yu, W., Javadpour, F. et al. 2013. Selection of Candidate Horizontal Wells and Determination of the Optimal Time of Refracturing in Barnett Shale (Johnson County). Paper presented at the SPE Unconventional Resources Conference Canada, Calgary, Alberta, Canada. Society of Petroleum Engineers SPE-167137-MS. DOI: 10.2118/167137-MS.

Terracina, J.M., Turner, J.M., Collins, D.H. et al. 2010. Proppant Selection and Its Effect on the Results of Fracturing Treatments Performed in Shale Formations. Paper presented at the SPE Annual Technical Conference and Exhibition, Florence, Italy. Society of Petroleum Engineers SPE-135502-MS. DOI: 10.2118/135502-MS.

Turon, A., Camanho, P.P., Costa, J. et al. 2006. A Damage Model for the Simulation of Delamination in Advanced Composites under Variable-Mode Loading. *Mechanics of Materials* **38** (11): 1072-1089. DOI: http://dx.doi.org/10.1016/j.mechmat.2005.10.003

Ugueto C, G.A., Huckabee, P.T., Molenaar, M.M. et al. 2016. Perforation Cluster Efficiency of Cemented Plug and Perf Limited Entry Completions; Insights from Fiber Optics Diagnostics. Paper presented at the SPE Hydraulic Fracturing Technology Conference, The Woodlands, Texas, USA. Society of Petroleum Engineers SPE-179124-MS. DOI: 10.2118/179124-MS.

Valko, P. and Economides, M.J. 1995. *Hydraulic Fracture Mechanics*: John Wiley & Sons Ltd, Baffins Lane, Chichester, West Sussex PO19 IUD, England. Original edition. ISBN 0471956643.

Vasco, D.W., Keers, H., and Karasaki, K. 2000. Estimation of Reservoir Properties Using Transient Pressure Data: An Asymptotic Approach. *Water Resources Research* **36** (12): 3447-3465. DOI: 10.1029/2000WR900179

Vincent, M. 2011. Restimulation of Unconventional Reservoirs: When Are Refracs Beneficial? *Journal of Canadian Petroleum Technology* **50** (5). DOI: 10.2118/136757-PA

Vincent, M.C. 2010. Refracs: Why Do They Work, and Why Do They Fail in 100 Published Field Studies? Paper presented at the SPE Annual Technical Conference

and Exhibition, Florence, Italy. Society of Petroleum Engineers SPE-134330-MS. DOI: 10.2118/134330-MS.

Wang, H., Marongiu-Porcu, M., and Economides, M.J. 2016. Poroelastic and Poroplastic Modeling of Hydraulic Fracturing in Brittle and Ductile Formations. DOI: 10.2118/168600-PA

Warpinski, N.R. and Branagan, P.T. 1989. Altered-Stress Fracturing. *Journal of Petroleum Technology* **41** (9). DOI: 10.2118/17533-PA

Weaver, J.D., Raysoni, N.D., and Lubis, W. 2014. Determining Conductivity of Aged Fracture Proppants for Simulating Flow in a Fractured Reservoir. In: Google Patents.

Wu, K., Olson, J., Balhoff, M.T. et al. 2015. Numerical Analysis for Promoting Uniform Development of Simultaneous Multiple Fracture Propagation in Horizontal Wells. Paper presented at the SPE Annual Technical Conference and Exhibition, Houston, Texas, USA. Society of Petroleum Engineers SPE-174869-MS. DOI: 10.2118/174869-MS.

Wu, K., Olson, J., Balhoff, M.T. et al. 2016. Numerical Analysis for Promoting Uniform Development of Simultaneous Multiple-Fracture Propagation in Horizontal Wells. *SPE Production & Operations*. DOI: 10.2118/174869-PA

Wu, K. and Olson, J.E. 2013. Investigation of Critical in Situ and Injection Factors in Multi-Frac Treatments: Guidelines for Controlling Fracture Complexity. Paper presented at the SPE Hydraulic Fracturing Technology Conference, The Woodlands, Texas. Society of Petroleum Engineers. DOI: 10.2118/163821-MS.

Wu, K. and Olson, J.E. 2015. Simultaneous Multifracture Treatments: Fully Coupled Fluid Flow and Fracture Mechanics for Horizontal Wells. *SPE Journal* **20** (02). DOI: 10.2118/167626-PA

Xie, J. 2012. Applications of Level Set and Fast Marching Methods in Reservoir Characterization. PhD Dissertation, Texas A&M University.

Xie, J., Gupta, N., King, M.J. et al. 2012. Depth of Investigation and Depletion Behavior in Unconventional Reservoirs Using Fast Marching Methods. Paper presented at the SPE Europec/EAGE Annual Conference, Copenhagen, Denmark. Society of Petroleum Engineers SPE-154532-MS. DOI: 10.2118/154532-MS.

Yang, T.H., Tham, L.G., Tang, C.A. et al. 2004. Influence of Heterogeneity of Mechanical Properties on Hydraulic Fracturing in Permeable Rocks. *Rock Mechanics and Rock Engineering* **37** (4): 251-275. DOI: 10.1007/s00603-003-0022-z

Yao, Y., Gosavi, S.V., Searles, K.H. et al. 2010. Cohesive Fracture Mechanics Based Analysis to Model Ductile Rock Fracture. Paper presented at the 44th US Rock Mechanics Symposium, Salt Lake City, UT. American Rock Mechanics Association ARMA 10-140.

Zhang, Y. 2013. Dynamic Reservoir Characterization Using Complex Grids Based on Streamline and Fast Marching Methods. Ph.D. Dissertation, Texas A&M University.

Zhang, Y., Bansal, N., Fujita, Y. et al. 2016. From Streamlines to Fast Marching: Rapid Simulation and Performance Assessment of Shale-Gas Reservoirs by Use of Diffusive Time of Flight as a Spatial Coordinate. *SPE Journal* **21** (5). DOI: 10.2118/168997-PA

Zhang, Y., Yang, C., King, M.J. et al. 2013. Fast-Marching Methods for Complex Grids and Anisotropic Permeabilities: Application to Unconventional Reservoirs. Paper presented at the SPE Reservoir Simulation Symposium, The Woodlands, Texas. Society of Petroleum Engineers SPE-163637-MS. DOI: 10.2118/163637-MS.

Zhou, J., Huang, H., and Deo, M. 2016a. Numerical Study of Critical Role of Rock Heterogeneity in Hydraulic Fracture Propagation. Paper presented at the 50th U.S. Rock Mechanics/Geomechanics Symposium, Houston, Texas. American Rock Mechanics Association ARMA-2016-682.

Zhou, J., Huang, H., and Deo, M. 2016b. Simulation of Hydraulic and Natural Fracture Interaction Using a Coupled Dfn-Dem Model. Paper presented at the 50th U.S. Rock Mechanics/Geomechanics Symposium, Houston, Texas. American Rock Mechanics Association ARMA-2016-739.

Zhou, J., Huang, H., Deo, M. et al. 2015. A New Physics-Based Modeling of Multiple Non-Planar Hydraulic Fractures Propagation. Paper presented at the Unconventional Resources Technology Conference, San Antonio, Texas. Society of Petroleum Engineers SPE-178664-MS. DOI: 10.2118/178664-MS.

Zielonka, M.G., Searles, K.H., Ning, J. et al. 2014. Development and Validation of Fully-Coupled Hydraulic Fracturing Simulation Capabilities. Paper presented at the 2014 SIMULIA Community Conference.

# APPENDIX A

## A NEW METHOD FOR TRACING PRESSURE FRONT TRAJECTORY

The trajectory-based methods have been widely used in both geophysical and flow modeling. Due to the favorable efficiency and scalability, this approach is extremely useful in dealing with large data sets and high resolution models. The visual and intuitive nature of the methods enable them to interpret the observations and facilitate the subsurface management. The rapid turn-around time for an inversion also means that the techniques are appropriate for time-lapse monitoring.

Similar to streamline method in convective problems, the trajectory in diffusive problems can also provide insight into the understanding of high-frequency wave-like behavior through intuitive visualization of propagating disturbances. Moreover, the separation of time and amplitude in a solution defined along a trajectory can offer more simplicity and flexibility, particularly in the treatment of the inverse problem.

The diffusive nature of pressure has unique advantages in geologic calibration problems: 1) pressure transient test is easier and less expensive to acquire; 2) pressure front travels much faster than tracer or water front, which means that pressure responses can be obtained at very early stage of production. However, the computational cost and localized nature of pressure sensitivities are challenge in transient pressure data history matching using conventional finite difference model. Moreover, pressure tests from multiple wells are difficult to analyze due to superposition of pressure responses. Thus, the trajectory-based method offers an alternative way to analytically calculate the pressure

sensitivity with respect to reservoir properties, working as an efficient approach to integrate pressure data into geologic models. This section will propose a new method to improve the tracing results of pressure front trajectory.

### A.1 Review of Pressure Front Trajectory

One important aspect of the asymptotic method is that the solution can be defined along the one-dimension trajectory. Vasco et al. (2000) showed a detailed derivation about the pressure front trajectory $\psi$, which can be computed by integrating the differential equation

$$\frac{d\psi}{d\zeta} = \nabla \tau(x) \tag{A.1}$$

and the diffusive time of flight for the propagation of a pressure front can be given by an integral along the trajectory (Kulkarni et al. 2001),

$$\tau(x) = \int_{\psi} \frac{d\zeta}{\sqrt{\alpha(x)}} \tag{A.2}$$

where the term $\zeta$ indicates the distance along the trajectory $\psi$ and the unit of diffusive time of flight is the square root of time which is consistent with the scaling behavior of diffusive flow.

To trace the pressure front trajectory in Eq. (A.1), the gradient of diffusive time of flight, $\nabla \tau$, can be obtained from the solution of Eikonal equation. Note that the pressure front trajectories are defined for fully transient flow, different from streamlines that are associated with quasi-steady state flow (Datta-Gupta et al. 2007). In other words, the pressure front trajectories are time-independent and depends only on the static properties

of reservoir such as permeability, porosity and compressibility. In contrast, during the transient state, streamlines are generally dynamic and time-dependent.

Figure A.1 shows the diffusive time of flight contour along with the pressure front trajectories (diffusive) in a heterogeneous permeability field. The source is placed at the lower left corner. A comparison with streamlines (convective trajectories) is also plotted to illustrate the difference. To be a fair comparison, the prescribed pressure boundary condition is placed on the top and right boundaries in the streamline simulation to avoid boundary effect on streamline trajectories. The difference between these trajectories are very clear from this picture. Unlike the streamlines trajectories that correspond to velocity field and represent the flow paths of a passive tracer, pressure front trajectories depict the propagation of a pressure disturbance. Analogous to the convective time of flight, we define ‘diffusive time of flight’ along the pressure front trajectories. Both convective and diffusive time of flight constitute very useful to characterize the flow and transport processes in heterogeneous porous media.

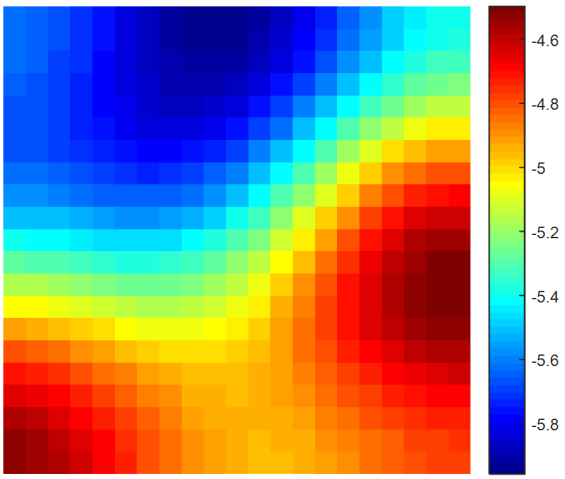


**(a)**

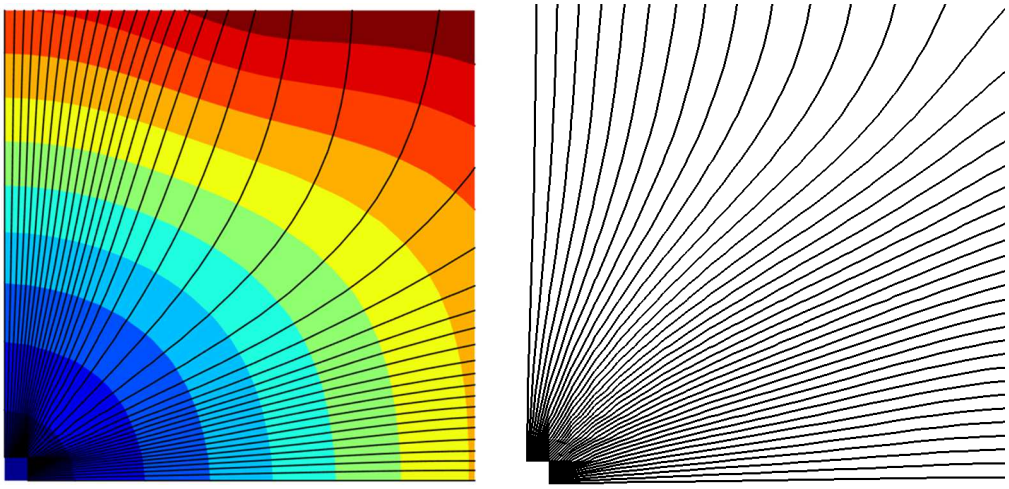

**(b)** **(c)**

**Figure A.1 Trajectories for a heterogeneous permeability (a) Permeability field (b) Diffusive time of flight and its trajectories (c) Streamlines**

## A.2 A New Method of Pressure Front Trajectory

Previous methods used for tracing pressure front trajectory have certain limitations when applied to complex field. We will propose a new method to remedy these drawbacks.

First, to trace pressure front trajectory, previous methods are all based on Eq. (A.1), however, this equation is not enough in complex fields such as that with property anisotropy. Let us revisit our Eikonal equation in more general form

$$\nabla\tau\cdot\overrightarrow{\overrightarrow{\alpha}}\cdot\nabla\tau=1 \tag{A.3}$$

A closer look at this equation shows that it has a form similar to that of the streamline time of flight equation which describes the propagation of a neutral tracer (Datta-Gupta and King 2007)

$$v\cdot\nabla\hat{\tau}(x)=1 \tag{A.4}$$

where $\hat{\tau}(\mathbf{x})$ is the streamline time of flight and $v$ is the interstitial velocity of a neutral tracer. By analogy with the time of flight formulation, pressure fronts travel with a velocity given by $\nabla\tau\cdot\overrightarrow{\overrightarrow{\alpha}}$, rather than the gradient itself $\nabla\tau$. This is consistent with the result from method of characteristics. Thus, with the new representation of velocity, the equation describing pressure front trajectory $\psi$ should be written as

$$\frac{d\psi}{d\zeta}=\nabla\tau(x)\cdot\overrightarrow{\overrightarrow{\alpha}} \tag{A.5}$$

Another problem of previous method comes for the numerical scheme. To trace the trajectories in in Eq. (A.1), Kim (2009) used the Heun's method, known as the second-order Runge-Kutta method, to calculate the trajectories. This multi-step predictor-corrector method uses an estimated auxiliary value to improve the solution of the differential equation.

One major drawback of Heun's method is that the step size may need to be prohibitively small, especially when using the low-order method, so it may take enormous computation time. If step size is not small enough, it will cause the crossover issues between trajectories, which certainly violates the physics of these trajectories which follows the direction of diffusive time of flight gradient. Another major drawback of Heun's method is that the calculation of gradient $\nabla \tau$ simply uses the finite difference between $\tau$ values at neighboring cell and thus will not guarantee the flux continuity in the face and mass conservation within the cell. The error in the local gradient may result in large bias in trajectory direction. Since this error can accumulate along the trajectory, it is especially important to get correct gradient near the source.

To this end, we borrow the Pollock's linear velocity algorithm that has been widely used in tracing streamlines to analytically calculate pressure front trajectories. The major advantages of Pollock's solution are that: 1) the velocity model within each cell provides continuous flux between the cells, so it will generate physically correct trajectories; 2) sufficient degrees of freedom in the representation of velocity can be provided; 3) easy extension to corner point grid with cube Pollock's algorithm and isoparametric transformation.

In the cube Pollock approach for tracing streamline, the boundary conditions for the cell are very simple: flux is specified on each of the six faces and distributed uniformly across the faces. Similarly, for tracing pressure front trajectory, we prescribe the equivalent velocity on each face, as shown in Figure A.2. Replacing these quantity into

Pollock scheme will give the trajectory within the cell. By doing this, the trajectories are guaranteed to never cross.

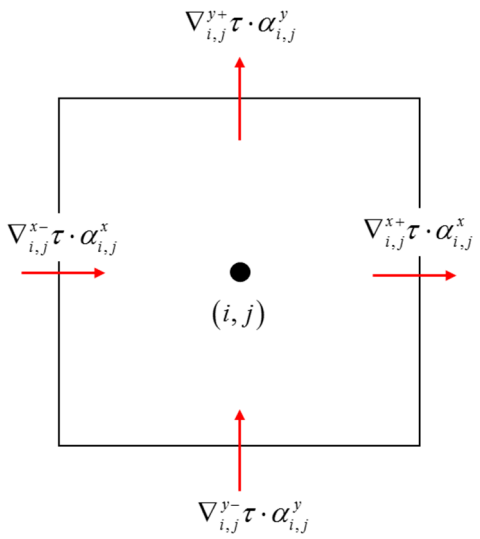


**Figure A.2 Pressure front tracing in the unit cell**

The next challenge is how to acquire these velocity at the cell face. A simple finite difference scheme used before would not maintain the velocity continuity. To enforce it, we need to first calculate the value at the 'phantom' node sitting at the cell interface. In Figure A.3, the 'phantom' node (hollow circle) used to force the velocity continuity condition in normal direction

$$\frac{\tau_{i-1/2,j} - \tau_{i-1,j}}{l_{I+}(i-1, j)} \cdot \alpha^{x}_{i-1,j} = \frac{\tau_{i,j} - \tau_{i-1/2,j}}{l_{I-}(i, j)} \cdot \alpha^{x}_{i,j} \qquad \text{(A.6)}$$

With the above equation, $\tau$ at the 'phantom' node and corresponding velocity can be calculated and substituted into Pollock's approach. Detailed description about Pollock's approach can be found in Datta-Gupta and King (2007).

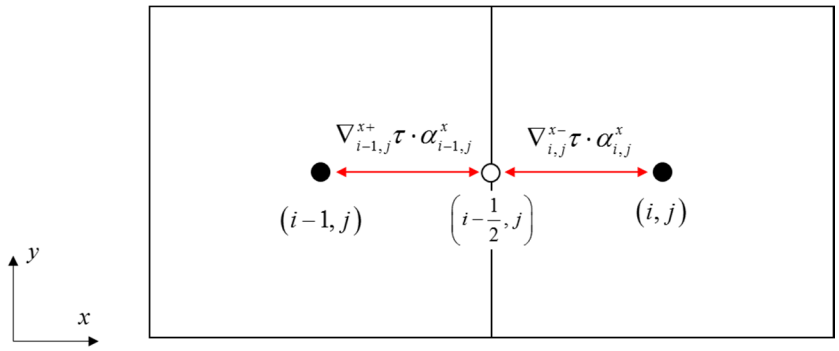


**Figure A.3 Numerical scheme used to maintain velocity continuity at the cell interface**

## A.3 Numerical Experiments

To validate the proposed method, we utilize an anisotropic field to compare the pressure front trajectories from both proposed and previous methods. Figure A.4 shows the comparison of pressure front trajectories by using different velocity representations in Eq. (A.1) and Eq. (A.5) in an homogeneous but anisotropic field where diffusivity coefficient ratio is $\alpha_x/\alpha_y=10$. The diffusive time of flight, i.e., underlying contour in Figure A.4, has elliptic shape with aspect ratio of $\sqrt{10}$. According to method of characteristics, since the field is isotropic, the characteristic line is thus expected to be straight lines radiating outward. It is clear in Figure A.4 (a) that by tracing Eq. (A.1), the trajectories are always orthogonal to diffusive time of flight contour but they fail to track the characteristic line which directly connects certain point with the source in

homogeneous case. Figure A.4 (b) shows the correction solution with straight lines in this homogeneous field.

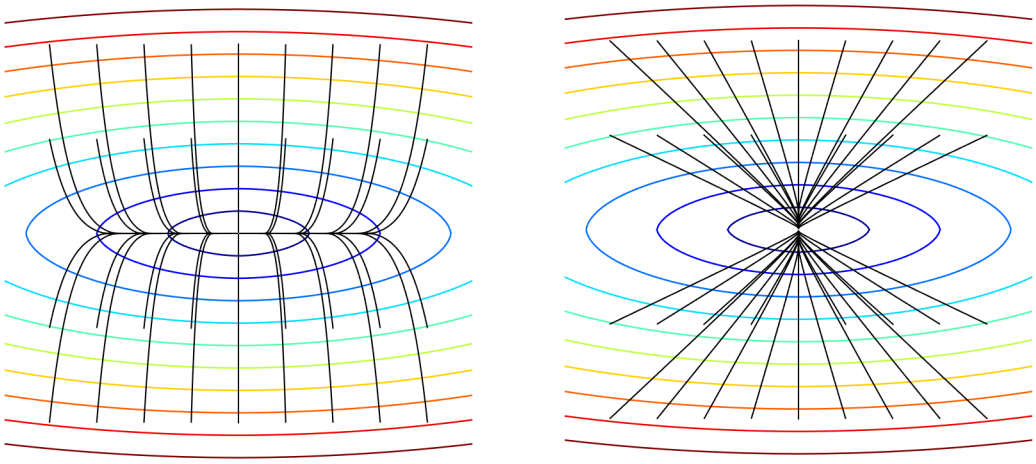

**(a)** **(b)**

**Figure A.4 Trajectories in an anisotropic field using (a) Eq. (A.1) (b) Eq. (A.5)**

To also demonstrate the advantages of proposed method in isotropic field, we test the two methods using a smoothly varying media with source sitting at the center of domain. Figure A.5 shows the comparison of trajectories from proposed method based on Pollock approach, compared with previous Heun's method. Relative large error near the well region could significantly deviate the trajectory. From the picture, we can see that the trajectories in proposed method are more distributed than that from Heun's method. The reason is that the proposed method results in a more accurate gradient transition near the well region.

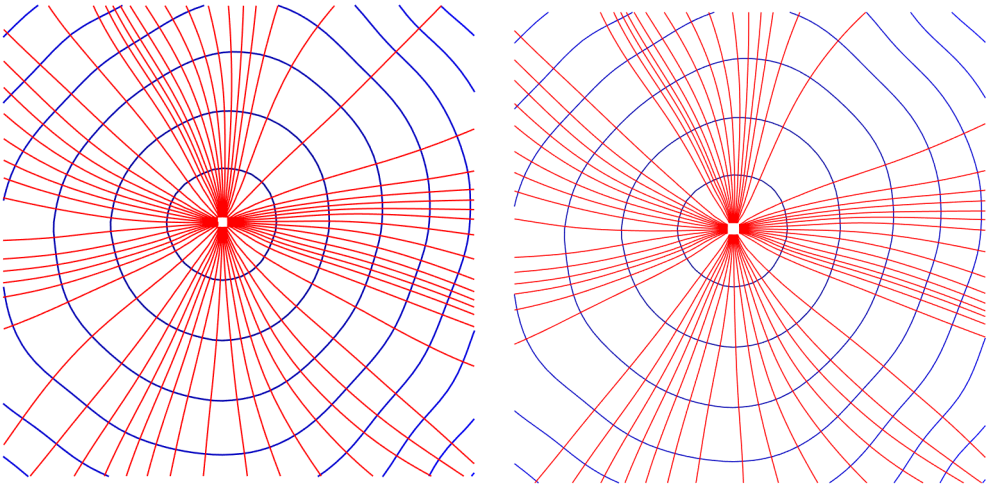

**(a)** **(b)**

**Figure A.5 Comparison of trajectories for source at the center by (a) Proposed method (b) Heun's method**

APPENDIX B

DISCRETIZATION SCHEMES OF FAST MARCHING METHOD

The various discretization schemes of fast marching method that have been used to solver the Eikonal equation will be systematically compared in this section. The solution accuracy from fast marching method, especially those near the source region, could significantly impact the subsequent pressure solution. Therefore, a robust and reliable scheme will be highly demanded in the real application of fast marching method in oil and gas industry. In this study, a 2D grid system will be used to demonstrate the accuracy and identify the best practice when using these schemes while extension to 3D is straightforward.

## B.1 Schemes of Fast Marching Method

### *B.1.1 Single-Stencil Scheme*

The Eikonal equation that governs the pressure front propagation in an isotropic medium is

$$\sqrt{\alpha}\left|\nabla \tau(\vec{x})\right| = 1 \tag{B.7}$$

a classical five-point (seven-point for 3D) single stencil scheme, local update of $\tau$ value in above equation can be written with the standard finite difference notation as (Sethian 1999)

$$\max\left(D_{ij}^{-x}\tau, -D_{ij}^{-x}\tau, 0\right)^2 + \max\left(D_{ij}^{-y}\tau, -D_{ij}^{-y}\tau, 0\right)^2 = \frac{1}{\alpha} \tag{B.8}$$

where $D_{ij}^{-x}$ and $D_{ij}^{+x}$ are the standard backward and forward finite difference operator that can be written as $D_{ij}^{-x}\tau = \left(\tau_{i-1,j} - \tau_{i,j}\right)/\Delta x$ and $D_{ij}^{+x}\tau = \left(\tau_{i+1,j} - \tau_{i,j}\right)/\Delta x$ for $\pm x$ directions. Similar equations hold for $\pm y$ directions. In Eq. (B.8), $\tau$ values at unknown points are regarded as infinity and the "*max*" function is used to guarantee the "upwind" criteria as the solution must satisfy the causality relationship. It leads to a quadratic equation and its minimum positive root gives us the value at center point (i, j). More specifically, $\tau$ values will be calculated from each of the four quadrants by ordinary finite difference formulation among which the minimum value is taken.

Zhang et al. (2013) further extend the discretization of Eq. (B.8) for more general corner point grid by performing the isoparametric mapping and combining properties from the two half cells to get an average speed between neighbor cells in each principal direction, in analogy to transmissibility calculations for solving flow equations. Figure B.1 shows an example of 2D isoparametric mapping and the lower left quarter for cell (i, j) in the 5-stencil scheme. The discretization of Eq. (B.8) can be written for this case as

$$\frac{\left(\tau_{i,j} - \tau_{i-1,j}\right)^2}{s_I^2} + \frac{\left(\tau_{i,j} - \tau_{i,j-1}\right)^2}{s_J^2} = 1 \tag{B.9}$$

where $s_I$ and $s_J$ are the averaged 'slowness" (inverse to pressure front propagation speed) in the reference grid

$$S_I = \frac{l_{I+}(i-1, j)}{\sqrt{\alpha_I(i-1, j)}} + \frac{l_{I-}(i, j)}{\sqrt{\alpha_I(i, j)}} \tag{B.10}$$

$$S_J = \frac{l_{J+}(i, j-1)}{\sqrt{\alpha_J(i, j-1)}} + \frac{l_{J-}(i, j)}{\sqrt{\alpha_J(i, j)}} \tag{B.11}$$

Here $\alpha_I$ and $\alpha_J$ are diffusivity in *I* and *J* directions respectively. $l_{I+}$, $l_{I-}$, $l_{J+}$ and $l_{J-}$ are distances from cell centers to face centers as illustrated in Figure B.1. The same local solution has to be performed for the same cell (i, j) based on the other three pairs of neighbors and then the smallest $\tau$ value obtained from these solutions should be used as the updated value for cell (i, j).

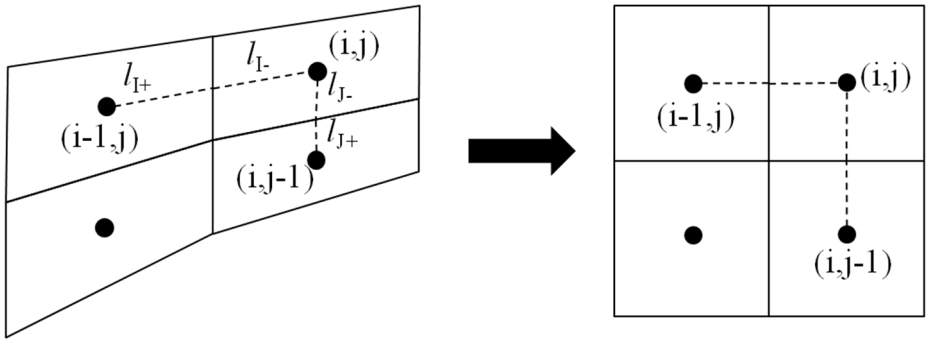


**Figure B.1 Isoparametric mapping and discretization for 2D example with corner point grid (from Zhang et al. (2013))**

### *B.1.2 Multi-Stencil Scheme*

These schemes based on classical single stencil generally ignore the information provided by diagonal points, they suffer from large numerical errors along diagonal directions. A lot of researchers have used diagonal nodes to enhance the accuracy of Eikonal solution. Generally, there are two approaches to use the diagonal information (Hassouna and Farag 2007). One is to use only one stencil that is centered and is always aligned with the natural

coordinate system. The coordinate system is then rotated to intersect the grid system at diagonal nodes. The second approach is to use several stencils that are centered but covering entire diagonal neighbor points, where the gradient is approximated using directional derivatives.

Following the second approach, Hassouna and Farag (2007) combine multiple stencils and directional derivatives within the FMM to improve the accuracy of solving the Eikonal equation on Cartesian domains. Figure B.2 shows the two stencils used for 2D Cartesian domain, where the nearest neighbor points are covered by left stencil and the diagonal points are covered by the right stencil. By doing this, we actually extend the scheme from five-stencil to nine-stencil in 2D.

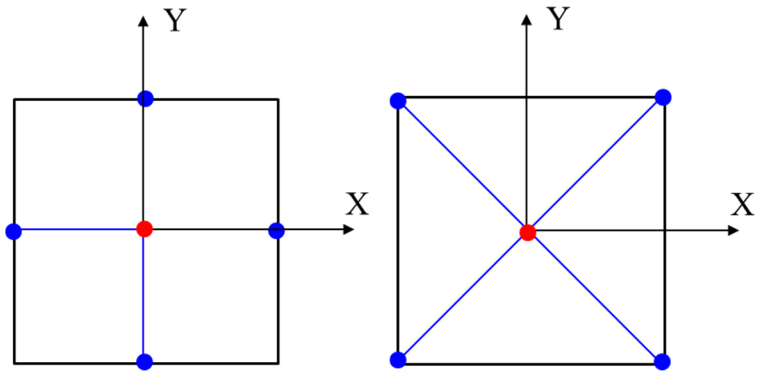


**Figure B.2 The two stencils used for 2D Cartesian domain**

### *B.1.3 Vertex-based Scheme*

In the single-pass algorithm, causality condition is required to ensure a good approximation of the characteristic direction and an accurate estimation of the value during the marching process. Zhang et al. (2013) demonstrate that the isotropic fast marching method will not produce acceptable results for general anisotropic cases. They

also demonstrate that for anisotropic permeability case, as long as the principal directions of the permeability are aligned with the cell edges, the causality condition will be satisfied. Figure B.3 illustrates the causality issues for isotropic and anisotropic cases for both good and bad scenarios. As we can see, in the corner point grid (right bottom picture), the major axis is always aligned with the cell edge, there is no causality issue.

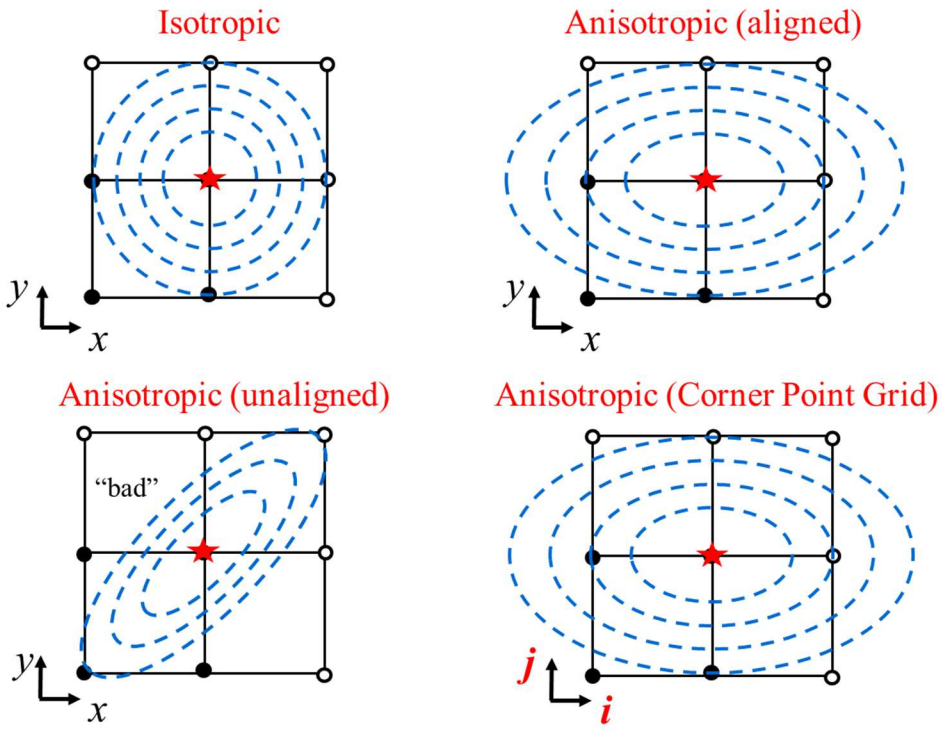


**Figure B.3 Illustration of the causality issues for isotropic and anisotropic cases**

However, for non-smoothly varying medium (locally high permeability contrast), causality condition may still be violated for both isotropic and anisotropic cases. The reason is that when we use cell center as solution node, the averaging of properties between two grid cells are required. This may lead to a local solution that is not the "minimum possible" travel time, violating causality condition. To avoid the causality

issue, a new scheme is proposed to use the cell vertices as the solution nodes instead of the cell centers (Zhang 2013). This vertex-based scheme includes two steps: a first global step where solutions are obtained at all vertices with the original center-based scheme and then a second local step where solutions at cell centers are locally solved within each cell using the value at the edge (or face in 3D) center interpolated from the vertices, which is illustrated in Figure B.4. By doing this, for a particular cell vertex, each local solution of the Eikonal equation is always inside a particular cell volume without property averaging. This guarantees "causality" because the nearest neighboring nodes always give the smallest travel time within that particular cell volume.

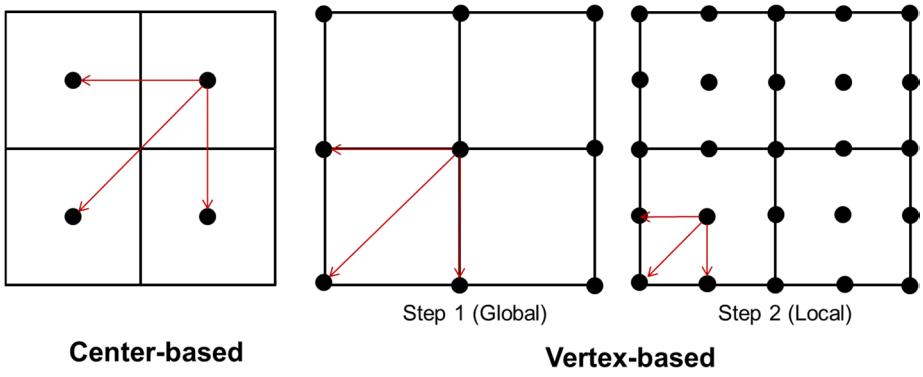


**Figure B.4 Comparison of center-based and vertex-based schemes**

Despite the advantage in dealing with causality issue, the vertex-based scheme may generate the path that is not the shortest from source point, especially in the near-source region. The reason is that vertex-based scheme utilizes the values of vertices to update the value at cell center. This can be illustrated in Figure B.5 where the vertex-based scheme chooses the path from source to vertices and then to the neighboring cell, resulting in a higher estimation. In contrast, the aforementioned center-center scheme avoids this issue

by directly calculating the center-to-center path. Therefore, an improved vertex-based scheme would be a mixed scheme by taking advantages of both vertex- and center-based schemes. That means, in the second step of vertex-based scheme, when we calculate the values at edge (or face in 3D) center, we need to pick the minimum from the values calculated from its vertices, as well as neighboring cell center.

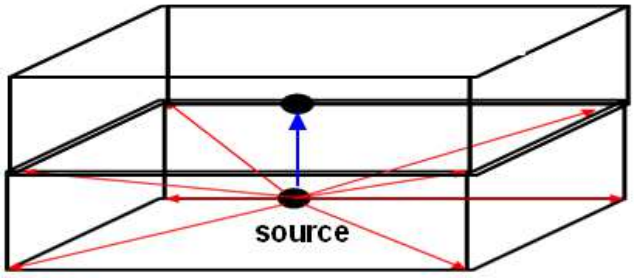


**Figure B.5 Comparison of vertex-based schemes near source term (red) with actual path (blue)**

### *B.1.4 Local Triangular Solver*

The above discretization schemes rely on the structured rectangular mesh. Extension of scheme to unstructured non-orthogonal grid system has been proposed by numerous researchers (Lelièvre et al. 2011; Qian et al. 2007; Sethian 1999). For unstructured grid, a local solver is generally required to solve the Eikonal equation on local triangle (2D) or tetrahedral (3D). Two distinct yet equivalent local solvers based on the Fermat's principle and Eulerian discretization are most widely used. Li and King (2016) demonstrated this triangular-based local solver that utilizes cell center, vertex and edge center by refining a 2D square gird system into triangles with both five-stencil and nine-stencil discretization. Compared with original fast marching method in Cartesian mesh, the accuracy will be

improved. The cost is additional degrees of freedom that have been introduced during refinement. For example, in nine-stencil discretization on 2D square grid, degree of freedom will increase to $(2n_x+1)\times(2n_y+1)$ on original $n_x \times n_y$ grid.

### B.2 Averaged Single-Stencil of Fast Marching Method

Realizing the drawback of classical single-stencil scheme where diagonal information is not utilized, we propose an averaged gradient scheme that takes diagonal node into account. To this end, we use averaged gradient in Eq. (B.8), as shown in Figure B.6

$$\left(\frac{\tau_{i,j}-\tau_{i-1,j}}{2s_I}+\frac{\tau_{i,j-1}-\tau_{i-1,j-1}}{2s_I'}\right)^2+\left(\frac{\tau_{i,j}-\tau_{i,j-1}}{2s_J}+\frac{\tau_{i-1,j}-\tau_{i-1,j-1}}{2s_J'}\right)^2=1 \tag{B.12}$$

where $s_I$, $s_I'$, $s_J$, $s_J'$ are the averaged 'slowness' in the reference grid as illustrated in Figure B.5 and $\beta$ is the aspect ratio

$$S_I=\frac{l_{I+}(i-1,j)}{\sqrt{\alpha_I(i-1,j)}}+\frac{l_{I-}(i,j)}{\sqrt{\alpha_I(i,j)}} \tag{B.13}$$

$$S_I'=\frac{l_{I+}(i-1,j-1)}{\sqrt{\alpha_I(i-1,j-1)}}+\frac{l_{I-}(i,j-1)}{\sqrt{\alpha_I(i,j-1)}} \tag{B.14}$$

$$S_J=\frac{l_{J+}(i,j-1)}{\sqrt{\alpha_J(i,j-1)}}+\frac{l_{J-}(i,j)}{\sqrt{\alpha_J(i,j)}} \tag{B.15}$$

$$S_J'=\frac{l_{J+}(i-1,j-1)}{\sqrt{\alpha_J(i-1,j-1)}}+\frac{l_{J-}(i-1,j)}{\sqrt{\alpha_J(i-1,j)}} \tag{B.16}$$

$$\beta = \frac{l_{I+}(i-1,j-1)+l_{I+}(i-1,j)+l_{I+}(i,j-1)+l_{I+}(i,j)}{l_{J+}(i-1,j-1)+l_{J+}(i-1,j)+l_{J+}(i,j-1)+l_{J+}(i,j)} \tag{B.17}$$

Unlike the multi-stencil and vertex-based schemes that double the amount of quadratic equations to be solved, one major advantage of this modification is that the diagonal information has been included without additional computational cost.

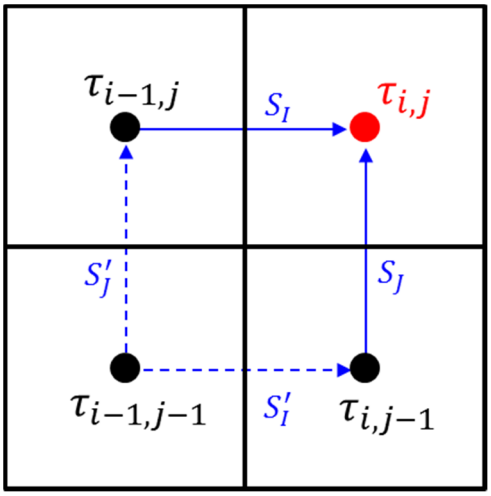


**Figure B.6 Illustration of averaged single-stencil scheme**

## B.3 Numerical Experiments

In order to study the accuracy and convergence of the proposed method, several numerical experiments have been conducted. We compare the accuracy of the proposed single-stencil FMM using averaged gradient (A-FMM) with original center-based single-stencil (S-FMM), multi-stencil (M-FMM), vertex-based (V-FMM) and triangular local (T-FMM) schemes.

Both homogeneous and heterogeneous will be used to compare the computed arrival time by each method. Analytical solution is available in homogeneous cases but

hard to find in heterogeneous cases, therefore we will study its convergence and use the refined model as our reference. To measure the error between the computed arrival time $\tau$ and the analytical (or reference) solution $\tau_\alpha$, the error function and $L_2$ norm are employed where *n* is the total number of grid cells

$$\varepsilon = \frac{\tau - \tau_a}{\tau_a} \tag{B.18}$$

$$L_2 = \sqrt{\sum_{i=1}^{n} |\tau - \tau_a|^2} \tag{B.19}$$

*Experiment 1: Homogeneous Isotropic Medium*

This experiment has a test grid of size 10 x 10, with $\Delta x = \Delta y = 1$. The speed function $\alpha$ is set to be a unit. The source point is set at the corner of the grid. Figure B.7 compares the error from above schemes and uses size of circle to indicate the magnitude of error, where cross 'x' represents the accurate solution. In all pictures, the greatest error appears in the lower left corner near the source, which corresponds to the wavefronts with the greatest curvature. This is reasonable since we assume planar wavefront in these schemes. Followings are the important observations from this comparison:

1. In of S-FMM, solutions along the two orthogonal directions are accurate but the errors increase rapidly in the region around 45 degree line.
2. M-FMM results in a smaller error than S-FMM, as well as exact solutions along the diagonal direction.
3. V-FMM results in a slightly larger error than S-FMM although it has the advantage of avoiding causality issues.
4. T-FMM uses local triangular solver and thus can get exact solution along its diagonal line. The overall error is much smaller than above local orthogonal solvers.
5. The proposed A-FMM results in the smallest error among all methods and also generates exact solution along diagonal line.

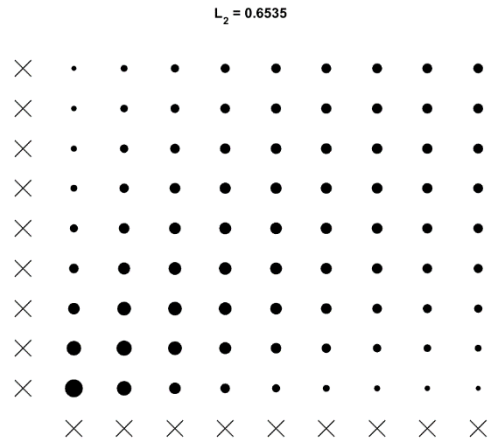


**(a) S-FMM**

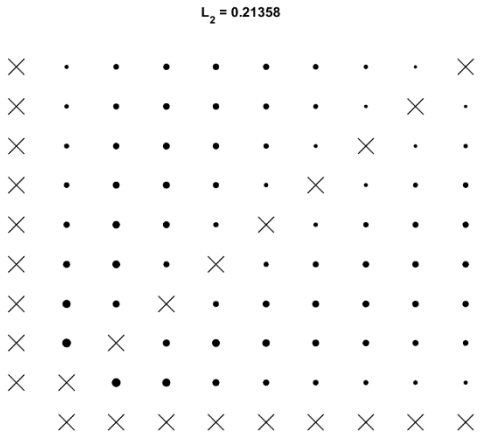


**(b) M-FMM**

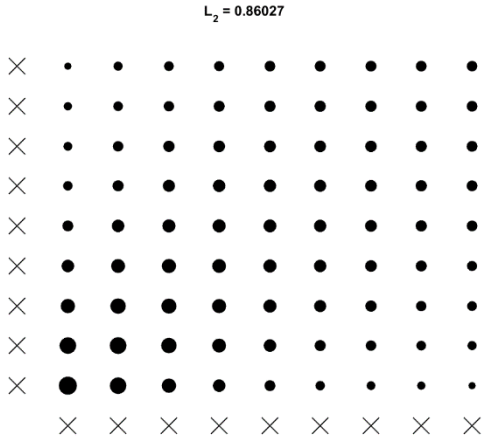


**(c) V-FMM**

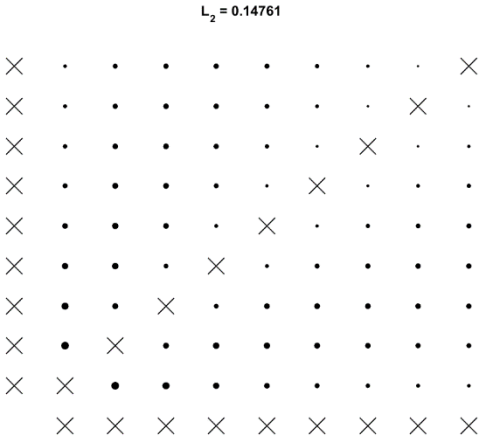


**(d) T-FMM**

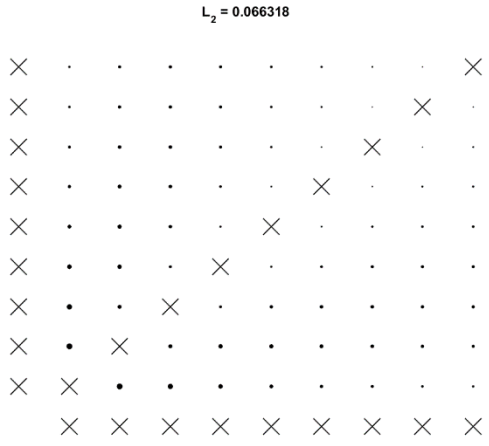


**(e) A-FMM**

**Figure B.7 Error comparison in homogeneous isotropic medium ('X' represents exact solution)**

*Experiment 2: Homogeneous Anisotropic Medium*

This experiment uses the same uniform test cell 10 x 10, but speed function is set to be anisotropic with $\sqrt{\alpha_x} = 5\sqrt{\alpha_y}$ . Figure B.8 compares the error from above schemes. The basic trend is similar to the isotropic medium but there are some different conclusions:

1. In the anisotropic case, the error is relatively larger along the large permeability direction which has smaller $\tau$ values (horizontal direction in the Figure B.8 for all schemes.
2. V-FMM results in a systematically larger error than cell center-based method.
3. T-FMM that uses local triangular still gives the exact solution along diagonal line and overall smaller error than above local orthogonal solvers.
4. The proposed A-FMM that uses the average of $\tau$ gradient no longer gives the exact solution along diagonal line, but still results in the smallest error among all methods.

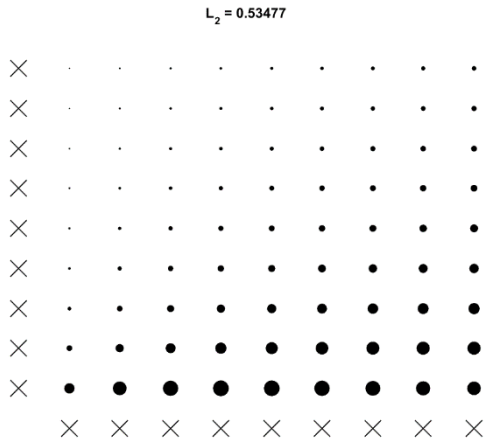


**(a) S-FMM**

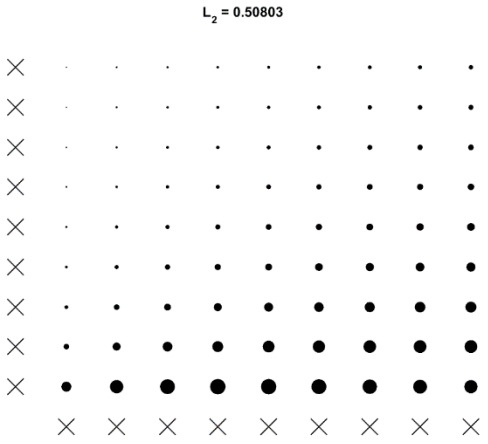


**(b) M-FMM**

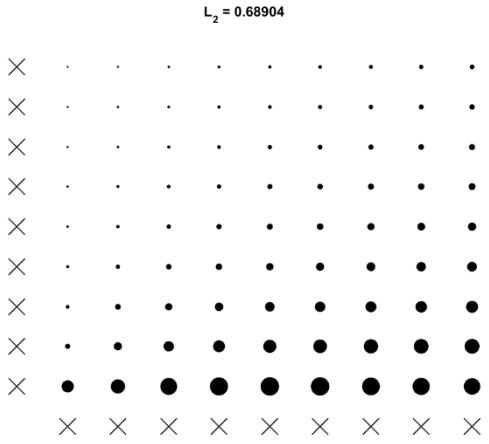


**(c) V-FMM**

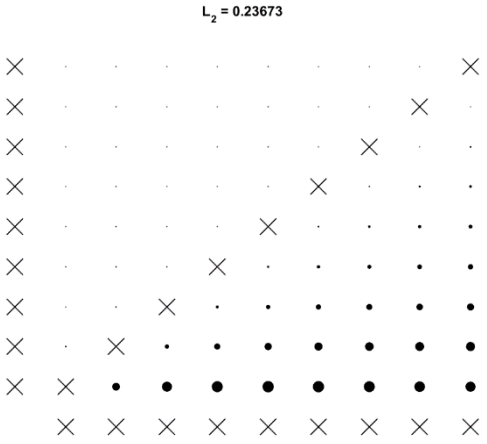


**(d) T-FMM**

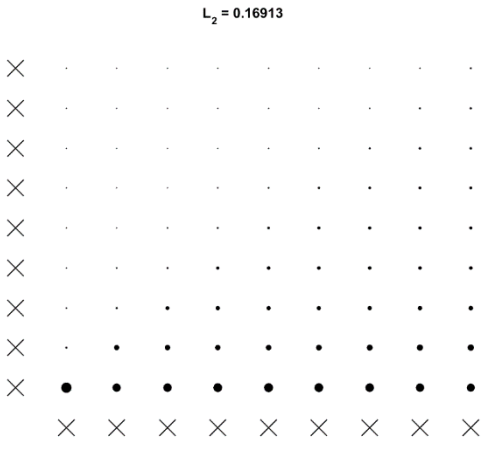


**(e) A-FMM**

**Figure B.8 comparison in homogeneous anisotropic medium (‘X’ represents exact solution)**

*Experiment 3: Slightly Heterogeneous Medium*

In the slightly heterogeneous medium shown in Figure B.9 (a), permeability varies smoothly and there is no high contrast of properties in neighboring cells. As a result, there is no potential causality issue. To demonstrate it, we use the method mentioned in Zhang (2013) to identify possible local violation of "causality issue" by doing local calculation for each grid block of a heterogeneous permeability field. Specifically, for each grid block, we calculate the travel time from the grid block to its four orthogonal and four diagonal neighbor grids. For each diagonal neighbor, we compare its travel time with that of the two adjacent immediate neighbors. If the diagonal neighbor's travel time is smaller than both of the immediate neighbors' travel time, we will increase the grid block's marking number by 1. If the diagonal neighbor's travel time is smaller than only one of the immediate neighbors' travel time, we will increase the grid block's marking number by 0.5. Therefore, the marking numbers for all the grid blocks will show which grid blocks may have potential causality issue. Figure B.9 (b) shows that no cell violates the causality condition in this slightly heterogeneous medium.

For the comparison study, since there is no analytical solution available for heterogeneous medium, we use the results of original single-stencil method on a very fine grid system as our reference. The convergence the convergence of original single-stencil method has been proved by many researchers (Hassouna and Farag 2007; Sethian 1996). A numerical method is said to be convergent if it approaches to the exact solution as the grid size goes to zero. Specifically, we refine the original grid from 10 x 10 to 270 x 270

and then exact the $\tau$ values at the same locations as our true solutions for comparison purpose.

Figure B.10 compares the error from above schemes. The major observations are:

1. M-FMM shows the notable advantage in the heterogeneous case, where the error is much smaller than S-FMM. This advantage is not obvious in homogeneous medium.
2. V-FMM still gives a slightly larger error than S-FMM because there is no causality issue in the smoothly heterogeneous medium.
3. T-FMM shows the substantial error reduction in heterogeneous medium compared with above methods at the expense of increased computational cost.
4. The proposed A-FMM gives the smallest error among all methods.

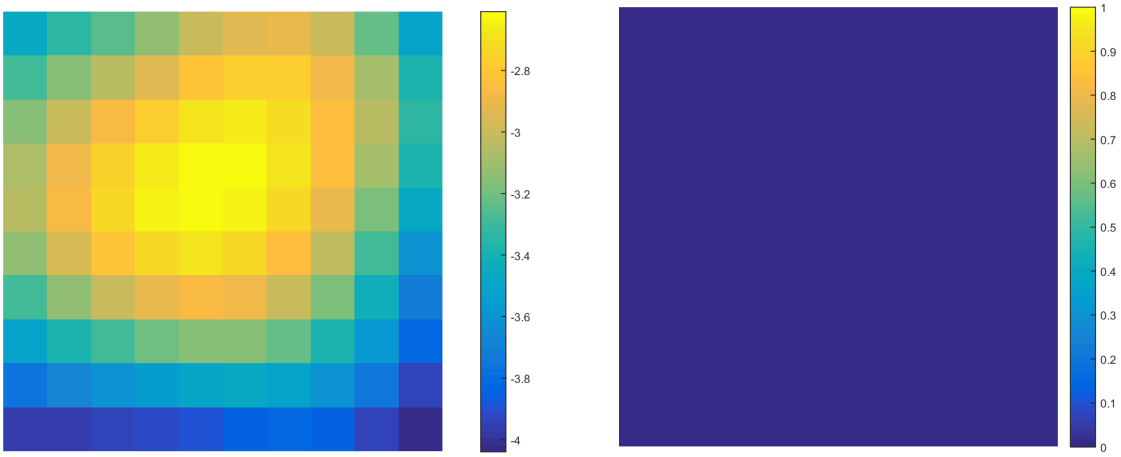


**Figure B.9 (a) Permeability field (10 x 10) and (b) Indicator of cells with causality issue for smoothly heterogeneous medium**

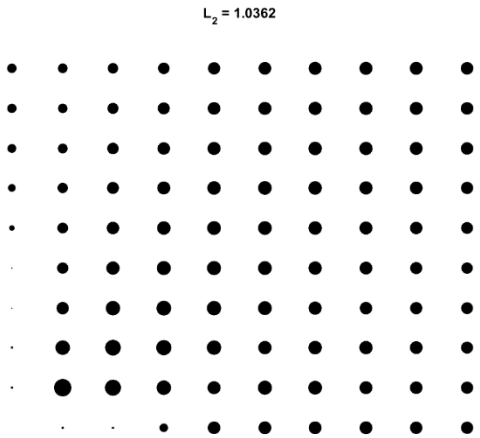


**(a) S-FMM**

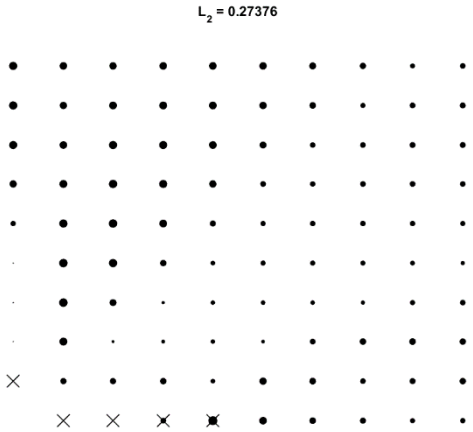


**(b) M-FMM**

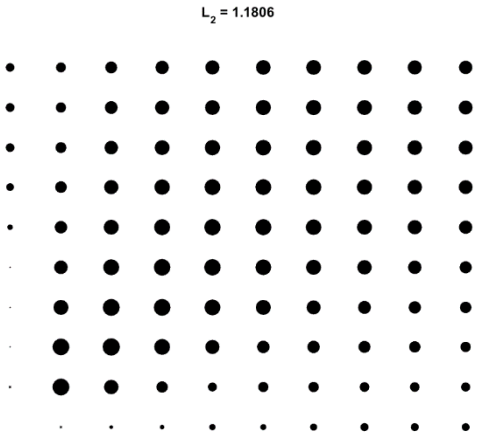


**(c) V-FMM**

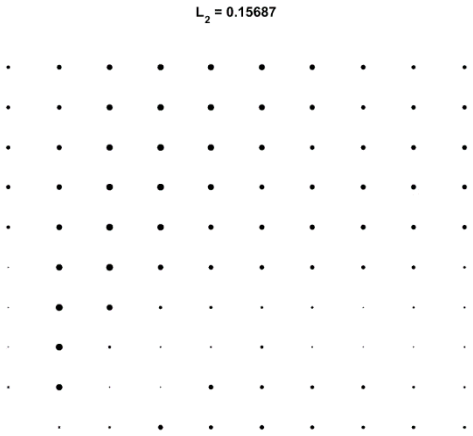


**(d) T-FMM**

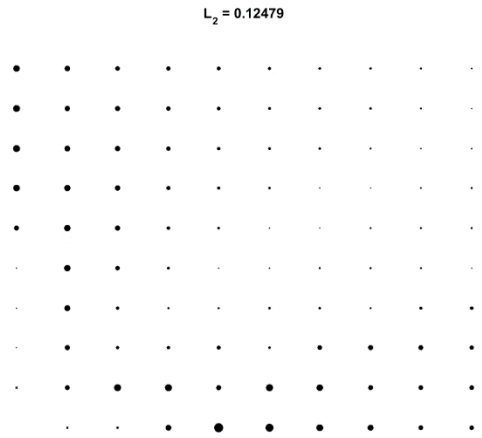


**(e) A-FMM**

**Figure B.10 comparison in smoothly heterogeneous medium**

*Experiment 4: Highly Heterogeneous Medium*

In the highly heterogeneous medium, permeability map displays a channelized pattern where permeability varies significantly and has strong local contrast at certain locations. Figure B.11 shows the permeability field and the indicator of cells with causality issue. In this case, most cell have potential causality issue. Again, we refine the initial grid from 10 x 10 to 270 x 270 and use the corresponding $\tau$ values as our true solutions for comparison purpose. Figure B.11 shows the error comparison and some new observations are summarized for the highly heterogeneous medium:

1. Traditional S-FMM has the worst performance since most cells may violate causality condition; similarly, M-FMM and proposed A-FMM are better than S-FMM but still give significant error.
2. In contrast, V-FMM and T-FMM show the best performance since these methods avoid the property average and thus have no causality issue.

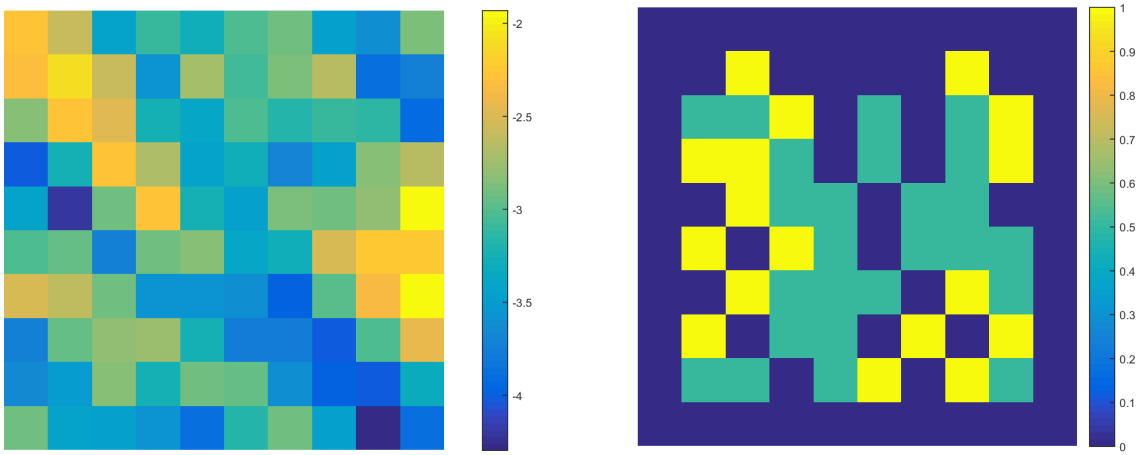


**Figure B.11 (a) Permeability field (10 x 10) and (b) Indicator of cells with causality issue for highly heterogeneous medium**

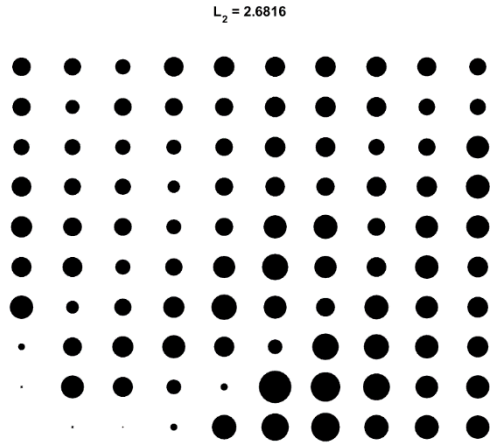


**(a) S-FMM**

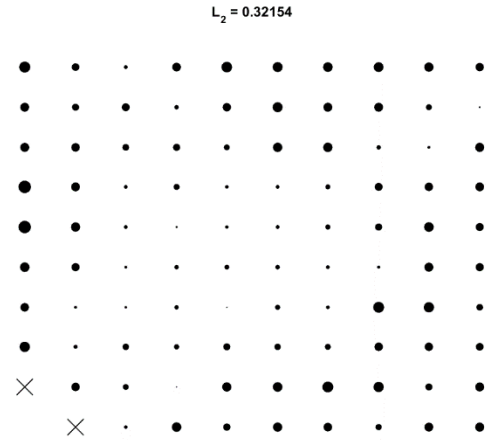


**(b) M-FMM**

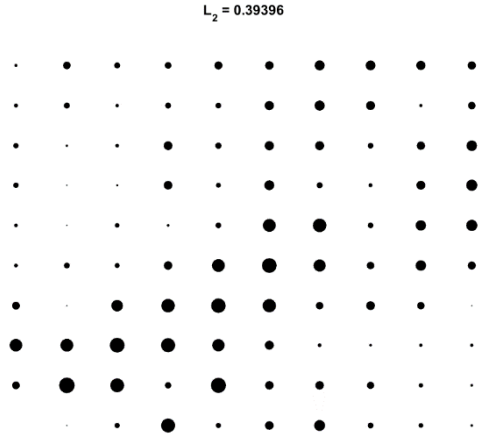


**(c) V-FMM**

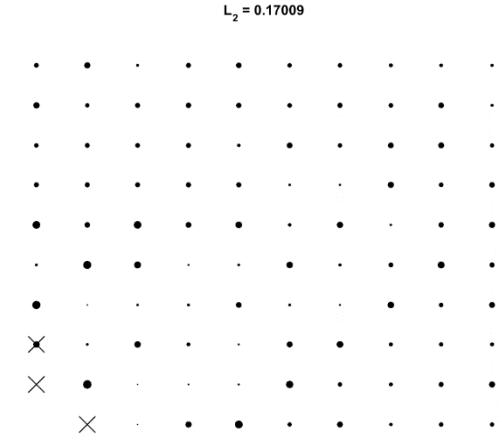


**(d) T-FMM**

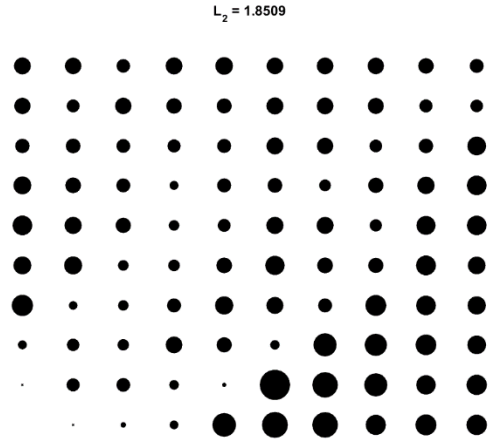


**(e) A-FMM**

**Figure B.12 comparison in highly heterogeneous medium**

## B.4 Summary

We propose an improved version of fast marching method (FMM) as a more accurate version of original FMM for solving Eikonal equation in Cartesian domain. We also compare a variety of existing fast marching algorithms used to solve the Eikonal equation. The accuracy of these methods has been demonstrated through comprehensive numerical experiments. The main findings are summarized as follows:

1. The proposed single-stencil FMM that uses averaged gradient (A-FMM) is always better than original center-based single-stencil FMM (S-FMM) in all cases. Therefore, the original FMM scheme is suggested to be replaced by the proposed method for any scenario.
2. In the cases without causality issue, the vertex-based scheme (V-FMM) cannot catch the shortest path and thus result in the largest error, whereas the proposed method has the top performance among these available schemes.
3. In the cases with potential causality issue, the vertex-based scheme (V-FMM) and triangular local solver (T-FMM) have best performance since they use the property averaging and thus avoid causality issue, at the expense of computational cost.